UNIVERSIDAD DE INVESTIGACION DE TECNOLOGIA EXPERIMENTAL YACHAY

Escuela de Ciencias Físicas y Nanotecnología

TÍTULO: Ab initio studies of magnetic and electronic properties of 2D $XGeTe_3$ alloys, where X=Cr, Mn, Fe.

Trabajo de integración curricular presentado como requisito para la obtención del título de Físico

Autor:

Morocho Luis

Tutor:

Ph.D - Pinto Henry

Cotutor:

Ph.D - Garay Tapia

Urcuquí, enero 2025

AUTORÍA

Yo, **Morocho Pogo Luis David**, con cédula de identidad 2100396262, declaro que las ideas, juicios, valoraciones, interpretaciones, consultas bibliográficas, definiciones y conceptualizaciones expuestas en el presente trabajo; así cómo, los procedimientos y herramientas utilizadas en la investigación, son de absoluta responsabilidad de el/la autora (a) del trabajo de integración curricular. Así mismo, me acojo a los reglamentos internos de la Universidad de Investigación de Tecnología Experimental Yachay.

Urcuquí, enero 2025.

Luis David Morocho Pogo
C.I: 2100396262

AUTORIZACIÓN DE PUBLICACIÓN

Yo, **Morocho Pogo Luis David**, con cédula de identidad 21003962626, cedo a la Universidad de Investigación de Tecnología Experimental Yachay, los derechos de publicación de la presente obra, sin que deba haber un reconocimiento económico por este concepto. Declaro además que el texto del presente trabajo de titulación no podrá ser cedido a ninguna empresa editorial para su publicación u otros fines, sin contar previamente con la autorización escrita de la Universidad.

Asimismo, autorizo a la Universidad que realice la digitalización y publicación de este trabajo de integración curricular en el repositorio virtual, de conformidad a lo dispuesto en el Art. 144 de la Ley Orgánica de Educación Superior

Urcuquí, enero 2025.

<div align="center">

_____

Luis David Morocho Pogo

C.I: 2100396262

</div>

Dedicatoria

Para mis padres:

Lorena y Luis

Y mis hermanos:

Xavier y Diego

Luis David Morocho Pogo

Agradecimiento

Luis David Morocho Pogo

´

Resumen

Este estudio presenta una investigación exhaustiva de las propiedades magnéticas y electrónicas de los monocapas XGeTe$_3$ (X = Cr, Mn, Fe) y sus aleaciones aleatorias, utilizando la teoría del funcional de la densidad (DFT) con los funcionales PBE y PBESol, complementados con correcciones de Hubbard U. CrGeTe$_3$ exhibe un robusto orden ferromagnético (FM) con una brecha de banda calculada que concuerda bien con los datos experimentales, destacando su potencial para aplicaciones prácticas. La monocapa MnGeTe$_3$ muestra un comportamiento de medio metal (HM), lo que lo hace particularmente prometedor para aplicaciones espintrónicas. En contraste, FeGeTe$_3$ revela un estado fundamental antiferromagnético (AFM) y posibles inestabilidades dinámicas, lo que requiere una mayor exploración para optimizar sus propiedades electrónicas.

En las aleaciones aleatorias, se observaron modificaciones significativas en los momentos magnéticos y las estructuras electrónicas. Específicamente, en Cr$_{1-x}$GeMn$_x$Te$_3$, el desorden en el momento magnético sugiere estados magnéticos fundamentales complejos, beneficiosos para la espintrónica. Mientras tanto, Cr$_{1-x}$GeFe$_x$Te$_3$ demuestra efectos de fuerte hibridación, indicando su idoneidad para sensores magnéticos y aplicaciones termoeléctricas. El sistema Fe$_{1-x}$GeMn$_x$Te$_3$ revela desafíos estructurales a mayores concentraciones de Mn, pero su estabilidad termodinámica respalda su potencial uso en uniones túnel magnéticas.

En general, esta investigación resalta las considerables perspectivas tecnológicas de los monocapas XGeTe$_3$ y sus aleaciones aleatorias, abogando por un control preciso de las propiedades magnéticas y electrónicas para avanzar en sus aplicaciones en espintrónica, memorias magnéticas y dispositivos termoeléctricos.

Palabras clave: Teoría del Funcional de la Densidad, monocapas, ferromagnetismo, antiferromagnetismo, semi-metal, aleaciones aleatorias.

Abstract

This study presents a thorough investigation of the magnetic and electronic properties of $XGeTe_3$ (X = Cr, Mn, Fe) monolayers and their random alloys, utilizing density functional theory (DFT) with PBE and PBESol functionals, supplemented by Hubbard U corrections. $CrGeTe_3$ exhibits robust ferromagnetic (FM) ordering with a calculated band gap that aligns well with experimental data, highlighting its potential for practical applications. The $MnGeTe_3$ monolayer shows half-metallic (HM) behavior, making it particularly promising for spintronic applications. In contrast, $FeGeTe_3$ reveals an antiferromagnetic (AFM) ground state and potential dynamical instabilities, necessitating further exploration to optimize its electronic properties.

For the random alloys, significant modifications in magnetic moments and electronic structures were noted. Specifically, in $Cr_{1-x}GeMn_xTe_3$, magnetic moment disorder suggests complex magnetic ground states beneficial for spintronics. Meanwhile, $Cr_{1-x}GeFe_xTe_3$ demonstrates strong hybridization effects, indicating its suitability for magnetic sensors and thermoelectric applications. The $Fe_{1-x}GeMn_xTe_3$ system reveals structural challenges at higher Mn concentrations, but its thermodynamic stability supports its potential use in magnetic tunneling junctions.

Overall, this research emphasizes the considerable technological prospects of $XGeTe_3$ monolayers and their random alloys, advocating for precise control over magnetic and electronic properties to advance their applications in spintronics, magnetic memory, and thermoelectric devices.

Keywords: Density Functional Theory, monolayers, ferromagnetism, anti-ferromagnetism, half-metal,random alloys.

Contents

List of Figures

List of Tables

Chapter 1

Introduction

Understanding how materials function at their fundamental levels is crucial for driving technological progress. Modelling and simulations, based on computational algorithms and supported by scientific theories[1,2], play a vital role in this process. They provide detailed insights into the behavior of materials at the atomic and molecular levels, enabling the design of new materials tailored to specific applications, such as storage devices[3], bio-materials, etc. This interdisciplinary field, commonly known as materials science, aims to accurately predict the properties of novel materials, ensuring alignment with experimental observations. The consistent validation of these predictions through experimentation, along with the pursuit of dependable and precise forecasts, is paramount for the success of this emerging discipline[4].

In this context, the exploration of two-dimensional (2D) materials, exemplified by the groundbreaking discovery of graphene in 2004[5], has drawn significant attention to this class of structures. These materials, characterized by a thickness of up to about a nanometer[6], present a unique spectrum of properties and diverse applications.

However, a significant challenge arises from the fact that many 2D materials are not thermodynamically stable and are expensive to synthesize due to the poor control of synthesized layers[7]. This challenge has prompted researchers to turn to theoretical simulations, using density functional theory (DFT), to guide the quest for new stable configurations. Examples like boron nitride[8] or transition metal dichalcogenides (TMDs)[9] highlight the rich possibilities inherent in 2D materials, ranging from tunable bandgaps[10] to intriguing electronic properties such as quantum confinement effects[11]. Another interesting class of materials that includes transition metal compounds are the transition-metal trichalcogenides (TMTCs) with the chemical formula ABX_3[12]. These materials display intriguing magnetic properties that can be utilized to understand the little-studied field of magnetism in 2D systems, which began with the experimental synthesis of magnetic $CrGeTe_3$[13] and CrI_3[14] monolayers in 2017. Furthermore, they offer insights into how magnetism can be

confined to only one plane and controlled by the thickness of the layers, owing to spin-orbit coupling or magneto-crystalline dipole-dipole interactions[15].

These intriguing phenomena, intimately linked to the behavior of d-spin electronic orbitals within transition metal atoms, can be addressed by GGA+U[16], a variant of the Generalized Gradient Approximation (GGA), in combination with the PBESol functional[17]. Such an approach, which has not been thoroughly studied for XGeTe3 monolayers can be allow the accurate description of on-site electron-electron interactions and provides improved predictions of structural and vibrational properties, respectively.

1.1 Problem Statement

We intend to utilize the approach described above to conduct ab initio simulations using density functional theory on TMTCs materials like XGeTe3 monolayers, where X represents a transition metal such as Cr (Chromium), Mn (Manganese), or Fe (Iron). This computational study aims to shed light on their potential applications and will be compared with theoretical and experimental studies on $MnGeTe_3$[18,19,20] 2D systems. Finally, magnetic alloys will be examined among these three monolayers.

1.2 General ans Specific Objectives

The primary objective of these computational studies is to employ advanced density functional theory methods for detailed investigations on monolayers of $XGeTe_3$, where X represents chromium (Cr), manganese (Mn), or iron (Fe). Thus, the following steps are undertaken:

- Explanation of the DFT basis and exchange-correlated functionals such as PBE, PBESol, and their enhancement with DFT+U formalism.

- Description of the formalism utilized to study $XGeTe_3$ monolayers, executed through calculations on the VASP package.

- Examination of the electronic, magnetic, and vibrational properties of $XGeTe_3$ monolayers using PBE and PBESol functionals.

- Performing Hubbard U corrections to accurately describe $XGeTe_3$ monolayers.

- Exploration of the formation of magnetic alloys by combining $XGeTe_3$ monolayers.

- Drawing conclusions to highlight key findings and implications.

Chapter 2

Theoretical Background

2.1 Many Body Schrödinger Equation

In the realm of materials science, exploring particle behavior within a system inevitably involves navigating the intricate principles of quantum mechanics. This journey commences with a comprehensive dissection of the energy components governing interactions among various particles, notably electrons and nuclei. At its core, quantum mechanics introduces the dual nature of particle-wave duality, with wavefunctions serving as the foundational framework.

As we delve deeper into the quantum landscape, one fundamental interaction shaping particle behavior is the Coulomb interaction. This interaction arises from the electrostatic forces between charged particles(electrons or nuclei), playing a pivotal role in determining the dynamics of electrons and nuclei within a material system[4,21].

The Coulomb interaction presents itself through three essential components: electron-electron, nucleus-nucleus, and electron-nuclei interactions. Mathematically, these interactions are expressed as follows:

- Electron-Electron interactions: between electron pairs

$$\hat{V}_{ee} = \frac{1}{2} \sum_{i \neq j}^{N} \frac{e^2}{4\pi\epsilon_0} \frac{1}{|\mathbf{r_i} - \mathbf{r_j}|} \tag{2.1}$$

- Nuclei-Nuclei interactions: between nuclei pairs

$$\hat{V}_{nn} = \frac{1}{2} \sum_{I \neq J}^{M} \frac{e^2}{4\pi\epsilon_0} \frac{Z_I Z_J}{|\mathbf{R_I} - \mathbf{R_J}|} \tag{2.2}$$

- Electron-Nuclei interaction:between electrons and nuclei

$$\hat{V}_{en} = -\sum_{i,I}^{N,M} \frac{e^2}{4\pi\epsilon_0} \frac{Z_I}{|\mathbf{r_i} - \mathbf{R_I}|} \tag{2.3}$$

Additionally, we need to consider the kinetic energy of both the N electrons and the M nuclei:

$$\hat{K} = -\sum_{i=1}^{N} \frac{\hbar^2}{2m_e} \nabla_i^2 - \sum_{I=1}^{M} \frac{\hbar^2}{2M_I} \nabla_I^2 \tag{2.4}$$

As we aim to explore the ground states of interacting electron and nuclei particles, we must consider the time-independent Schrödinger equation, defined simply as:

$$\hat{H}\psi(\mathbf{r}) = E\psi(\mathbf{r}) \tag{2.5}$$

Here $\hat{H}$ is the hamiltonian operator, which includes both kinetic and potential energies, and $\psi(\mathbf{r})$ is the wavefunction that describes the system's properties. For many-body systems, the wavefunction $\boldsymbol{\Psi}$ describes the positions of all electrons $(\mathbf{r_1}, \mathbf{r_2}, \mathbf{r_3}, ..., \mathbf{r_N})$ and nuclei $(\mathbf{R_1}, \mathbf{R_2}, \mathbf{R_3}, ..., \mathbf{R_M})$.

Expanding on equation 2.5, we get:

$$\left(\hat{K} + \hat{V}\right)\Psi = E_{tot}\Psi \tag{2.6}$$

Combining 2.1,2.2, 2.3, and 2.4, we can describe the many-body Schrödinger equation for N electrons and M nuclei as:

$$\left[-\sum_i \frac{\hbar^2}{2m_e}\nabla_i^2 - \sum_I \frac{\hbar^2}{M_I}\nabla_I^2 + \frac{1}{2}\sum_{i\neq j}\frac{e^2}{4\pi\epsilon_0}\frac{1}{|\mathbf{r_i} - \mathbf{r_j}|} + \right.$$
$$\left.\frac{1}{2}\sum_{I\neq J}\frac{e^2}{4\pi\epsilon_0}\frac{Z_I Z_J}{|\mathbf{R_I} - \mathbf{R_J}|} - \sum_{i,I}\frac{e^2}{4\pi\epsilon_0}\frac{Z_I}{|\mathbf{r_i} - \mathbf{R_I}|}\right]\Psi = E_{tot}\Psi \tag{2.7}$$

An issue related to equation 2.7 is its complexity in solving for many interacting particles. However, astonishing approximation methods have been studied over the last century, providing excellent accuracy to perform atomic simulations, which will be discussed in the next section.

2.2 Adiabatic Approximation

The 2.7 represents a first-principle approach to describing many-body interactions in quantum mechanics. In this framework, it's crucial to establish a consistent set of atomic units for

simplification and computational efficiency. Let's define some commonly used atomic units:

$$\hbar = 1.05457163 \times 10^{34} Js$$

$$m_e = 9.10938291 \times 10^{-31} kg$$

$$m_p = 1.67262164 \times 10^{-27} kg$$

$$e = 1.60217649 \times 10^{-19} C$$

$$\epsilon_0 = 8.85418782 \times 10^{-12} F/m$$

As we delve into the intricacies of kinetic energies within 2.7, the Hartree energy (E_H) emerges as a key player. Representing the total electrostatic interaction energy within a system of electrons and nuclei, excluding electron-electron interactions, the Hartree energy becomes particularly illuminating in the context of hydrogen atoms. In this scenario, characterized by a solitary electron and a single nucleus (proton), the Hartree energy aligns with the Coulomb energy of the electron-proton pair, and defined as

$$E_{Ha} = \frac{e^2}{4\pi\epsilon_0 a_0} \tag{2.8}$$

where $a_0 \simeq 0.529$ Å and based on its angular momentum:

$$m_e v a_0 = \hbar \tag{2.9}$$

Taking into account that inside the orbit of a hydrogen atom, the attraction of the electron to the nucleus is given by:

$$m_e \frac{e^2}{a_0} = \frac{e^2}{4\pi\epsilon_0 a_0^2} \tag{2.10}$$

We arrive at two important relations:

$$\frac{e^2}{4\pi\epsilon_0 a_0} = \frac{\hbar^2}{m_e a_0^2} \tag{2.11}$$

and

$$\frac{1}{2}m_e v^2 = \frac{1}{2}E_{Ha} \tag{2.12}$$

Then, by dividing each term of 2.7 by E_{Ha}, then we get:

$$\left[-\sum_i \frac{1}{2} a_0^2 \nabla_i^2 - \sum_I \frac{1}{2(M_I/m_e)} a_0^2 \nabla_I^2 + \frac{1}{2} \sum_{i \neq j} \frac{a_0}{|\mathbf{r_i} - \mathbf{r_j}|} \right.$$
$$\left. + \frac{1}{2} \sum_{I \neq J} Z_I Z_J \frac{a_0}{|\mathbf{R_I} - \mathbf{R_J}|} - \sum_{i,I} Z_I \frac{a_0}{|\mathbf{r_i} - \mathbf{R_I}|} \right] \Psi = \frac{E_{tot}}{E_{Ha}} \Psi \tag{2.13}$$

As we treat with Hartree atomic units, then the four constants that appear in 2.13 are set to 1. Thus,

$$\left[-\sum_i \frac{\nabla_i^2}{2} - \sum_I \frac{\nabla_I^2}{2M_I} - \sum_{i,I} \frac{Z_I}{|\mathbf{r_i} - \mathbf{R_I}|} + \frac{1}{2} \sum_{i \neq j} \frac{1}{|\mathbf{r_i} - \mathbf{r_j}|} + \right.$$
$$\left. \frac{1}{2} \sum_{I \neq J} \frac{Z_I Z_J}{|\mathbf{R_I} - \mathbf{R_J}|} \right] \Psi = E_{tot} \Psi \tag{2.14}$$

Now, based on the fact that the mass of nuclei is around 2000 times greater than the electron mass, implying that the kinetic energy of nuclei can be neglected; and also since the positions $\mathbf{R}$ are shifted by a constant amount, we have:

$$\sum_I \frac{\nabla_I^2}{2M_I} = 0 \quad \text{and} \quad E = E_{tot} - \frac{1}{2} \sum_{I \neq J} \frac{Z_I Z_J}{|\mathbf{R_I} - \mathbf{R_J}|} \tag{2.15}$$

And recognize that the term

$$V_n(\mathbf{r}) = -\sum_{i,I} \frac{Z_I}{|\mathbf{r_i} - \mathbf{R_I}|} \tag{2.16}$$

is accounting for the Coulomb potential of the nuclei experienced by the electrons. Then rewritten Eq. 2.14:

$$\left[-\sum_i \frac{\nabla_i^2}{2} + \sum_i V_n(\mathbf{r_i}) + \frac{1}{2} \sum_{i \neq j} \frac{1}{|\mathbf{r_i} - \mathbf{r_j}|} \right] \Psi = E \Psi \tag{2.17}$$

In order to know the equilibrium structure of a any system, we can treat the nuclei as fixed and thus we can approach the total wavefuction Ψ by separation of variables, splitting it into a wavefunction for electrons Ψ_R (that depends on the $\mathbf{R}$ nuclei positions) and the other one for nuclei(χ):

$$\Psi\left(r_1, ..., r_N, R_1, ..., R_M\right) = \Psi_R\left(r_1, ..., r_N\right)\chi\left(R_1, ..., R_M\right) \tag{2.18}$$

So, rewritten Eq. 2.17 in terms of **R** nuclei positions

$$\left[-\sum_i \frac{\nabla_i^2}{2} + \sum_i V_n(\mathbf{r}_i; \mathbf{R}) + \frac{1}{2}\sum_{i \neq j}\frac{1}{|\mathbf{r_i} - \mathbf{r_j}|}\right]\Psi_\mathbf{R} = E_\mathbf{R}\Psi_\mathbf{R} \tag{2.19}$$

Here $E_R = E\left(R_1, ..., R_M\right)$ represents the total electronic energy as a function of all nuclei positions, and V_n represents the Coulomb potential of the nuclei experienced by the electrons. It is also important to note that by using Eqs. 2.18 and 2.19 into equation 2.14, and then of applying normalization condition we obtain a equation describing solely the behavior of nuclei:

$$\left[-\sum_I \frac{\nabla_I^2}{2M_I} + \frac{1}{2}\sum_{I \neq J}\frac{Z_I Z_J}{|\mathbf{R}_I - \mathbf{R}_J|} + E\left(\mathbf{R}_1, ..., \mathbf{R}_M\right)\right]\chi = E_{tot}\chi \tag{2.20}$$

The separation of the total wavefunction into the components described by equations 2.19 and 2.20 is significant because it allows us to understand how the system behaves when there are changes in the positions of the nuclei. When the nuclei undergo small deviations from their initial positions to their final positions relative to the ground state, the electrons continue to occupy their lowest energy states. This phenomenon is known as adiabatic evolution, where the electron configuration adjusts smoothly to changes in the nuclear positions while staying in its ground state.

2.3 Hartree-Fock Theory

2.3.1 Pauli's exclusion principle

At the heart of the Hartree-Fock theory lies the Pauli exclusion principle, which states that no two fermions (particles with half-integer spin, such as electrons) can occupy the same quantum state simultaneously. This principle plays a crucial role in understanding the behavior of electrons in atoms and molecules, as it imposes constraints on the possible configurations of electron states.

To account for the Pauli exclusion principle, we introduce the concept of a Slater determinant. A Slater determinant is a determinant constructed from a set of orthonormal single-electron wavefunctions $\phi_i(\mathbf{r})$. For a system of N interacting electrons, the Slater determinant is constructed

as follows:

$$\Psi(\mathbf{r_1}, ..., \mathbf{r_N}) = \frac{1}{\sqrt{N!}} \begin{vmatrix} \phi_1(r_1) & \phi_1(r_2) & \cdots & \phi_1(r_N) \\ \vdots & \vdots & \ddots & \vdots \\ \phi_N(r_1) & \phi_N(r_2) & \cdots & \phi_N(r_N) \end{vmatrix} \tag{2.21}$$

2.3.2   Mean Field Approximation

Based on 2.18 we know that first two terms provide a way to account for the single-electron Hamiltonian, this is:

$$\hat{H}_0 = -\sum_i \frac{\nabla_i^2}{2} + \sum_i V_n(\mathbf{r_i}) \tag{2.22}$$

This Hamiltonian allows us to define Schrodinger equation based only of independent electrons:

$$\sum_i \hat{H}_0(\mathbf{r}_i)\Psi = E\Psi \tag{2.23}$$

where

$$\Psi(\mathbf{r}_1, \mathbf{r}_2, ..., \mathbf{r}_N) = \phi_1(\mathbf{r}_1)...\phi_N(\mathbf{r}_N) \tag{2.24}$$

Now in order to guarantee the Pauli's exclusion principle, i.e $\Psi(\mathbf{r}_2, \mathbf{r}_1) = -\Psi(\mathbf{r}_1, \mathbf{r}_2)$; we can use the definition of Slater determinant given by Eq. 2.21. Let's consider the case for $N = 2$ electrons:

$$\Psi(\mathbf{r}_1, \mathbf{r}_2) = \frac{1}{\sqrt{2}} [\phi_1(\mathbf{r}_1)\phi_2(\mathbf{r}_2) - [\phi_1(\mathbf{r}_2)\phi_2(\mathbf{r}_1)] \tag{2.25}$$

Then applying the normalization condition to that wavefunction, we arrive to the electron charge density $n(\mathbf{r})$:

$$n(\mathbf{r}) = |\phi_1(\mathbf{r})|^2 + |\phi_2(\mathbf{r})|^2 \tag{2.26}$$

And as we know from classical electrostatic (from Poisson's equation: $\nabla^2 V_H(\mathbf{r}) = -4\pi n(\mathbf{r})$) an electronic charge will generate a electrostatic potential as follows:

$$V_H(\mathbf{r}) = \int d\mathbf{r}' \frac{n(\mathbf{r}')}{|\mathbf{r} - \mathbf{r}'|} \tag{2.27}$$

This allows us to account for an extra term in the Schrodinger equation for each indepedent electron (within Eq. 2.23):

$$\left[-\frac{\nabla^2}{2} + V_n(\mathbf{r}) + V_H(\mathbf{r}) \right] \phi_i(\mathbf{r}) = \varepsilon_i \phi_i(\mathbf{r}) \tag{2.28}$$

These equations must be solved numerically and simultaneously among the Poisson's equation and the total electronic charge density $(n(\mathbf{r}) = \sum_i |\phi_i(\mathbf{r})|^2)$.

2.3.3 Hartree-Fock equations

As we see in the last subsection we can neglect the Coulomb repulsion of electrons. However that interaction as currently we know is not too strong and we can still search for the solution of single-particle wavefunctions, $\phi_i(\mathbf{r})$, in the form of a Slater determinant. Those solutions can be obtained using 'variational principle'.

First at all, lets consider the case for $N = 2$ electrons as it was described in the Eq. 2.25 and its lowest energy (in its Dirac notation):

$$E = \langle \Psi | \hat{H} | \Psi \rangle \tag{2.29}$$

Then, the Hamiltronian for this system can be expanded using Eq. 2.23:

$$\left[\hat{H}_0(\mathbf{r}_1) + \hat{H}_0(\mathbf{r}_2) + \frac{1}{|\mathbf{r}_1 - \mathbf{r}_2|} \right] \Psi = E\Psi \tag{2.30}$$

Then combining Eqs. 2.25, 2.29, and 2.30 and applying normalized and ortogonalized conditions $(\langle \psi_1 | \psi_1 \rangle = \langle \psi_2 | \psi_2 \rangle = 1$, and $\langle \psi_1 | \psi_2 \rangle = \langle \psi_2 | \psi_1 \rangle = 0$) after several algebraic manipulations:

$$E = \int d\mathbf{r} \psi_1^* \hat{H}_0(\mathbf{r})\psi_1(\mathbf{r}) + \int d\mathbf{r} \psi_2^*(\mathbf{r}) \hat{H}_0(\mathbf{r})\psi_2(\mathbf{r})$$
$$+ \int d\mathbf{r}_1 d\mathbf{r}_2 \frac{\psi_1^*(\mathbf{r}_1)\psi_2^*(\mathbf{r}_2)\psi_1(\mathbf{r}_1)\psi_2(\mathbf{r}_2)}{|\mathbf{r}_1 - \mathbf{r}_2|} - \int d\mathbf{r}_1 d\mathbf{r}_2 \frac{\psi_1^*(\mathbf{r}_1)\psi_2^*(\mathbf{r}_2)\psi_1(\mathbf{r}_2)\psi_2(\mathbf{r}_1)}{|\mathbf{r}_1 - \mathbf{r}_2|}$$

The last equations shows us the energy E is a functional of of ψ_1 and ψ_2. Then, we have to find those wavefunctions in order to minimize the functional. This is:

$$\frac{\delta E}{\delta \psi_1} = 0 \, , \frac{\delta E}{\delta \psi_2} = 0 \tag{2.31}$$

This minimization procedure would be treated better if we use Lagrange multipliers:

$$L\left[\psi_1, \psi_2, \lambda_{11}, ..., \lambda_{22} \right] = E[\psi_1, \psi_2] - \sum_{i,j} \lambda_{ij} \left[\langle \psi_i | \psi_j \rangle - \delta_{ij} \right] \tag{2.32}$$

Then, the minimization problem becomes:

$$\frac{\delta L}{\delta \psi_i} = 0 \; , i = 1, 2, \quad \frac{\delta L}{\delta \lambda_{ij}} = 0 \; , i, j = 1, 2 \tag{2.33}$$

After several algebraic manipulations and using the transformation:

$$\phi_i = \sum_j S_{ij} \psi_j \tag{2.34}$$

we get the so-called Hartree-Fock equations(generalized from the case $N = 2$ electrons):

$$\left[-\frac{\nabla^2}{2} + V_n(\mathbf{r}) + V_H(\mathbf{r}) \right] \phi_i(\mathbf{r}) + \int d\mathbf{r}' V_X(\mathbf{r}, \mathbf{r}') \phi_i(\mathbf{r}') = \varepsilon_i \phi_i(\mathbf{r}) \; , \tag{2.35}$$

$$n(\mathbf{r}) = \sum_i |\phi_i(\mathbf{r})|^2 \; , \tag{2.36}$$

$$\nabla^2 V_H(\mathbf{r}) = -4\pi n(\mathbf{r}) \; . \tag{2.37}$$

The importance of this equation lies in its ability to offer an accurate solution for the ground state based on a single-particle using the variational principle. As electrons inherently repel each other, the Hartree-Fock equations introduce an electron correlation, effectively minimizing the disparity between the calculated solution and the exact solution of the system.

2.4 Density Functional Theory

2.4.1 Hohenberg-Kohn Theorem

Based on 2.18 we can note that the left hand side represents the Hamiltonian of a many-electron system. This Hamiltonian encapsulates various energy contributions, such as kinetic energy, nuclear potential energy, and electron-electron repulsion. The Hohenberg-Kohn theorem plays a fundamental role in understanding the implications of this equation. To grasp its significance, let's start with the concept of the Hamiltonian's expectation value, denoted by E:

$$E = \langle \Psi | \hat{H} | \Psi \rangle = \int d\mathbf{r}_1 \cdots d\mathbf{r}_N \Psi^*(\mathbf{r}_1, \cdots \mathbf{r}_N) \hat{H} \Psi(\mathbf{r}_1, \cdots \mathbf{r}_N) \tag{2.38}$$

Now, here's where it gets interesting. The Hohenberg-Kohn theorem highlights a critical insight: If E represents the lowest energy state of the system, then E is uniquely determined by the electron density n:

$$E = F[n] \tag{2.39}$$

Why is this equation so powerful? Well, consider this: the wave function $\Psi(\mathbf{r}_1, \cdots \mathbf{r}_N)$ describes a system with N electrons, each moving in three-dimensional space. That's a whopping $3N$ unknowns to solve for! It's practically impossible to tackle directly. But the Hohenberg-Kohn theorem simplifies everything by asserting that the ground state energy depends solely on the electron density, which is a function of just three variables. This remarkable theorem is built upon three logical premises:

1. The electron density uniquely determines the external potential felt by the nuclei.

2. This external potential determines the wave function describing the behavior of the many-electron system.

3. Finally, the wave function uniquely determines the total energy of the system,meaning that the ground state is non-degenerate.

The amalgamation of these premises crystallizes into the central theorem, encapsulated in Equation 2.39. This succinctly encapsulates the profound implications of the Hohenberg-Kohn theorem[22], which can be distilled into two succinct theorems[23]:

Theorem 2.1. *When a system of N interacting electrons is subjected to an external potential V_{ext}, this potential is solely dependent of the electron density n of the ground state.*

Theorem 2.2. *Let $E[n]$ denote the functional representing the energy relative to the electronic density for a given V_{ext}. Then, this functional attains its global minimum corresponding to the ground state.*

Let's proceed to prove both theorems. As indicated by equation 2.18, the Hamiltonian for a many-electron system is defined as:

$$\hat{H} = -\sum_i \frac{\nabla_i^2}{2} + \sum_i V_n(\mathbf{r_i}) + \frac{1}{2} \sum_{i \neq j} \frac{1}{|\mathbf{r_i} - \mathbf{r_j}|} = \hat{T} + V_{ext} + \hat{W} \tag{2.40}$$

where $\hat{T}$ represents the kinetic energy, V_{ext} denotes the external potential, and $\hat{W}$ accounts for the Coulomb energy. The expectation value of that Hamiltonian gives us:

$$\begin{aligned}
E &= \langle\Psi|\hat{H}|\Psi\rangle = \langle\Psi|V_{ext}|\Psi\rangle + \langle\Psi|\hat{T} + \hat{W}|\Psi\rangle \\
E &= \langle\Psi|\sum_i V_n(\mathbf{r})|\Psi\rangle + \langle\Psi|\hat{T} + \hat{W}|\Psi\rangle \\
E &= \int V_n(\mathbf{r})n(\mathbf{r})d\mathbf{r} + \langle\Psi|\hat{T} + \hat{W}|\Psi\rangle
\end{aligned} \tag{2.41}$$

Now, let's make the assumption in line with 2.1, that there are two distinct ground states capable of yielding the same particle density.

$$E_0 = \langle \Psi_0 | \hat{H} | \Psi_0 \rangle < \left\langle \Psi'_0 \Big| \hat{H}' \Big| \Psi'_0 \right\rangle = \left\langle \Psi'_0 \Big| \hat{H}' - \sum_i V'_n(\mathbf{r}) + \sum_i V_n(\mathbf{r}) \Big| \Psi'_0 \right\rangle$$

$$E_0 < E'_0 + \left\langle \Psi'_0 \Big| \sum_i [V_n(\mathbf{r_i}) - V'_n(\mathbf{r_i})] \Big| \Psi'_0 \right\rangle \tag{2.42}$$

This results in:

$$E_0 < E'_0 + \int [V_n(\mathbf{r}) - V'_n(\mathbf{r})] n(\mathbf{r}) d\mathbf{r} \tag{2.43}$$

Using a similar procedure, we obtain the eigenvalue E'_0:

$$E_0 < E'_0 - \int [V_n(\mathbf{r}) - V'_n(\mathbf{r})] n(\mathbf{r}) d\mathbf{r} \tag{2.44}$$

Adding Equations 2.43 and 2.44, we arrive at:

$$E_0 + E'_0 < E_0 + E'_0 \tag{2.45}$$

This contradiction disproves our initial assumption. Thus, it is evident that the ground state is dependent on the electronic density.

2.4.2 Kohn-Sham Method

The HK theorem facilitates a reduction in the computational cost when dealing with a system comprising N interacting electrons compared to the Hartree Fock Theory. We acknowledge the existence of the functional $E = F[n]$, but without knowledge of its form. Consequently, Kohn and Sham proposed a procedure, supported by refs.[4,24,2].

This functional) is expressed as shown in equation 2.41:

$$F[n] = \int V_n(\mathbf{r}) n(\mathbf{r}) d\mathbf{r} + \langle \Psi[n] | \hat{T} + \hat{W} | \Psi[n] \rangle \tag{2.46}$$

The last two terms are the kinetic energy and the Coulomb repulsion of electrons and in comparison with the fist term their density dependence is not explicit. In this context, Kohn and Show[25] introduced an extra term $E_{xc}[n]$ to account for this discrepancy. Therefore rewritten 2.46:

$$E = \int V_n(\mathbf{r}) n(\mathbf{r}) d\mathbf{r} - \sum_i \int \phi_i^*(\mathbf{r}) \frac{\nabla^2}{2} \phi_i(\mathbf{r}) d\mathbf{r} + \frac{1}{2} \iint \frac{n(\mathbf{r}) n(\mathbf{r}')}{|\mathbf{r} - \mathbf{r}'|} d\mathbf{r} d\mathbf{r}' + E_{xc}[n] \tag{2.47}$$

Then, employing the variational principle of the Hohenberg-Kohn theory -orthonormal constraint- that is analogous to the method employed by the Hartree-Fock. So, we iteratively construct a set

of wave functions $\phi_i(\mathbf{r})$ through a self-consistent procedure, leading to the Kohn-Sham equations:

$$\left[-\frac{1}{2} + V_n(\mathbf{r}) + V_H(\mathbf{r}) + V_{xc}(\mathbf{r}) \right] \phi_i(\mathbf{r}) = \varepsilon_i \phi_i(\mathbf{r}) \tag{2.48}$$

Here $V_n(\mathbf{r})$ is the Hartree potential, $V_H(\mathbf{r})$ is the external potential, and $V_{xc}(\mathbf{r})$ is the exchange and correlation potential, defined as:

$$V_{xc} = \left. \frac{\delta E_{xc}[n]}{\delta n} \right|_{n(\mathbf{r})} \tag{2.49}$$

Our task now centers on crafting precise approximations for $E_{xc}[n]$.

2.4.3 Exchange-Correlation Functionals

2.4.3.1 Local Density Approximation

To accurately describe the electronic properties of a system, various methods have been developed to approximate the exchange-correlation functional described in Eq. (2.48). One of the simplest and most commonly used approximations is the Local Density Approximation[26,27](LDA). This method approximates the electron density of an inhomogeneous system by dividing it into several regions of volume $d\mathbf{r}$, treating each of these regions as a homogeneous electron gas (HEG) within a total volume V and taking into account the Coulomb repulsion between electrons[4].

$$E_{xc}^{LDA} = \int d\mathbf{r} n(\mathbf{r}) \epsilon_{xc}^{HEG} \left(n(\mathbf{r}) \right) \tag{2.50}$$

where ϵ_{xc}^{HEG} represents the exchange-correlation energy density.

To improve the description of the exchange-correlation energy functional, it is useful to separate the exchange part from the correlation part[28]:

$$E_{xc}^{LDA}[n] = E_x^{HEG}[n] + E_c^{HEG}[n] \tag{2.51}$$

The exchange energy density contribution is given by:

$$\epsilon_x^{HEG}(n) = -\frac{3}{4} \left(\frac{3}{\pi} n \right)^{1/3} \tag{2.52}$$

The correlation energy denisty was obtained using stochastic numerical methods and subsequently parametrized[26,27]. The correlation energy E_c is expressed as:

$$\epsilon_c^{HEG}(r_s(n)) = \begin{cases} A \ln r_s + B + C r_s \ln r_s + D r_s & \text{if } r_s < 1, \\ \frac{\gamma}{1 + \beta_1 \sqrt{r_s} + \beta_2 r_s} & \text{if } r_s \geq 1. \end{cases} \tag{2.53}$$

where $A = 0.0311, B = -0.048, C = 0.002, D = -0.0116, \gamma = -0.1423, \beta_1 = 1.0529, \beta_2 = 0.334$. Here, r_s the Wigner-Seitz radius, is a dimensionless parameter representing the average inter-electron distance; i.e :

$$r_s = \left(\frac{3}{4\pi n} \right)^{1/3} \tag{2.54}$$

By utilizing the LDA, researchers can make reasonable approximations for the exchange-correlation functional in systems where the electron density varies slowly. This method forms the foundation for more sophisticated approximations and has been instrumental in the advancement of density functional theory (DFT) calculations in material science and condensed matter physics.

2.4.3.2 Local Spin Density Approximation

To study magnetic systems, such as magnetic monolayers, it is crucial to account for spin polarization, as this is essential for capturing the system's magnetic properties. Unlike the LDA, which treats the electron density as spin-independent, many magnetic systems require a treatment that explicitly includes spin polarization. This involves considering separate spin-up ($n_\uparrow$) and spin-down ($n_\downarrow$) densities, which is essential for accurately describing the magnetic characteristics of the system.

In the Local Spin Density Approximation (LSDA), the exchange-correlation energy functional E_{xc}^{LSDA} is modified to account for spin polarization. It is given by:

$$E_{xc}^{LSDA}[n_\uparrow, n_\downarrow] = \int d\mathbf{r} n(\mathbf{r}) \, \epsilon_{xc}^{HEG}(n_\uparrow(\mathbf{r}), n_\downarrow(\mathbf{r})) \tag{2.55}$$

$$= \int d\mathbf{r} n(\mathbf{r}) \left[\epsilon_x^{HEG}(n_\uparrow(\mathbf{r}), n_\downarrow(\mathbf{r})) + \epsilon_c^{HEG}(n_\uparrow(\mathbf{r}), n_\downarrow(\mathbf{r})) \right]$$

Here, ϵ_{xc}^{HEG} represents the exchange-correlation energy per particle for a homogeneous electron gas, which depends on the spin-up and spin-down densities.

The exchange energy contribution E_x^{LSDA} is calculated using:

$$E_x^{LSDA}[n_\uparrow, n_\downarrow] = \frac{1}{2} \left[E_x^{LDA}[2n_\uparrow] + E_x^{LDA}[2n_\downarrow] \right] \tag{2.56}$$

The exchange energy per electron $\epsilon_x^{HEG}(n, \zeta)$ is then expressed as:

$$\epsilon_x^{HEG}(n, \zeta) = \epsilon_x^{HEG}(n, \zeta = 0) + \left[\epsilon_x^{HEG}(n, \zeta = 1) - \epsilon_x^{HEG}(n, \zeta = 0)\right] f(\zeta) \qquad (2.57)$$

where ζ is the spin polarization parameter, defined by:

$$\zeta = \frac{n_\uparrow - n_\downarrow}{n_\uparrow + n_\downarrow} \qquad (2.58)$$

and $f(\zeta)$ is a factor accounting for spin polarization:

$$f(\zeta) = \frac{(1 + \zeta)^{4/3} + (1 - \zeta)^{4/3} - 2}{2(2^{1/3} - 1)} \qquad (2.59)$$

The correlation energy can be computed numerically using the Random Phase Approximation (RPA) and then parametrized as described in the literature[29,30].

To assess the effectiveness of LSDA, it is helpful to define the exchange-correlation hole density as a function of electron distances, $\overline{n}_{xc}^{HEG}(n_\uparrow, n_\downarrow; u)$. The average hole density for LSDA is:

$$\langle \overline{n}_{xc}^{LSDA}(u) \rangle = \frac{1}{N} \int d\mathbf{r} \, n(\mathbf{r}) \, \overline{n}_{xc}^{HEG}\left(n_\uparrow(\mathbf{r}), n_\downarrow(\mathbf{r})\right) \qquad (2.60)$$

Evaluating this average density at the same point, $\langle \overline{n}_{xc}(u = 0) \rangle$, reveals why E_{xc}^{LSDA} performs well in a local regime, predicting suitable the total E_{xc}^{LSDA}. However, it also shows that the LSDA does not adequately capture the correlation hole $\overline{n}_c^{LSDA}(u)$. Implyieng an undertimation and overstimation of exchange and correlation energies, respectively.

2.4.3.3 Generalized Gradient Approximation

To address the limitations of the Local Spin Density Approximation (LSDA), the Generalized Gradient Approximation (GGA) represents a significant advancement in density functional theory (DFT). The GGA enhances the accuracy of DFT calculations by incorporating not only the electron density $n(\mathbf{r})$ but also its gradient $|\nabla n(\mathbf{r})|$ in the exchange-correlation energy functional. This approach allows GGA to better handle spin electron densities.

The exchange-correlation energy within the GGA framework is expressed as:

$$E_{xc}^{GGA} = \int d\mathbf{r} \, n(\mathbf{r}) \, \epsilon_{xc}^{HEG}(n(\mathbf{r})) \, F_{xc} \left[n_\uparrow(\mathbf{r}), n_\downarrow(\mathbf{r}), \nabla n_\uparrow(\mathbf{r}), \nabla n_\downarrow(\mathbf{r})\right] \qquad (2.61)$$

Here, F_{xc} represents an enhancement factor that depends on both the density and its gradient, providing a more accurate description of the exchange-correlation effects.

Among various GGA functionals, the Perdew-Burke-Ernzerhof (PBE) functional is one of the most prominent and widely utilized. The exchange energy within the PBE functional is given by:

$$E_x^{PBE} = \int d\mathbf{r}\, \epsilon_x^{HEG}(n) \left[1 + \kappa - \frac{\kappa}{1 + \beta\pi^2 s^2/3\kappa} \right] \tag{2.62}$$

where $s(\mathbf{r})$ is defined as:

$$s(\mathbf{r}) = \frac{|\nabla n(\mathbf{r})|}{2n(\mathbf{r})k_F(\mathbf{r})} \tag{2.63}$$

The correlation energy in the PBE functional is expressed as:

$$E_c^{PBE} = \int d\mathbf{r} \left[\epsilon_c^{HEG} + nc_0\phi^3 \ln\left\{ 1 + \frac{(1 + At^2)\beta t^2/c_0}{1 + At^2 + A^2t^4} \right\} \right] \tag{2.64}$$

where $t(\mathbf{r})$ is given by:

$$t(\mathbf{r}) = \frac{|\nabla n(\mathbf{r})|}{2n(\mathbf{r})k_s(\mathbf{r})} \quad \text{and} \quad k_s = \sqrt{\frac{4k_F}{\pi}} \tag{2.65}$$

In general, the PBE functional tends to overestimate equilibrium lattice constants by approximately 1%, which contrasts with the LDA's tendency to underestimate these values by a similar margin. This discrepancy is significant in ab initio calculations, as it affects various properties such as phonons, magnetic moments, and band gaps. Perdew has noted that GGA functionals, including PBE, face a trade-off: while they may improve the accuracy of total energy calculations, they can worsen bond lengths.

To address this issue, the PBEsol functional has been proposed. The PBEsol functional aims to reduce the dependence on gradient density to achieve more accurate lattice parameters compared to PBE. However, it is worth noting that using PBEsol can lead to less accurate total energy predictions. Thus, while GGA functionals represent a substantial improvement over LSDA, they come with their own set of trade-offs that need to be carefully considered depending on the specific requirements of the computational study.

2.4.3.4 Hybrid functionals

The limitations observed in PBE and PBEsol functionals lead to the exploration of hybrid functionals, which aim to combine the advantages of different approaches to enhance accuracy. Hybrid functionals incorporate a portion of exact exchange from Hartree-Fock theory and other part comes splitting exchange-correlation potential into its exchange and correlation parts.

$$\left(-\frac{1}{2}\nabla^2 + V_n + V_H[n](\mathbf{r}) + (1-\alpha)V_x[n](\mathbf{r}) + V_c[n](\mathbf{r})\right)\psi_i(\mathbf{r}) + \int \alpha V_x^{HF}(\mathbf{r},\mathbf{r}')\psi_i(\mathbf{r}')d\mathbf{r}' = \varepsilon_i\psi_i(\mathbf{r}) \tag{2.66}$$

where $0 < \alpha < 1$. There are some common recipes, such as 'PBE0',that accounts for a mixing of Hartree-Fock exact exchange and a contribution of PBE exchange-correlations parts.

$$E_{xc}^{PBE0} = \frac{1}{4}E_x^{HF} + \frac{3}{4}E_x^{PBE} + E_c^{PBE} \tag{2.67}$$

Another common recipe is the HSE06 (Heyd-Scuseria-Ernzerhof 2006) functional, which is expressed as:

$$E_{xc}^{HSE06} = \frac{1}{4}E_x^{HF,SR}(\omega) + \frac{3}{4}E_x^{PBE,SR}(\omega) + E_x^{PBE,LR} + E_c^{PBE} \tag{2.68}$$

where ω controls the short and long-range separation and depends on the decomposition of Coulomb kernel:

$$\frac{1}{r} = S_\omega(r) + L_\omega(r) = \frac{erfc(\omega r)}{r} + \frac{erf(\omega r)}{r} \tag{2.69}$$

this ω parameter is semiempirical. When with use HSE03 and HSE06 functionals we set ω to 0.3 and 0.2 respectively.

Hybrid functionals will give us the better approximation for energy functional in the the current computational studies, but their computational cost implemenation is high as we can see in Fig. 2.1.
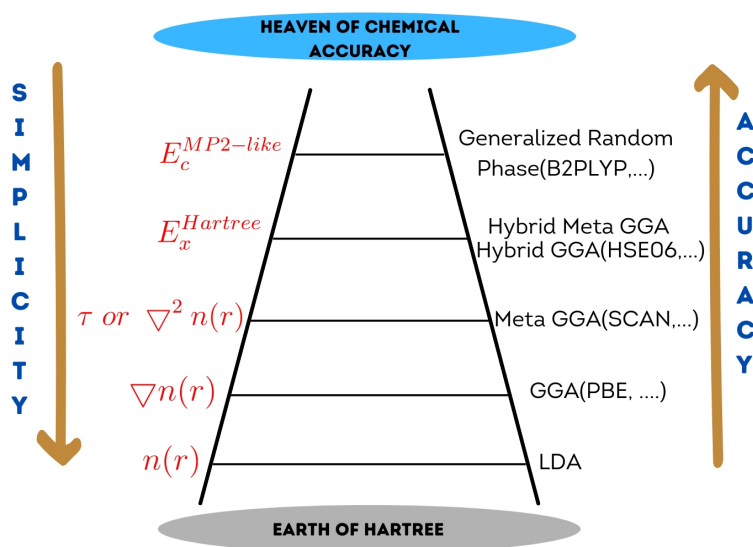
Figure 2.1: Jacob's Ladder of exchange-correlation functionals, as proposed by J.P. Perdew, illustrates the progression from the simplest approximations (Local Density Approximation, LDA) to more sophisticated and accurate functionals (Generalized Random Phase Approximations), ultimately reaching the "Heaven of Chemical Accuracy." The hierarchy is structured based on both the complexity of the functional and the accuracy of the results. Each rung represents an enhancement in accuracy by incorporating more detailed dependencies on the electron density $n(\mathbf{r})$ and its derivatives, such as the gradient $\nabla n(\mathbf{r})$, the Laplacian $\nabla^2 n(\mathbf{r})$, or the kinetic energy density τ. The GGA functionals, such as PBE and PBEsol, discussed earlier in this work, occupy the second rung, offering a balance between simplicity and accuracy. Hybrid GGAs (e.g., HSE06) and meta-GGAs (e.g., SCAN) ascend higher on the ladder, achieving greater chemical accuracy through the inclusion of additional terms.

2.5   DFT and Magnetism

In materials science, particularly when studying magnetic materials, Density Functional Theory (DFT) provides a powerful framework for understanding electronic structures. This is crucial for applications ranging from elucidating magnetism to designing high-energy-density permanent magnets and developing data storage technologies.

To explore the fundamental properties of electrons, we need to consider both electron density and spin density. Previously, we introduced electron density to identify an appropriate exchange-correlation functional. However, as Dirac proposed, an electron with velocity v and orbital angular momentum $\mathbf{L}$ generates and interacts with a magnetic field. This intrinsic property, known as 'spin,' must be explicitly addressed.

Thus, we expand our discussion to include spin density. This requires redefining the many-body wavefunction $\mathbf{\Psi}$ as a 4-spinor:

$$|\mathbf{\Psi}\rangle = \begin{pmatrix} |\psi_\uparrow\rangle \\ |\psi_\downarrow\rangle \end{pmatrix} \qquad (2.70)$$

Consequently, we can express the electronic and spin densities as 2-spinors, dependent on the position **r**:

$$n(\mathbf{r}) = \sum_i \mathbf{\Psi}_i^\dagger(\mathbf{r})\mathbf{\Psi}_i(\mathbf{r}) \tag{2.71}$$

$$\mathbf{s}(\mathbf{r}) = \sum_i \mathbf{\Psi}_i^\dagger(\mathbf{r})\mathbf{S}(\mathbf{r})\mathbf{\Psi}_i(\mathbf{r}) \tag{2.72}$$

where $\mathbf{S} = \frac{\hbar}{2}\sigma$ represents the spin operator, with σ denoting the Pauli matrices:

$$\sigma_x = \begin{pmatrix} 0 & 1 \\ 1 & 0 \end{pmatrix}, \quad \sigma_y = \begin{pmatrix} 0 & -i \\ i & 0 \end{pmatrix}, \quad \sigma_z = \begin{pmatrix} 1 & 0 \\ 0 & -1 \end{pmatrix} \tag{2.73}$$

Thus, electron and spin densities are defined as:

$$n(\mathbf{r}) = \sum_\alpha n_{\alpha\alpha'}(\mathbf{r}) \tag{2.74}$$

$$\mathbf{s}(\mathbf{r}) = \frac{\hbar}{2}\sum_{\alpha\beta} n_{\alpha\beta}(\mathbf{r})\sigma_{\alpha\beta} \tag{2.75}$$

We can then define a functional $G[n_{\alpha\beta}]$ that is minimized at the ground state density matrix $n_{\alpha\beta}^0(\mathbf{r})$:

$$\left.\frac{\delta G[n_{\alpha\beta}]}{\delta n_{\alpha\beta}}\right|_{n_{\alpha\beta}^0} = 0 \tag{2.76}$$

This leads to the Kohn-Sham equations for spin-DFT:

$$\left[-\frac{1}{2}\nabla^2 + V_n(\mathbf{r}) + V_H(\mathbf{r})\right]\psi_i(\mathbf{r};\alpha) + \sum_\beta v_{\alpha\beta}^{xc}(\mathbf{r})\psi_i(\mathbf{r};\beta) = \varepsilon_i\psi_i(\mathbf{r};\alpha) \tag{2.77}$$

where the exchange-correlation potential $v_{\alpha\beta}(\mathbf{r})$ is given by:

$$v_{\alpha\beta}(\mathbf{r}) = \left.\frac{\delta E_{xc}}{\delta n_{\alpha\beta}}\right|_{n_{\alpha\beta}(\mathbf{r})} \tag{2.78}$$

Rearranging terms, we define:

$$V_{xc} = \frac{v_{\uparrow\uparrow}^{xc} + v_{\downarrow\downarrow}^{xc}}{2}$$

$$B_x^{xc} = \frac{v_{\uparrow\downarrow}^{xc} + v_{\downarrow\uparrow}^{xc}}{2\mu_B}$$

$$B_y^{xc} = i\frac{v_{\uparrow\downarrow}^{xc} - v_{\downarrow\uparrow}^{xc}}{2\mu_B}$$

$$B_z^{xc} = \frac{v_{\uparrow\uparrow}^{xc} - v_{\downarrow\downarrow}^{xc}}{2\mu_B}$$

Thus, the exchange-correlation matrix is redefined as:

$$v_{\alpha\beta}(\mathbf{r}) = V_{xc}(\mathbf{r})\mathbf{1} + \mu_B\sigma \cdot \mathbf{B}_{xc}(\mathbf{r}) \tag{2.79}$$

Finally, the Schrödinger equation incorporating spin-DFT is:

$$\left[-\frac{1}{2}\nabla^2 + V_n(\mathbf{r}) + V_H(\mathbf{r}) + V_{xc}(\mathbf{r}) + \mu_B\sigma \cdot \mathbf{B}_{xc}(\mathbf{r})\right]\mathbf{\Psi}_i(\mathbf{r}) = \varepsilon_i\mathbf{\Psi}_i(\mathbf{r}) \tag{2.80}$$

It is important to consider the different magnetic configurations a system can exhibit. There are three possible configurations: ferromagnetism, antiferromagnetism, and paramagnetism. See Fig. 2.2.
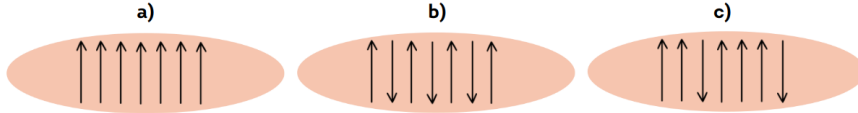
Figure 2.2: Types of magnetism. (**a**) shows a ferromagnetic configuration where all spins are aligned parallel. (**b**) shows an antiferromagnetic configuration where spins are aligned antiparallel in a magnetic order. (**c**) shows a paramagnetic configuration where the spins of electrons are randomly oriented without a preferred direction.

2.6 Computational implementation of DFT: the Vienna ab initio Simulation Package (VASP)

The present work is based on computational studies perfomed on VASP package. This package employs DFT methodology (it coudl be also perfomed calculations based on the GW method and dynamical electronic correlations) to perform ab initio calculations; widely used for a lot of currently research groups of a widely fields of investigations such as quantum theory of materials, solid state physics, materials sciences, etc.

VASP provides several fuunctionals , that are also bases on pseudopotentials to would be used based on system under investigation such as GGA, LDA, hybrids functionals, metaGGA functionals, etc.; in a way that we can replicate the electronic structure of a system under studied.

I would be explained some important aspects to consider within VASP framework .

2.6.1 Pseudopotentials

In exploring the wavefunctions that describe a range of atoms, we encounter a crucial question: how can we effectively manage the rapid oscillations of electron wavefunctions near the nucleus, which arise from the strong Coulomb potential?

To begin, we must consider the frozen-core approximation, which treats valence and core electrons separately. This approximation assumes that the nuclei remain immobile by effectively freezing the core electrons in their ground state, thus enabling us to focus on the valence electrons and significantly reduce computational costs. However, it is important to note that if core electrons are not treated appropriately, valence electrons may not be screened adequately. This screening effect is particularly critical in complex systems.

To mitigate these issues, Hamms Hemman introduced the concept of pseudopotentials in 1934[31]. This method replaces the oscillatory behavior of the Coulomb potential near the nucleus with a pseudopotential that accurately captures scattering effects within a specified energy range[32]. By effectively "freezing" the core region, this approach facilitates the study of low-energy states without the complications of strong core interactions.

Pseudopotentials effectively construct a repulsive potential that gives rise to pseudo-valence wavefunctions $|\tilde{\psi}_v\rangle$. These pseudo-valence wavefunctions are designed to reproduce the true valence wavefunctions $|\psi_v\rangle$, ensuring they remain orthogonal to the core wavefunctions $|\psi_c\rangle$:

$$|\tilde{\psi}_v\rangle = |\psi_v\rangle + \sum_c |\psi_c\rangle\langle\psi_c|\tilde{\psi}_v\rangle \tag{2.81}$$

Furthermore, these pseudo wavefunctions $|\tilde{\psi}_v\rangle$ must satisfy the effective single-particle Schrödinger equation:

$$H_{eff}|\psi_i\rangle = \varepsilon_i|\psi_i\rangle \quad \text{for } i = c, v. \tag{2.82}$$

This leads us to the equation:

$$H_{eff}|\tilde{\psi}_v\rangle = \varepsilon_v|\psi_v\rangle + \sum_c \varepsilon_c|\psi_c\rangle\langle\psi_c|\tilde{\psi}_v\rangle \tag{2.83}$$

$$= \varepsilon_v|\psi_v\rangle + \sum_c (\varepsilon_c - \varepsilon_v)|\psi_c\rangle\langle\psi_c|\tilde{\psi}_v\rangle. \tag{2.84}$$

Arranging this yields:

$$\left[H_{eff} + \sum_c (\varepsilon_c - \varepsilon_v)|\psi_c\rangle\langle\psi_c|\right]|\tilde{\psi}_v\rangle = \varepsilon_v|\tilde{\psi}_v\rangle. \tag{2.85}$$

As a result, we obtain the effective Hamiltonian of the pseudo-valence states given by:

$$H_{ps} = H_{eff} + \sum_c (\varepsilon_c - \varepsilon_v)|\psi_c\rangle\langle\psi_c|. \tag{2.86}$$

Thus, we can express the pseudopotential as:

$$v_{ps} = v_{eff} + \sum_c (\varepsilon_c - \varepsilon_v)|\psi_c\rangle\langle\psi_c|. \tag{2.87}$$

It is noteworthy that the pseudo-valence wavefunction, $|\psi_{ps}\rangle = |\tilde{\psi}_v\rangle$, associated with Eq. 2.85 has the same single-particle energy as the true valence wavefunction. However the pseudo wavefunction is not normalized in contrast to the normalized true wavefunction $|\psi_v\rangle$. This can be demonstrated by normalizing both sides of Eq. 2.81, revealing that the discrepancy in normalization is on the order of approximately 0.1[33]:

$$1 - \langle\psi_{ps}|\psi_{ps}\rangle = \sum_i |\langle\psi_c|\psi_{ps}\rangle|^2. \tag{2.88}$$

While this approach improves the representation of the nodal behavior of the valence wavefunction near the nucleus by employing a smoother wavefunction, it may also introduce certain inconveniences. To address these, several pseudopotentials have been developed to ensure correct behavior of the true valence wavefunction. According to Richard Martin[32], there are two key factors to consider when choosing a pseudopotential:

- On one hand, when the goal is to accurately replicate the true valence wavefunction ψ_c, a smaller cutoff radius r_c (defined as the distance beyond which the pseudopotential effectively vanishes) is preferred. This approach typically results in the use of hard pseudopotentials,

which provide a more precise description of the electron interaction in the vicinity of the nucleus. Hard pseudopotentials are particularly effective for capturing the strong interactions present in systems where the core states play a significant role.

- On the other hand, to optimize computational efficiency and reduce the complexity of calculations, a larger cutoff radius is often selected. This choice leads to the use of soft pseudopotentials, which allow for a smoother representation of the wavefunction and thereby simplify the mathematical treatment. Soft pseudopotentials can efficiently capture the essential physics of the system while requiring the use of fewer basis functions, significantly lowering the overall computational costs without sacrificing accuracy in many cases.

2.6.2 Projector Augmeted Wave method (PAW) in VASP

2.6.2.1 General Overview

The Projector Augmented Wave (PAW) method, implemented in the Vienna Ab initio Simulation Package (VASP), provides an accurate description of valence wave functions using a refined approach to pseudopotentials. PAW is based on the ultrasoft pseudopotential technique, which utilizes an auxiliary function surrounding each ionic core to enhance computational efficiency. Originally proposed by Blöchl, this method was subsequently generalized for magnetic systems in a collinear framework by Hobbs, Kress, and Hafner.

This section highlights the essential concepts of the PAW method.

2.6.2.2 Key Concepts

- **Brillouin Zone Integration**

    To describe a crystal system, it is essential to introduce the concept of the unit cell, which serves as the fundamental building block of the crystal lattice, characterized by a Bravais lattice—a periodic arrangement of lattice points. Each lattice point can be represented by lattice vectors $\mathbf{R}$:

$$\mathbf{R} = n_1\mathbf{a_1} + n_2\mathbf{a_2} + n_3\mathbf{a_3}, \tag{2.89}$$

    where n_1, n_2, n_3 are integers and $\mathbf{a_i}$ are the primitive vectors defining the lattice. Modeling a unit cell suffices to represent the entire crystal.

    To analyze electrons within the unit cell, we consider an electron subjected to a periodic potential $U(\mathbf{r})$ that satisfies the condition:

$$U(\mathbf{r} + \mathbf{R}) = U(\mathbf{r}), \tag{2.90}$$

where $\mathbf{R}$ is a lattice vector. This leads to Bloch's theorem, which states that the eigenstates ψ of the one-electron Hamiltonian $\hat{H} = -\nabla^2 + U(r)$ can be expressed as:

$$\psi_{n\mathbf{k}}(\mathbf{r}) = e^{i\mathbf{k}\cdot\mathbf{r}}u_{n\mathbf{k}}(\mathbf{r}), \tag{2.91}$$

where $\mathbf{k}$ is the wave vector defined in reciprocal space, and $u_{n\mathbf{k}}(\mathbf{r})$ is a periodic function of the Bravais lattice. It is crucial to account for the reciprocal lattice vector $\mathbf{G}$ to ensure that the wavevector $\mathbf{k}$ lies within the first Brillouin Zone (BZ), considering periodic boundary conditions:

$$\mathbf{k}' = \mathbf{k} + \mathbf{G} \quad \text{with} \quad \mathbf{G} = m_1\mathbf{b_1} + m_2\mathbf{b_2} + m_3\mathbf{b_3} \tag{2.92}$$

This formulation is essential for solving the Schrödinger equation and analyzing electron behavior in periodic potentials. By substituting the single-particle electronic wavefunction into the Kohn-Sham equations and normalizing, we obtain:

$$\int_{uc} |u_{n\mathbf{k}}(\mathbf{r})|^2 d\mathbf{r} = 1, \tag{2.93}$$

indicating that while the wavefunction $\psi_{n\mathbf{k}}$ is non-periodic, we must solve the Schrödinger equation for $u_{n\mathbf{k}}$ on a discrete grid in reciprocal space and apply appropriate boundary conditions to construct the electron density $n(\mathbf{r})$.

- **k-point sampling**

  From Eq. 2.93, we observe that the electronic density depends on the band index n and the $\mathbf{k}$-point in the reciprocal space within the Brillouin zone. Therefore, the relationoship between the eigenvalues and wavefunctions that arise from periodic boundary conditions relate to the $\mathbf{k}$-point as follows:

$$\epsilon_\lambda = \epsilon_{n\mathbf{k}} \quad \text{and} \quad \psi_\lambda = \psi_{n\mathbf{k}}. \tag{2.94}$$

An appropriate choice of $\mathbf{k}$-points is essential for accurately representing the electron density for occupied states $n\mathbf{k}$ as indicated in Eq. 2.93. For larger unit cells, fewer $\mathbf{k}$-points are necessary:

$$n(\mathbf{r}) = 2\sum_{n}^{\text{occ}} |\psi_{n\mathbf{k}}(\mathbf{r})|^2. \tag{2.95}$$

In the context of the Vienna Ab initio Simulation Package (VASP), two primary **k**-point sampling methods are employed: the Monkhorst-Pack scheme and Γ-centered meshes.

The Monkhorst-Pack scheme generates a uniform grid of **k**-points that are symmetrically distributed in the Brillouin zone. This method is advantageous for systems with high symmetry, as it allows for efficient integration over the Brillouin zone while ensuring that all relevant states are adequately sampled.

According to VASP documentation, the **k**-points that sample the Brillouin zone for the Monkhorst-Pack scheme are given by:

$$\mathbf{k} = \sum_{i=1}^{3} \frac{n_i + s_i + \frac{1-N_i}{2}}{N_i} \mathbf{b}_i \quad \forall n_i \in [0, N_i[\tag{2.96}$$

where

$$
\begin{aligned}
n_i &: \text{ indices representing the subdivisions along each direction,} \\
s_i &: \text{ optional shift in terms of subdivisions,} \\
N_i &: \text{ total number of subdivisions along each direction,} \\
\mathbf{b}_i &: \text{ reciprocal lattice vectors.}
\end{aligned}
\tag{2.97}
$$

On the other hand, Γ-centered meshes utilize Γ (the center of the Brillouin zone) as a reference point. This approach is often preferred for calculations involving metallic crystals, where the presence of electronic states near the Fermi level can substantially affect the results. The Γ-centered method helps capture these states more effectively, providing a denser sampling near the zone center.

According to the documentation, the **k**-points sample in the Brillouin zone are given by:

$$\mathbf{k} = \sum_{i=1}^{3} \frac{n_i + s_i}{N_i} \mathbf{b}_i \quad \forall n_i \in [0, N_i[\tag{2.98}$$

Both methods are crucial in achieving accurate electronic structure calculations and ensuring convergence in properties derived from these calculations, such as total energy, forces, and electron densities. Generally, the **k**-point mesh is given by a mesh in the form of:

$$N_x \times N_y \times N_z \tag{2.99}$$

Generally, such subdivisions are the same $N_x = N_y = N_z$. However, for monolayers $N_x = N_y, N_z = 1$.

It is important to mention that choosing the **k**-point scheme generally yields the same accuracy. However, it is advisable for a hexagonal crystalline lattice to choose a Γ-centered

scheme, as discussed by Chadi and Cohen [34], where an odd-grid is recommended due to space group symmetry considerations.

- **Plane Wave Expansion**

In the Projector-Augmented Wave (PAW) method, wavefunctions are described using plane waves due to their computational efficiency and completeness in representing periodic systems. From Bloch's theorem in Equation 2.91, we recognize that $u_{n\mathbf{k}}$ is periodic, and, following the analysis provided by Kantorovich[35], this periodic function can be expanded in direct space. Since $\psi_{n\mathbf{k}}$ is generally not periodic, we can expand it in reciprocal space using Fourier series, leading to the following expression:

$$\psi_{n\mathbf{k}}(\mathbf{r}) = e^{i\mathbf{k}\cdot\mathbf{r}} \frac{1}{\sqrt{\Omega}} \sum_{\mathbf{G}} e^{i\mathbf{G}\cdot\mathbf{r}} C_{n\mathbf{k}}(\mathbf{G}) \tag{2.100}$$

where $C_{n\mathbf{k}}(\mathbf{G})$ are the corresponding Fourier coefficients and

- **Cut-off energy**

Now that the basic concepts are introduced, let us delve deeper. As we remember from the pseudopotential section, the goal of the pseudo-valence wave function is to treat its nodal behavior. In this sense, plane waves with larger lattice vectors $\mathbf{G}$ are required to account for the aggressive valence wave functions near the core. Practically, this requires significant computational cost. To capture the main behavior of quantum states of the pseudo-valence wave function $\tilde{\psi}_v$ and avoid counting oscillations at short distances, it is advisable to define a cut-off radius that describes the G_{max} needed to accurately describe the valence spin-orbitals ψ_v.

$$|\mathbf{G}| \leq G_{max} \tag{2.101}$$

Using plane waves, we must follow the convergence criterion:

$$|\mathbf{G} + \mathbf{k}| < G_{max} \tag{2.102}$$

We aim to choose the associated cut-off energy adequately $E_{cut} = \frac{\hbar^2}{2m} G_{max}^2$.

In VASP, the cut-off energy is explicitly accounted for based on the atom and its orbital states. However, for systems with different atomic species, a convergence criterion given by the relationship between the cut-off energy and the total energy of a given system is needed:

$$\Delta E < 1\,\mathrm{meV/atom} \tag{2.103}$$

to obtain a good description of electronic properties.

- **Two-Dimensional Equation of State**

  In ab initio calculations, such as those performed using VASP, determining accurate lattice parameters is crucial. This determination provides a proper description of band gaps, magnetic moments, and is strongly correlated with phonon calculations. The Birch equation of state is commonly used for bulk systems; however, for computational studies of two-dimensional systems, a different equation of state is necessary to relate the system's area with its corresponding total energy. The equation derived from Andrew's paper[36] is employed for this purpose:

  $$E(A) = E_0 + 4A_0\gamma_0 \left\{ \frac{1}{2}\epsilon^2 + \frac{1}{6}(5 - \gamma_0')\epsilon^3 + \frac{1}{6}\left[(1 - \gamma_0')(8 - \gamma_0') + \gamma_0\gamma_0'' + 18\right]\epsilon^4 \right\} \quad (2.104)$$

  Here, A_0, γ_0, γ_0', and γ_0'' are the equilibrium values for the unit-cell area, layer modulus, the derivative of the force per unit length, and the second derivative of the layer modulus at $\mathcal{F} = 0$ (two-dimensional force per unit length), respectively. The strain ϵ is defined as the equibiaxial Eulerian strain:

  $$\epsilon = \frac{1}{2}\left[1 - \frac{A_0}{A}\right]. \quad (2.105)$$

2.6.2.3 Projector Augmented Wave (PAW) Method

With the foundational concepts introduced, we will now delve into the Projector Augmented Wave (PAW) method, which is extensively utilized in VASP for its ability to reduce computational costs while ensuring a numerical treatment compatible with pseudopotentials.

The primary objective of the PAW method is to accurately describe the true all-electron (AE) wavefunction from the pseudo wavefunction. A generalized form of this relationship can be expressed as follows:

$$\Psi = T\tilde{\Psi} \quad (2.106)$$

Here, T is defined as a transformation operator representing the connection between the true and pseudo wavefunctions. The significance of the PAW method is underscored in the following aspects:

- It facilitates a detailed description of the nodal structure of the pseudo valence wavefunction within each atomic region.

- It introduces the concept of the "Augmentation Sphere," which connects the pseudo wavefunction inside the augmentation region to that outside, delimited by the cutoff radius r_c. Within this sphere, the pseudo wavefunction adheres to Equation 2.106, while outside, we utilize $\Psi = \tilde{\Psi}$.

Given that T exhibits distinct behaviors inside and outside the augmentation sphere, it is beneficial to define it as:

$$T = \mathbb{1} + \sum_R T_R \tag{2.107}$$

In this expression, $\mathbb{1}$ denotes the identity operator, while T_R represents orbital-based modifications.

To elucidate these orbital-based modifications, we identify three critical components:

- All-electron partial waves $|\phi_i\rangle$

- Pseudo partial waves $|\tilde{\phi}_i\rangle$

- Projector functions $|\tilde{p}_i\rangle$, which facilitate the treatment of localized atomic orbitals within the augmentation sphere. The orthonormality condition $\langle \tilde{p}_i|\tilde{\phi}_j\rangle = \delta_{ij}$ holds for states within this region, leading to the completeness relation $\sum_i |\tilde{\phi}_i\rangle\langle\tilde{p}_i| = \mathbb{1}$.

In conformity with Bloch's theorem, we can express the pseudo valence wavefunction in terms of plane waves. To incorporate atomic orbital modifications appropriately, we represent a plane wave as a sum of spherical waves:

$$e^{i\mathbf{k}\cdot\mathbf{r}} = 4\pi \sum_{l=0}^{\infty} \sum_{m=-l}^{l} i^l j_l(kr) Y_l^m(\hat{k}) Y_l^{m*}(\hat{r}). \tag{2.108}$$

This expression enables us to describe the electronic wavefunction states indexed by $i = (R, l, m, n)$. Consequently, the all-electron wavefunction, derived from Equation 2.107, can be written as:

$$\Psi = \tilde{\Psi} + \sum_i \left(|\phi_i\rangle\langle\tilde{p}_i|\tilde{\Psi}\rangle - |\tilde{\phi}_i\rangle\langle\tilde{p}_i|\tilde{\Psi}\rangle \right) \tag{2.109}$$

This formulation reveals essential features of the all-electron wavefunction, which consists of three components: the first represents the pseudized version of the wavefunction, facilitating computational efficiency; the second incorporates the all-electron contributions within the augmentation

region; and the third addresses the contributions of the pseudized wavefunctions within the overall wavefunction.

Further mathematical details are outside the scope of this discussion, as they are not the primary focus of this thesis. However, it is pivotal to note that the true all-electron density can be computed based on the contributions expressed as:

$$n(\mathbf{r}) = \tilde{n}(\mathbf{r}) + n^1(\mathbf{r}) - \tilde{n}^1(\mathbf{r}) \tag{2.110}$$

In this equation, $n^1(\mathbf{r})$ is referred to as the "one-center" electronic density, accounting for the total contributions from all valence atomic states within the augmentation region.

Thus, we establish a clear advancement over conventional pseudopotentials by incorporating a dependency on three distinct constituents of the electronic density. As previously discussed, we can evaluate the exchange-correlation energy based on this electronic density framework.

Substantial contributions from Kresse and Joubert have further enhanced the PAW method by integrating it with well-established plane wave implementations[37], shifting the focus away from purely partial wave treatments. They reformulated the pseudo exchange-correlation treatment into a plane wave context by considering the vital contributions encapsulated in Equation 2.109. Additionally, they introduced a valence compensation charge density $\hat{n}$ to correct the charge pseudodensity in exchange-correlation energy calculations:

VASP offers functionality to construct pseudopotentials utilizing the PAW method; however, availability of the pseudopotential generator package may vary.

$$E_{K\,xc} = E_{xc}[\tilde{n} + \tilde{n}_c + \hat{n}] + \sum_a \left(E_{xc}^a[\tilde{n}^a + \hat{n}_c^a] - E_{xc}^a[\tilde{n}^a + \tilde{n}_c^a + \hat{n}^a] \right). \tag{2.111}$$

2.6.2.4   PAW and LDA+U

In this section, we discuss the implementation of the Projector Augmented Wave (PAW) method within the LDA+U framework. It is important to note that the electronic density defined in the PAW formalism does not account for spin-charge density. To address this limitation, Bengone et al.[38] redefined the electron charge density to incorporate spin effects, leading to the following formulation:

$$n_{m,m'}^{\tau,\sigma} = \sum_{n,\mathbf{k}} f_{n,\mathbf{k}}^\sigma \langle \tilde{\Psi}_n^{\mathbf{k},\sigma} | \tilde{P}_{m,m'}^\tau | \tilde{\Psi}_n^{\mathbf{k},\sigma} \rangle \tag{2.112}$$

where the variables are defined as follows:

$$\tau \equiv \text{atomic site,}$$

$$\sigma \equiv \text{spin,}$$

$$m, m' \equiv \text{magnetic quantum numbers for an } \ell \text{ (defining the matrix),}$$

$$n \equiv \text{band index,}$$

$$\mathbf{k} \equiv \text{given k-point,}$$

$$f \equiv \text{Fermi distribution,}$$

$$\Psi \equiv \text{All-Electron (AE) wavefunction,}$$

$$P \equiv \text{projection operator.}$$

This formulation focuses on the occupation matrix for orbitals on atom ℓ, where $m = m' = m_j$.

To study highly localized orbitals, such as d orbitals, we assume that within the augmentation region, the contributions from the basis functions approach unity:

$$\sum_i |\tilde{\phi}_i\rangle\langle\tilde{p}_i| \approx 1. \tag{2.113}$$

Thus, we can express the spin-dependent charge density as:

$$n_{m,m'}^{\tau,\sigma} = \sum_{n,\mathbf{k}}^{\sigma} f_{n,\mathbf{k}}^{\sigma} \sum_{ij} \langle\tilde{\Psi}_n^{\mathbf{k},\sigma}|\tilde{p}_i\rangle\langle\tilde{p}_i|\tilde{\Psi}_n^{\mathbf{k},\sigma}\rangle. \tag{2.114}$$

Here, the indices $(i, j) = (l, m, n)$ are related to angular momentum, magnetic angular momentum, and plane wave indices. This distinction is crucial when treating atoms with orbitals l_{ij} that share the same magnetic angular momentum. We can derive a simplified version of the previous equation:

$$n_{m,m'}^{\tau,\sigma} = \sum_{i,j} \rho_{ij}^{\sigma} \langle\tilde{\phi}_{n_i}|\tilde{\phi}_{n_j}\rangle, \tag{2.115}$$

where $\rho_{i,j}$ represents the spin density for both spin channels. This formulation introduces the Hubbard U term, which corrects the behavior of highly localized orbitals and is expressed as:

$$U_{\text{eff}} = U - J. \tag{2.116}$$

Dudarev et al.[39] further developed these implications to study transition metals with strongly correlated d electrons. Their approach emphasizes the importance of incorporating both Coulomb repulsion (U) and exchange interaction (J), allowing for a more accurate description of the electronic structure in such correlated systems.

2.6.3 Special Quasirandom Structures

VASP implements several approaches to accurately describe the electronic behavior of various systems. For example, in Section 2.6.2.4, we discussed the application of Hubbard U corrections to account for highly correlated orbitals. In this section, we will focus on the study of random alloys through the "Special Quasirandom Structures" (SQS) method[40,41]. VASP employs a two-step method for SQS, which is implemented using the Alloy Theoretic Automated Toolkit (ATAT) software package. Below, we describe key concepts of the SQS method and its application in VASP.

Consider a lattice of N atoms representing a binary random alloy $A_{1-x}B_x$, where x denotes the desired composition related to the random occupation of lattice sites by A or B atoms. To model this system, we define a set $\Lambda = \{1, 2, \ldots, N\}$ of lattice points, where each site i is characterized by a configuration $\sigma_k \in \Lambda$. Using the Ising model, we assign each configuration $\sigma_k \in \{-1, 1\}$: $+1$ if site k is occupied by an A atom, and -1 if occupied by a B atom. However, evaluating the expectation value of any physical property from the Ising model Hamiltonian,

$$\langle f(\sigma) \rangle = \sum_{\sigma}^{2^N} \rho(\sigma) f(\sigma) \tag{2.117}$$

involves 2^N terms, leading to a significant computational cost. To address this issue, the first step of the SQS method reduces the computational burden by considering clusters. A cluster is defined as a set of lattice sites (e.g., pairs, triples, etc.), and these clusters can be represented by "figures," which are determined by:

- The number of endpoints, k,

- The order, m, of nearest neighbors (NN),

- The position l of the figure in the lattice system.

Using the Ising model, we define a cluster function $\Gamma_\alpha(\sigma)$ for a given configuration σ_k as the product of spin variables $\hat{\mathbf{S}}_k = \sigma = \{\sigma_k\}_{k \in \Lambda}$ corresponding to that figure:

$$\Gamma_\alpha(\sigma) = \prod_f (l, \sigma) \tag{2.118}$$

This leads to the averaged lattice function over all positions of figures in the lattice:

$$\overline{\Gamma}_f(\sigma) = \frac{1}{ND_f} \sum_l \Gamma_f(l, \sigma) \tag{2.119}$$

where D_f accounts for the fact that a site in a cluster can contribute to multiple configurations. This concept introduces a key parameter, the "effective cluster property" ε_f, which allows us to express any physical property from Eq. 2.117 as a weighted superposition of cluster functions:

$$f(\sigma) = \sum_f \varepsilon_f(l) \Gamma_f(l, \sigma) \tag{2.120}$$

where

$$\varepsilon_f(l) = \frac{1}{N} \sum_\sigma f(\sigma) \Gamma_f(l, \sigma) \tag{2.121}$$

By substituting Eq. 2.119 into Eq. 2.120, we obtain the weighted superposition of the expectation value of the average lattice function:

$$\langle f \rangle = N \sum_f D_f \langle \overline{\Gamma}_f \rangle \varepsilon_f \tag{2.122}$$

This equation reduces the computational cost by sampling over all figures of the lattice system instead of considering all configurations as in Eq. 2.117. The second step of the SQS method involves considering a set of N_s periodic structures, $\sigma = s$, and identifying a figure $f < F$ that best mimics the random alloy $A_{1-x}B_x$. Since figures with more than $k = 3$ or $k = 4$ vertices contribute less significantly to the cluster functions, we have:

$$f(\sigma) = \sum_{s=1}^{N_s} \xi_s(\sigma) f(s) \tag{2.123}$$

and

$$\xi_s(\sigma) = \sum_{f=1}^{F} \left[\overline{\Gamma}_f(s) \right]^{-1} \overline{\Gamma}_f(\sigma) \tag{2.124}$$

where ξ_s is the weight of the s-th special configuration.

The correlation functions for a perfect random alloy R are given by:

$$\overline{\Gamma}_{k,m}(R) = \langle \overline{\Gamma}_{k,m} \rangle_R = (2x-1)^k \tag{2.125}$$

A good SQS structure approximates a random alloy's correlation functions until transferability is achieved with respect to a perfect random alloy $\langle f \rangle$. This can be measured as:

$$\langle f \rangle - f(s) = \sum_{k,m} D_{k,m} \left[(2x-1)^k - \overline{\Gamma}_{k,m}(s) \right] \varepsilon_{k,m} \tag{2.126}$$

where the prime k' indicates the exclusion of $k=0$ and $k=1$ vertices. Although the SQS method works well for small systems, a limitation arises when dealing with supercells containing a large number of atoms. In such cases, a greater number of clusters α must be considered. This is necessary because the method must evaluate each correlation function until the transferability condition in Eq. 2.126 is satisfied. To overcome this limitation, the SQS method incorporates an efficient stochastic approach: the Monte Carlo algorithm[42].

While I will not delve into the mathematical formulation of the Monte Carlo method for SQS, the essence of the approach, as developed by van de Walle et al., is to seek the optimal cluster correlation functions Γ_α by introducing an objective function:

$$Q = -wL + \sum_{\alpha \in A} |\Delta \Gamma_{\alpha'}(\sigma)\sigma| \tag{2.127}$$

where:

- w is a user-specified weight, fundamental for obtaining a good SQS,

- L is the largest distance for which $\mathrm{diam}(\alpha) < L$,

- α' is an equivalent cluster to α,

- A is a chosen set of clusters $\{\alpha\}$.

In this way, we can obtain nearly perfect quasirandom structures for larger N-atom systems. VASP computes ab initio electronic and magnetic properties $\{\langle f(s) \rangle\}$ for a candidate SQS and uses the two-step method described above to best match the objective function in Eq. 2.127 using the Monte Carlo algorithm.

Chapter 3

Methodology

The computational investigations are conducted using the Vienna Ab initio Simulation Package (VASP). The crystal structures analyzed conform to the general formula XGeTe$_3$, which includes three specific compounds:

- CrGeTe$_3$, characterized by a chromium electronic configuration of $[Ar] : 3d^5 4s^1$,

- MnGeTe$_3$, with a manganese electronic configuration of $[Ar] : 3d^6 4s^2$, and

- FeGeTe$_3$, exhibiting an iron electronic configuration of $[Ar] : 3d^7 4s^2$.

Each crystal structure is defined by a unit cell containing 10 atoms, corresponding to two formula units (f.u.) per unit cell. The common elements in these structures, germanium (Ge) and tellurium (Te), have electronic configurations of $[Ar] : 4s^2 4p^2$ and $[Ar] : 5s^2 5p^4$, respectively. Additionally, these structures share identical symmetry characteristics, corresponding to space group 147.

The electronic properties are analyzed using Projector Augmented Wave (PAW) potentials. The ab initio study begins with spin-polarized calculations on the CrGeTe$_3$ monolayer, which are subsequently extended to the MnGeTe$_3$ and FeGeTe$_3$ monolayers. The Perdew-Burke-Ernzerhof (PBE) functional is initially employed. Since the ground state of each monolayer may involve magnetic configurations (either ferromagnetic or antiferromagnetic), we systematically determine the appropriate cutoff energy and k-point mesh for each structure.

A suitable energy cutoff for all three monolayers is established, adhering to the convergence criterion outlined in Section 2.6.2.2. A plane-wave basis with a cutoff energy of 500 eV is applied, meeting a convergence criterion of less than 1 meV/f.u., achieved through a Monkhorst-Pack mesh. We optimize the k-point mesh by performing several ionic position optimizations to derive the optimal lattice parameters, as discussed in the Two-Dimensional Equation of State (Section

2.6.2.2). A convergence criterion of 1 mÅ. is adopted, leading to the selection of a $10 \times 10 \times 1$ k-point grid.

The calculations incorporate a self-consistency loop break condition of 1×10^{-6} eV to minimize undesired Pulay stress and ensure an adequate plane-wave basis set. This two-step convergence criterion ensures accurate description of any $XGeTe_3$ crystal structure, regardless of the magnetic phase. Following the determination of these parameters, we perform ionic position optimizations to obtain the ground states for both the ferromagnetic and antiferromagnetic phases, ultimately identifying the more stable magnetic configuration for each monolayer.

Subsequent calculations utilize the PBEsol functional to assess potential improvements in electronic properties compared to existing experimental and theoretical studies of the monolayers. To account for the strong correlation among d electrons in each monolayer, Hubbard U corrections are applied using both PBE and PBEsol functionals, which modify the magnetic moments of the transition metals and the potential band gaps, aligning closely with experimental and theoretical values. Full optimization calculations are conducted to evaluate the preservation of symmetry in the monolayers, facilitated by FINDSYM utility[43].

Phonon calculations are performed using a $3 \times 3 \times 1$ supercell for the stable magnetic phase of $CrGeTe_3$, and a $4 \times 4 \times 1$ supercell for both $MnGeTe_3$ and $FeGeTe_3$. The vibrational properties of these structures are studied via the "atomic force from finite displacements" method implemented in the Phonopy package[44,45]. The functional that most accurately describes each monolayer, based on previous analysis, is utilized for these calculations.

Finally, we investigate ferromagnetic random alloys at three different concentrations: $x = 0.25$, $x = 0.50$, and $x = 0.75$. These random alloys take the forms $Cr_xGeMn_{1-x}Te_3$, $Cr_xGeFe_{1-x}Te_3$, and $Fe_xGeMn_{1-x}Te_3$, each containing 24 formula units (f.u.). The alloys are generated using the mcsqs code[42], which implements a Monte Carlo algorithm to find the best special quasi-random structure. This code is part of the Alloy-Theoretic Automated Toolkit (ATAT)[46,47,48,49,42,50,51,52,53,54,55,56,57,58,59,60]. Subsequently, VASP is employed for electronic optimizations, utilizing only the PBE functional.

3.1 Flow of VASP

- VASP selects the appropriate pseudopotential method for the calculation, using the Projector-Augmented Wave (PAW) method. This method ensures a precise treatment of core electrons while maintaining computational efficiency. Additionally, VASP employs an exchange-correlation functional as specified by the user.

- The initial electronic density is computed.

- VASP iteratively constructs the Kohn-Sham Hamiltonian in a self-consistent (SC) manner.

- The electronic density is updated at each iteration, and the effective potential is recalculated until the self-consistent cycle converges to a predefined tolerance level. This tolerance, typically set by the user, is recommended to be 1×10^{-6} eV, as suggested in the VASP documentation[61]. See Fig. 3.1.
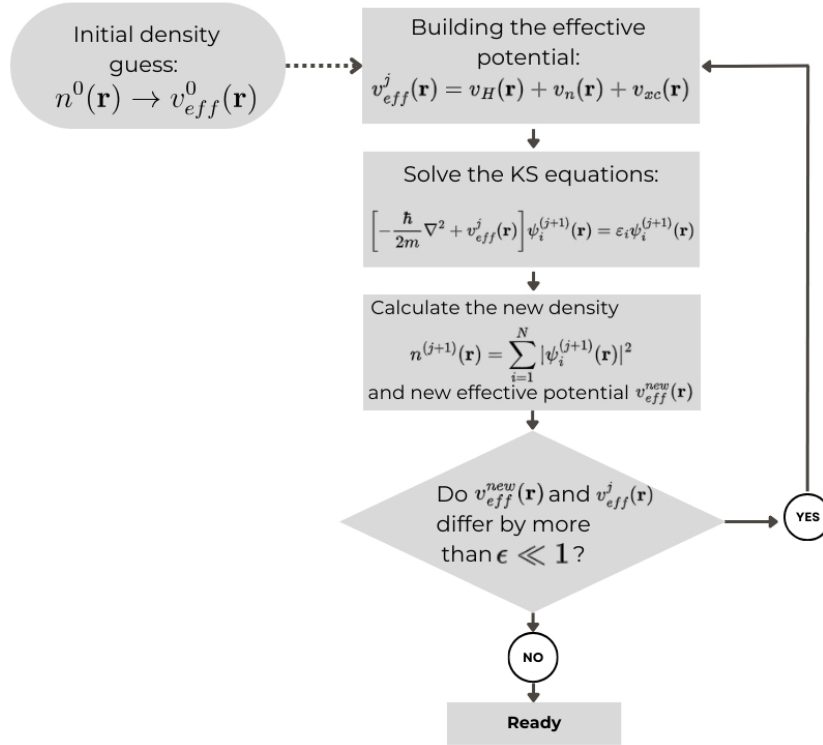
Figure 3.1: Flowchart adapted from the works of Gross[33] and Barhoumi[62], illustrating the self-consistent field (SCF) cycle in density functional theory (DFT) calculations, as implemented in VASP. The cycle starts with an initial guess for the electron density $n^0(\mathbf{r})$, followed by the construction of the effective potential $v_{\text{eff}}^j(\mathbf{r})$, incorporating the Hartree potential, exchange-correlation functional, and pseudopotentials. The Kohn-Sham equations are then solved to obtain updated wavefunctions, which are used to recalculate the electron density. This iterative process continues until the difference between successive effective potentials falls below a predefined tolerance, typically 1×10^{-6} eV[61]. The cycle ensures convergence to the ground-state electronic structure[25,63].

3.2 VASP Input and Output Files

This section provides a detailed explanation of the required input files for VASP calculations and the output files generated during the process.

3.2.1 Input Files

To perform a VASP calculation, four essential input files are required: INCAR, POSCAR, KPOINTS, and POTCAR.

3.2.1.1 INCAR

The INCAR file contains the parameters that govern various aspects of the calculation in VASP. Each parameter influences different stages of the simulation, such as electronic structure optimization, Density of States (DOS) calculations, ionic relaxation, and magnetization settings.

	GENERAL	
SYSTEM	= **XGeTe$_3$**	*# System name defined by the user*
PREC	= **Accurate**	
	ELECTRONIC OPTIMIZATION	
ENCUT	= **500**	*# Cutoff energy (in eV)*
LREAL	= **Auto**	
ISMEAR	= **0**	*# -5 for insulators, 1 or 2 for metals*
ALGO	= **Normal**	
	DOS CALCULATION	
LORBIT	= **11**	*# Necessary for DOS calculations*
NEDOS	= **4000**	*# Number of DOS points*
	IONIC RELAXATION	
ISIF	= **2**	*# Optimize ionic positions only ^{a}*
IBRION	= **2**	*# Conjugate gradient algorithm*
EDIFF	= **1E-06**	*# Energy convergence criterion*
NELM	= **100**	*# Maximum number of SCF iterations*
NSW	= **100**	*# Maximum number of ionic steps*
	MAGNETIZATION	
ISPIN	= **2**	*# Spin-polarized calculation*
MAGMOM	= **2*3 2*0 6*0**	*# Initial magnetic moments ^{b}*

^{a} By default ISIF= 3 optimizes ionic positions, cell shape, and cell volume. For monolayers, cell size relaxation is typically restricted to the x and y directions. To achieve this, modifications are made to the default 'vasp_std' script to perform the desired two-dimensional cell size optimization.

^{b} Magnetic moments are assigned according to the atom order in the POSCAR and POTCAR files. In this example: 2 atoms of X $\times \mu_B(X)$, 2 atoms of Ge $\times \mu_B(Ge)$, and 6 atoms of Te $\times \mu_B(Te)$.

Figure 3.2: Example of an INCAR file used for optimizing ionic positions while keeping the cell size and shape fixed. This file provides the total energy of the system. By applying it to different unit cell sizes, the Two-Dimensional Equation of State 2.6.2.2 can be used to determine the optimal lattice parameters. For further details, refer to the VASP manual.

Proper definition of the tags in the INCAR file is essential. Incorrect or unnecessary tag usage can lead to unrealistic results. Therefore, it is crucial to be meticulous and always refer to the official VASP manual for guidance.

3.2.1.2 POSCAR

The POSCAR file serves as a comprehensive blueprint for defining the atomic structure of materials and molecules in computational simulations. It consists of several key sections, each

containing specific information essential for accurate simulations. The first line is often a comment for human readability, providing a brief description of the system without affecting the calculation. Following this, the lattice vectors are provided, which define the shape and size of the unit cell. These vectors can be specified either in Cartesian or fractional coordinates, as illustrated in Figure 3.3.

```
  X Ge Te
1.0
 6.9068061733    0.0000000000    0.0000000000
-3.4534030866    5.9814696051    0.0000000000
 0.0000000000    0.0000000000   21.8184108734
  X Ge Te
 2 2 6
Direct
 0.666666687    0.333333343    0.500000000
 0.333333343    0.666666687    0.500000000
 0.000000000    0.000000000    0.444593012
 0.000642670    0.373393325    0.421062350
 0.999357343    0.626606705    0.578937650
 0.626606705    0.627303362    0.421062350
 0.373393325    0.372696668    0.578937650
 0.372696668    0.999357343    0.421062350
 0.627303362    0.000642670    0.578937650
```

Figure 3.3: Unit cell structure in fractional coordinates for the $XGeTe_3$ (X = Cr, Mn, Fe) monolayer, containing 10 atoms: 2 X atoms, 2 Ge atoms, and 6 Te atoms.

A scaling factor, typically provided after the lattice vectors, allows for resizing the simulation cell without altering the atomic coordinates. The file then specifies the atomic species present in the system and their corresponding quantities, whether they are standard elements or user-defined labels.

In essence, the POSCAR file provides comprehensive input for computational simulations, ensuring an accurate representation of the atomic structure within the system. For further details, refer to the official VASP manual[64].

3.2.1.3   KPOINTS

The KPOINTS file provides essential instructions for defining the sampling of the Brillouin zone, which is a fundamental region in reciprocal space related to the periodic structure of a crystal. The choice of k-points significantly affects the accuracy of the calculations by determining how the wavefunctions are sampled in this region.

k-points

0

Gamma

  6 6 1

  0 0 0

Figure 3.4: K-point grid centered at the Gamma point in the Brillouin zone. The dimensions "6 6 1" define the grid in the x, y, and z directions, respectively. The value "1" in the z direction indicates a 2D system, such as a monolayer.

Different schemes can be employed to select k-points. One commonly used method is the Monkhorst-Pack scheme, which ensures a uniform distribution of points across the Brillouin zone. The Brillouin zone is constructed from the reciprocal lattice and represents a Wigner-Seitz cell, characterized by paths that pass through high-symmetry points. For the systems under study, this path is Γ-M-K-Γ. See Fig. 3.5 for a top view of the Brillouin zone and the corresponding high-symmetry points.
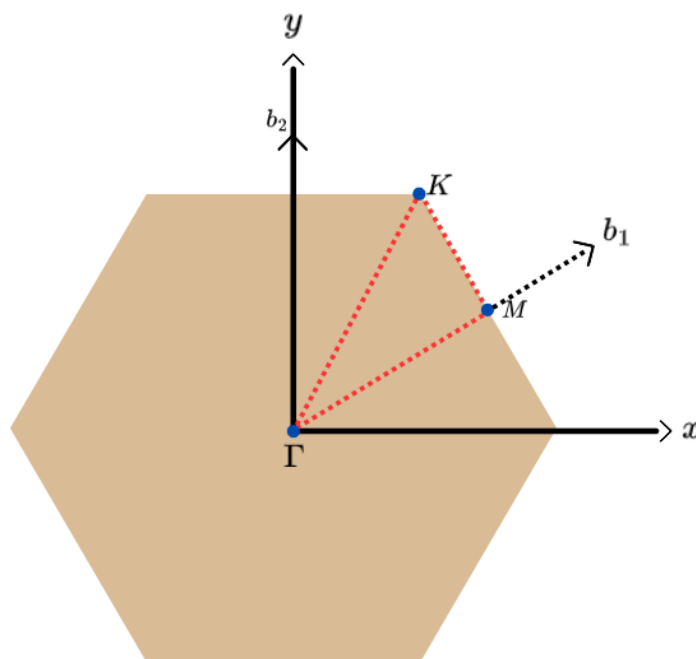
Figure 3.5: Top view of the Brillouin zone of $XGeTe_3$ monolayers, showing the path through the high-symmetry points that define its Wigner-Seitz unit cell.

Alternatively, Gamma-centered grids can be used, as shown in Figure 3.4, where the k-points are centered at the Gamma point of the Brillouin zone. The automatic generation of k-points is also an option depending on the complexity and symmetry of the system under study.

Each k-point can be assigned a weight, indicating its relative contribution to the total energy and other physical properties calculated. Proper weighting of k-points is crucial for achieving accurate and efficient results. For additional details, please refer to the official VASP manual[65].

3.2.1.4 POTCAR

The POTCAR file acts as a specialized instruction manual for computers during computational simulations. It aids the computer in comprehending the behavior of atoms within materials. Within this manual, default settings dictate the computer's calculations. These settings encompass various aspects, including the selection of exchange-correlation functionals, and the utilization of simplified atom models such as PAW.

These details are meticulously chosen based on both theoretical principles and experimental observations to ensure that the computer's predictions closely align with real-world phenomena. Recognizing the significance of the POTCAR file cannot be overstated. It serves as the bedrock for the computer's operations. By adhering to the appropriate settings and rules outlined in the POTCAR file, the computer can generate highly accurate predictions regarding the behavior of materials.

3.2.2 Output files

Upon completing ab initio calculations, several output files provide crucial information about the simulation results. These files offer insights into the electronic structure, energy convergence, atomic positions, and other important parameters. Here are brief descriptions of some of the most important output files:

3.2.2.1 OUTCAR

The `OUTCAR` file is a comprehensive output log that contains detailed information from the electronic structure calculations. This includes convergence criteria, energy values, forces acting on atoms, magnetic moments, and electronic band structure data. It serves as a valuable source for analyzing the simulation results in depth.

3.2.2.2 CONTCAR

The `CONTCAR` file contains the final atomic coordinates after the relaxation or optimization process. It is essential for visualizing the relaxed atomic structure and can be used as an input for subsequent calculations, ensuring continuity between simulations.

3.2.2.3   DOSCAR

The `DOSCAR` file provides information about the density of states (DOS), which represents the distribution of electronic states across a specified energy range. This file is essential for analyzing the electronic properties of a system and understanding its behavior under various conditions. One significant feature of this file is that it allows the calculation of the number of valence electrons, N_v, which characterize the system under study. The number of valence electrons can be computed using the following equation:

$$N_v = \int_{-\infty}^{\varepsilon_F} n(\varepsilon)\, d\varepsilon \tag{3.1}$$

Here, $n(\varepsilon)$ is the density of states as a function of energy ε, and ε_F is the Fermi energy. This integration is performed over the energy states up to the Fermi level.

3.2.2.4   PROCAR

The `PROCAR` file contains data about the projected electronic band structure, revealing the contributions of each atomic orbital to the electronic states. This information is indispensable for analyzing the electronic structure and the orbital character of the material.

3.2.2.5   OSZICAR

The `OSZICAR` file records the convergence behavior of both the electronic and ionic iterations during the calculation. It provides details on the energy convergence and the progress of the optimization, which is important for assessing the reliability and accuracy of the simulation results.

3.3   Phonon calculations using Phonopy software

The process of phonon calculation begins with a full relaxation of the atomic structure, where all degrees of freedom are optimized until the forces on each atom converge to a stable configuration. This optimization step generates a `CONTCAR` file, which contains the final equilibrium positions of atoms. Subsequently, supercells are constructed, where atoms are displaced to simulate the vibrational modes of the material. The displacements are calculated using Phonopy with the following command:

```
username:~$ phonopy -d -dim="2 2 1" -magmom="3 3 0 0 0 0 0 0 0"
```

Figure 3.6: Creation of displacements for a supercell: The command `phonopy -d -dim` generates the displaced structures required for force calculations. The `-magmom` tag is essential when dealing with magnetic atoms.

The underlying theory behind lattice vibrations is essential for understanding the thermodynamic, mechanical, and vibrational properties of crystalline solids. In a crystal, each atom oscillates around its equilibrium position, giving rise to vibrational modes, or phonons, which can either be acoustic or optical. As detailed by *Kittel*[66] and *Ashcroft*[67], these modes are crucial for explaining key properties such as heat capacity, thermal conductivity, and electron-phonon interactions.

The nuclear positions in a crystal lattice are described as:

$$\mathbf{R}_I(t) = \mathbf{R}_l + \mathbf{u}_I(t), \tag{3.2}$$

where $\mathbf{u}_I(t)$ represents the small displacement from equilibrium, and $\mathbf{R}_l$ refers to the lattice points in the crystal. These displacements are often modeled within the harmonic approximation. According to Newton's second law, the equation of motion for these displacements is:

$$M_I \ddot{\mathbf{u}}_I(t) = -\frac{\partial U}{\partial \mathbf{u}_I(t)}, \tag{3.3}$$

where M_I denotes the mass of the nucleus, and U represents the total potential energy of the system. In equilibrium, $\frac{\partial U}{\partial \mathbf{u}_I} = 0$, indicating that the system is stable. The potential energy U is expanded as a Taylor series around the equilibrium positions, and its second-order terms describe the harmonic interactions between neighboring atoms through the Born-von Karman force constants:

$$K_{ls\alpha,l's'\beta} = \frac{\partial^2 U}{\partial(R_{l\alpha} + \tau_{s\alpha})\partial(R_{l'\beta} + \tau_{s'\beta})}. \tag{3.4}$$

From here, the equation of motion for the small displacements $u_{I\alpha}(t)$ is reduced to:

$$M_I \ddot{u}_{I\alpha}(t) = -\sum_{J\beta} \Phi_{I\alpha,J\beta} u_{J\beta}(t), \tag{3.5}$$

where $\Phi_{I\alpha,J\beta}$ are the force constants. These force constants are central to constructing the dynamical matrix, defined as:

$$D_{s\alpha,s'\beta}(\mathbf{q}) = \frac{1}{(M_s M_{s'})^{1/2}} \sum_l e^{i\mathbf{q}\cdot\mathbf{R}_l} e^{i\mathbf{q}\cdot(\tau_{s'} - \tau_s)} K_{0s\alpha,ls'\beta}, \tag{3.6}$$

where $D_{s\alpha,s'\beta}(\mathbf{q})$ represents the dynamical matrix with the phonon wavevector $\mathbf{q}$. Diagonalizing this matrix yields eigenvalues, corresponding to the square of the phonon frequencies ω^2, and eigenvectors that represent the vibrational eigenmodes. The eigenvalues distinguish between

acoustic phonons, which are characterized by long-wavelength, in-phase oscillations of atoms, and optical phonons, where neighboring atoms oscillate out of phase. For a more in-depth analysis, see Chapter 7 of *Giustino*'s book[4].

After generating the displaced supercells using Phonopy, VASP is employed to compute the forces acting on atoms in each supercell, as is indicated in Eq. 3.6. This is achieved through single-point calculations, where the `INCAR` file is configured with specific tags tailored to this task, see Fig. 3.7. These calculations provide the force data necessary for constructing the force constants matrix Φ, which is crucial for determining the phonon frequencies and related vibrational properties.

	GENERAL
SYSTEM	= phonon calculation
PREC	= Normal
ISTART	= 0
ICHARG	= 2
ENCUT	= 500
SIGMA	= 0.05
ALGO	= Normal
LREAL	= .FALSE.
EDIFF	= 1E-07
NELM	= 100
	OPTIMIZATION
NSW	= 0
ISIF	= 2
POTM	= 0.5
ISMEAR	= 0
IBRION	= -1
LORBIT	= 11
ISPIN	= 2
MAGMOM	= 8*3 8*0 24*0
LWAVE	= .FALSE.
ADDGRID	= .TRUE.

Figure 3.7: Configuration of the `INCAR` file for single-point calculations. Note the use of the `IBRION=-1` tag for this purpose. The magnetic order is specified by the `MAGMOM` tag, which must be consistent with the displacements generated in Fig. 3.6.

To compute the forces from the VASP output file `vasprun.xml`, the following Phonopy command is used:

```
username:~$ phonopy -f pho_POSCAR{01..10}/vasprun.xml
```

Figure 3.8: Command to compute force sets for each displaced supercell.

The computed forces are then used to derive key phonon properties, such as phonon dispersion curves (phonon bands) and the phonon density of states (DOS). These properties are calculated using Phonopy with the following commands:

(a)

```
username:~$ phonopy -p -s band.conf
```

ATOM-NAME	= Cr Ge Te			
EIGENVECTORS	= .TRUE.			
DIM	= 2 2 1			
BAND	= 0 0 0	0.5 0 0	0.333 0.33 0	0 0 0
BAND-POINTS	= 1001			
BAND-LABELS	= Γ M K Γ			

Note: The high symmetry points (Γ, M, K) are indicative of the zone boundaries in the Brillouin zone and were obtained using the python module SeeK-path.

(b)

```
username:~$ phonopy -p -s dos.conf
```

DIM	= 3 3 1
MP	= 51 51 51
DOS	= .TRUE.
GAMMA-CENTER	= .TRUE.
FPITCH	= 0.02

Figure 3.9: Commands used to obtain (a) phonon band structure based on high-symmetry points provided by the SeeK-path tool[68,69], and (b) phonon density of states (DOS).

3.4 Implementation for generate random magnetic alloys: ATAT

The theoretical background of this software package was discussed in Section 2.6.3. Here, we outline the input files required to generate quasi-random structures. Specifically, we employ the Monte Carlo approach (mcsqs method), which requires two input files: 'rndstr.in' and 'sqscell.out'.

The first file, 'rndstr.in' (see Fig. 3.10 **a**), is similar to the POSCAR file. It contains the lattice vectors and atomic positions of the system in its unit cell form, but also allows for partial occupations of atomic positions. The second file, 'sqscell.out' (see Fig. 3.10 **b**), specifies the

supercell required to generate a Special Quasirandom Structure (SQS) that matches the desired compositions of the random alloy.

For example, we cannot use a $3 \times 3 \times 1$ supercell for a desired composition of $x = 0.25$ in a disordered (Cr,Mn) sublattice of the unit cell $Cr_xMn_{1-x}GeTe_3$, since the smallest step in that supercell would be $1/3^2 = 1/9$. Therefore, the allowed concentrations for this supercell would be: $x = 0, 1/9, 2/9, 1/3, 4/9, 5/9, 2/3, 7/9, 8/9, 1$.

(a)

```
        6.9068061733    0.0000000000    0.0000000000

        -3.4534030866   5.9814696051    0.0000000000

        0.0000000000    0.0000000000    21.8184108734
  1 0 0

  0 1 0

  0 0 1

        0.666666687     0.333333343     0.500000000     Cr=0.25,   Mn=0.75

        0.333333343     0.666666687     0.500000000     Cr=0.25,   Mn=0.75

        0.000000000     0.000000000     0.444593012     Ge

        0.000642670     0.373393325     0.421062350     Ge

        0.999357343     0.626606705     0.578937650     Te

        0.626606705     0.627303362     0.421062350     Te

        0.373393325     0.372696668     0.578937650     Te

        0.372696668     0.999357343     0.421062350     Te

        0.627303362     0.000642670     0.578937650     Te
```

(b)

$$1$$

$$\begin{matrix} 4 & 0 & 0 \\ 0 & 3 & 0 \\ 0 & 0 & 1 \end{matrix}$$

Figure 3.10: (**a**) Format of the 'rndstr.in' file, where the desired composition can be set in a unit cell lattice system. For instance, $x = 0.25$ for Cr atoms and $1 - x = 0.75$ for Mn atoms in the unit cell of $Cr_{1-x}Mn_xGeTe_3$ (with two formula units per unit cell), randomly distributed. (**b**) The structure of the 'sqscell.out' file, which generates the desired SQS (in this case, a $4 \times 3 \times 1$ supercell). This system consists of 12 unit cells (i.e., 24 formula units) with a total of 120 atoms.

With the 'rndstr.in' file, we can construct the cluster expansions required by the 'corrdump' code to obtain the cluster expansion using the following command:

```
username:~$ corrdump -l=rndstr.in -ro -noe -nop -clus -2=13.83 -3=10.56 -4=6.91
```

Note: We specify the cluster expansion for figures of two vertices up to the sixth nearest neighbor (NN), figures of three vertices up to the third NN, and figures of four vertices up to the second NN. The NN values are obtained by running the same command with a larger cutoff distance for two-vertex figures (e.g., 20 Å), ensuring that the relevant NN are included. These figures are displayed in the 'clusters.out' file.

Figure 3.11: Command used to perform cluster expansions for the $Cr_xMn_{1-x}GeTe_3$ unit cell system at $x = 0.25$, where Cr and Mn atoms are randomly distributed.

The command generates two output files: 'clusters.out', which lists all the identified clusters, and 'sym.out', which determines the space group of the system described in the 'rndstr.in' file. These files are then used for the Monte Carlo simulation, performed using the following command:

```
username:~$ mcsqs -rc
```

Note: The '-rc' flag allows for specifying the desired supercell, which is defined in the 'sqscell.out' file.

Figure 3.12: Command to generate the special quasirandom structure (SQS) using the Monte Carlo algorithm.

Finally, the 'bestsqs.out' file is generated. This file follows a format similar to that of the 'POSCAR' file and can be directly used for subsequent calculations. Due to the large supercell generated by the mcsqs method, several electronic optimization steps in VASP will be necessary within a relaxation cycle to ensure proper convergence.

Chapter 4

Results & Discussion

The magnetic monolayers under investigation belong to the trigonal system within the hexagonal family, specifically space group $P\bar{3}$ (No. 147). Prior to performing electronic structure calculations using the PBE functional, a vacuum spacing of approximately 21.8 Å was introduced to the two-dimensional system to prevent interactions between adjacent layers, thereby minimizing van der Waals interactions.

To ensure computational efficiency and accuracy, we first determined the appropriate energy cut-off for the plane wave basis set for both the ferromagnetic (FM) and antiferromagnetic (AFM) phases of each monolayer. A Monkhorst-Pack $9 \times 9 \times 1$ k-point grid was initially employed. Using a convergence criterion of less than 1 meV per formula unit (f.u.), an energy cut-off of 500 eV was selected. Additionally, Γ-centered k-point sampling was employed to preserve the hexagonal symmetry.
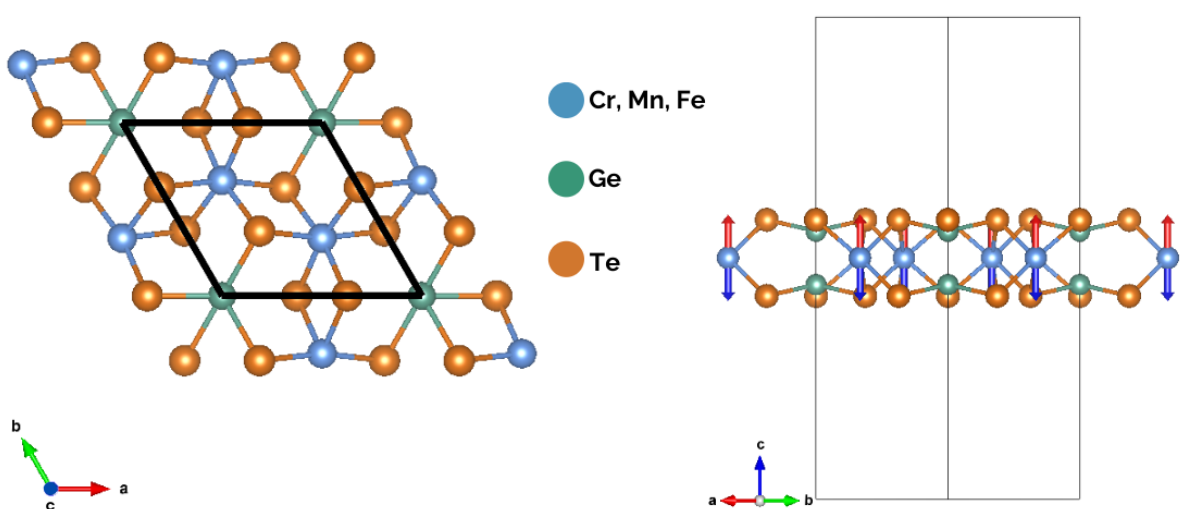
Figure 4.1: Top and side view of XGeTe$_3$($X = Cr, Mn, Fe$) monolayer

Following the determination of the energy cut-off, we optimized the k-point grid necessary for accurate electronic structure calculations. The lattice parameters were computed by fitting the two-dimensional equation of state, as described earlier. A convergence criterion of 1 mÅ was applied to obtain an optimal k-point grid of $10 \times 10 \times 1$ for subsequent calculations.
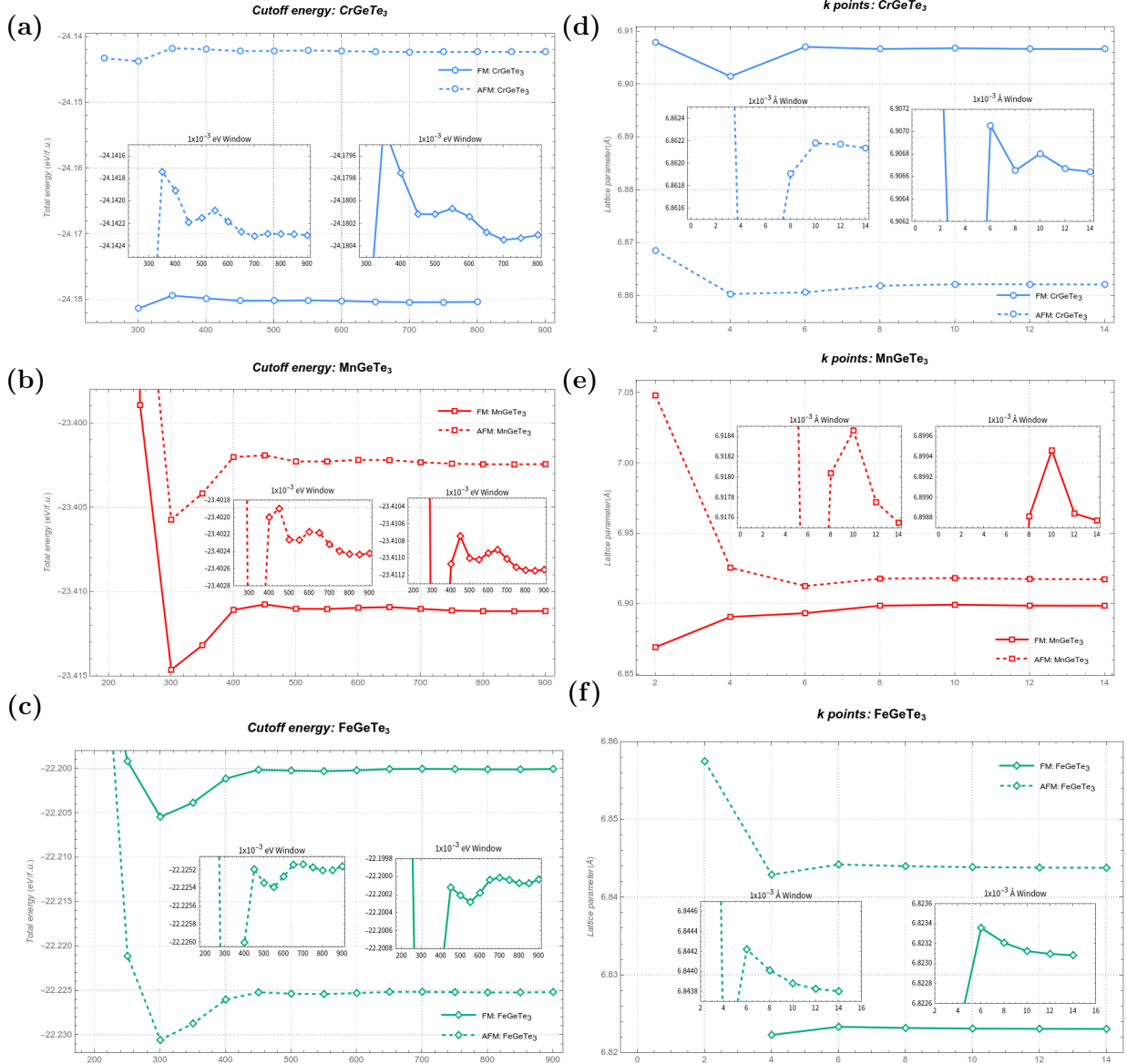
Figure 4.2: Energy convergence plots for each monolayer. Panels (**a**), (**b**), (**c**), with the x-axis representing the cut-off energy, show the convergence of energy with respect to the plane-wave cut-off for both the FM and AFM phases. The average total energy per formula unit (f.u.) converges at 400 eV, with 500 eV selected for further calculations to ensure accurate electronic property description. Panels (**d**), (**e**), (**f**), where the x-axis represents the k-point grid $k \times k \times 1$, illustrate that convergence is reached at $8 \times 8 \times 1$. A final grid of $10 \times 10 \times 1$ was used for subsequent calculations.

4.1 CrGeTe$_3$ monolayer

4.1.1 Electronic properties using PBE functional

With the cut-off energy and k-point grid established, we proceeded to determine the lattice parameters by fitting the total energy to a two-dimensional equation of state, as shown in Fig. 4.3. We recorded the total magnetic moment, the magnetic moments of the two Cr atoms, the total energy of the system, and the fractional coordinates. These calculations were performed for both ferromagnetic (FM) and antiferromagnetic (AFM) phases.
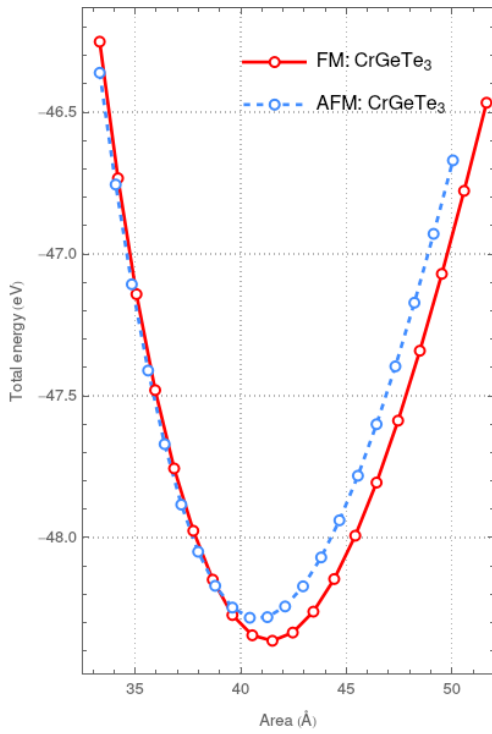
Properties	FM phase			AFM phase		
Space group	P-3			P-3		
$a = b$ (Å)	6.91			6.86		
c (Å)	21.82			21.82		
$\gamma(°)$	120			120		
Area (Å)	41.37			40.76		
Total Energy (eV)	-48.362			-48.284		
	Cr (1)	Cr (2)	Tot	Cr (1)	Cr(2)	Tot
μ_B	3.15	3.15	5.81	3.07	-3.07	0.00
	↑	↓	Tot	↑	↓	Tot
Band gap (eV)	0.51	0.39	0.37	0.46	0.46	0.46
sites	u	v	w	u	v	w
Cr(1)	0.6666	0.3333	0.5000	0.6666	0.3333	0.5000
Cr(2)	0.3333	0.6666	0.5000	0.3333	0.6666	0.5000
Ge(1)	0.0000	0.0000	0.5555	0.0000	0.0000	0.5555
Ge(2)	0.0000	0.0000	0.4445	0.0000	0.0000	0.4445
Te(1)	0.0002	0.3740	0.4211	0.0001	0.3746	0.4195
Te(2)	0.9998	0.6259	0.5789	0.9999	0.6254	0.5805
Te(3)	0.6259	0.6262	0.4211	0.6254	0.6255	0.4195
Te(4)	0.3740	0.3738	0.5789	0.3746	0.3745	0.5805
Te(5)	0.3738	0.9998	0.4211	0.3745	0.9999	0.4195
Te(6)	0.6262	0.0002	0.5789	0.6255	0.0000	0.5805

Figure 4.3: Left panel: Two-dimensional equation of state for the CrGeTe$_3$ monolayer in FM and AFM phases. The FM phase is more stable, as indicated by $\Delta E = E_{AFM} - E_{FM} = 0.04$ eV/f.u. Right panel: Electronic and magnetic properties obtained using the PBE functional for both phases, confirming semiconductor behavior in line with theoretical predictions[13,70,71].

After optimizing the lattice parameters, we conducted self-consistent calculations to examine the density of states (DOS) and the band structure, as illustrated in Fig. 4.4. In the ferromagnetic CrGeTe$_3$ monolayer, the valence band is primarily composed of Te p-orbitals, spanning the energy range from -4.61 eV to 4.12 eV. Significant hybridization between the Cr t_{2g} orbitals (d_{xy}, d_{yz}, and d_{zx}) and the Te p-orbitals is observed in the spin-down channel across the entire energy range, indicating that the PBE functional does not fully capture the localized nature of the Cr t_{2g} states.
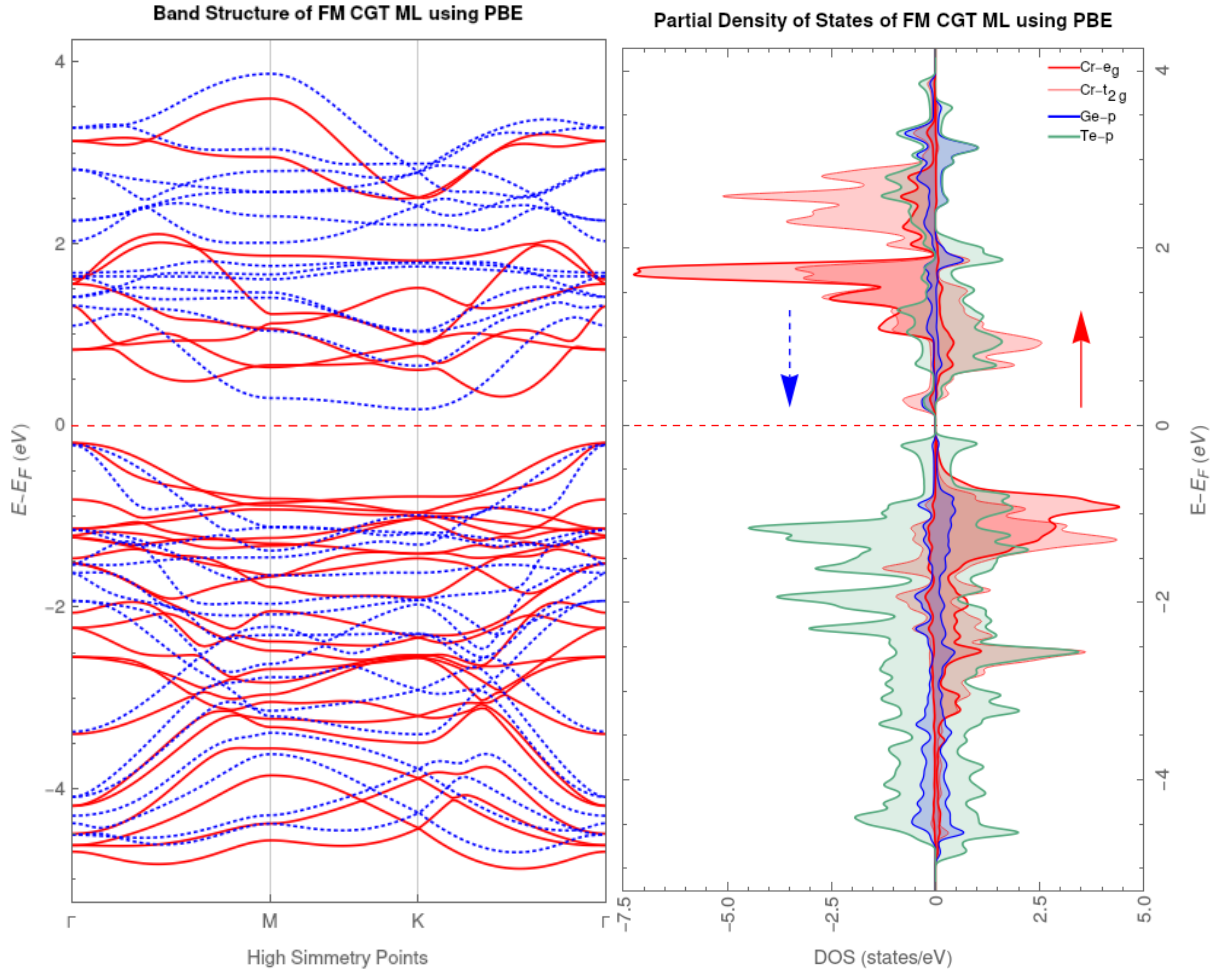
Figure 4.4: Band structure (left) and density of states (DOS) (right) for the ferromagnetic CrGeTe$_3$ monolayer calculated using the PBE functional. The red and blue colors in the band structure plot represent the spin-up and spin-down channels, respectively. In the DOS plot, the red arrow denotes the spin-up channel, and the blue dashed arrow represents the spin-down channel. The Fermi level is indicated by the red line in both plots.

4.1.2 Electronic properties using PBESol functional

To enhance the accuracy of our calculations, we employed the PBESol functional, which, to our knowledge, has not been previously applied to this monolayer in theoretical studies. PBESol was chosen for its reduced gradient density dependence, allowing for a more accurate determination of the lattice parameter.
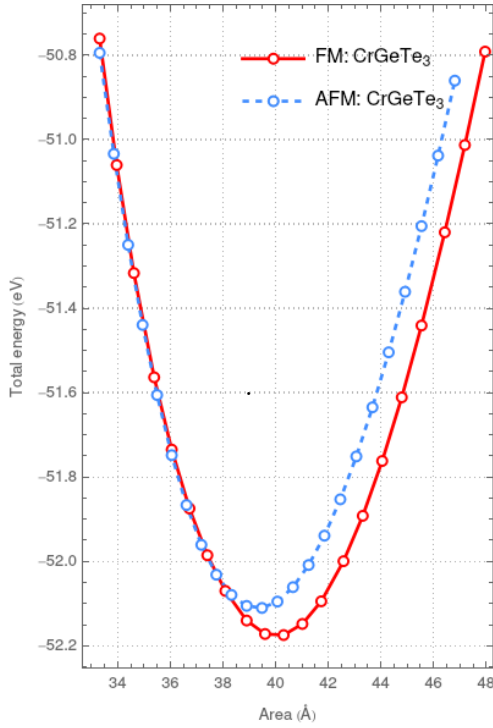
Properties	FM phase			AFM phase		
Space group	P-3			P-3		
$a = b$ (Å)	6.79			6.74		
c (Å)	21.82			21.82		
$\gamma(°)$	120			120		
Area (Å)	39.87			39.31		
Total Energy (eV)	-52.176			-52.110		
	Cr (1)	Cr (2)	Tot	Cr (1)	Cr(2)	Tot
μ_B	3.08	3.08	5.75	2.98	-2.98	0.00
	↑	↓	Tot	↑	↓	Tot
Band gap (eV)	0.49	0.18	0.18	0.32	0.32	0.32
sites	u	v	w	u	v	w
Cr(1)	0.6666	0.3333	0.5000	0.6666	0.3333	0.5000
Cr(2)	0.3333	0.6666	0.5000	0.3333	0.6666	0.5000
Ge(1)	0.0000	0.0000	0.5551	0.0000	0.0000	0.5550
Ge(2)	0.0000	0.0000	0.4449	0.0000	0.0000	0.4449
Te(1)	0.0001	0.3766	0.4221	0.0001	0.3775	0.4203
Te(2)	0.9999	0.6234	0.5779	0.9999	0.6225	0.5797
Te(3)	0.6234	0.6235	0.4211	0.6225	0.6226	0.4203
Te(4)	0.3766	0.3765	0.5779	0.3775	0.3774	0.5797
Te(5)	0.3765	0.9999	0.4221	0.3774	0.9999	0.4203
Te(6)	0.6235	0.0001	0.5779	0.6226	0.0001	0.5797

Figure 4.5: Left panel: Two-dimensional equation of state for the CrGeTe$_3$ monolayer in the FM and AFM phases. The FM phase is more stable, as indicated by $\Delta E = E_{\text{AFM}} - E_{\text{FM}} = 0.033$ eV/atom. Right panel: Electronic and magnetic properties calculated with the PBESol functional. Compared to the PBE functional (Table 4.3), PBESol shows a slight underestimation of electronic and magnetic properties. However, using the experimental lattice parameter of 6.82 Å[13], PBESol demonstrates a smaller error (0.73%) compared to PBE (0.17%).

Next, we calculated the band structures and density of states (DOS) using the PBESol functional, as shown in Fig. 4.6. Compared to the PBE functional, the band gap is significantly underestimated with the PBESol functional. Additionally, the e_g states (comprising d_{z^2} and $d_{x^2-y^2}$ orbitals) are localized across the energy range. However, as observed in Fig. 4.4, the t_{2g} states exhibit hybridization with Te p orbitals in the spin-up channel.
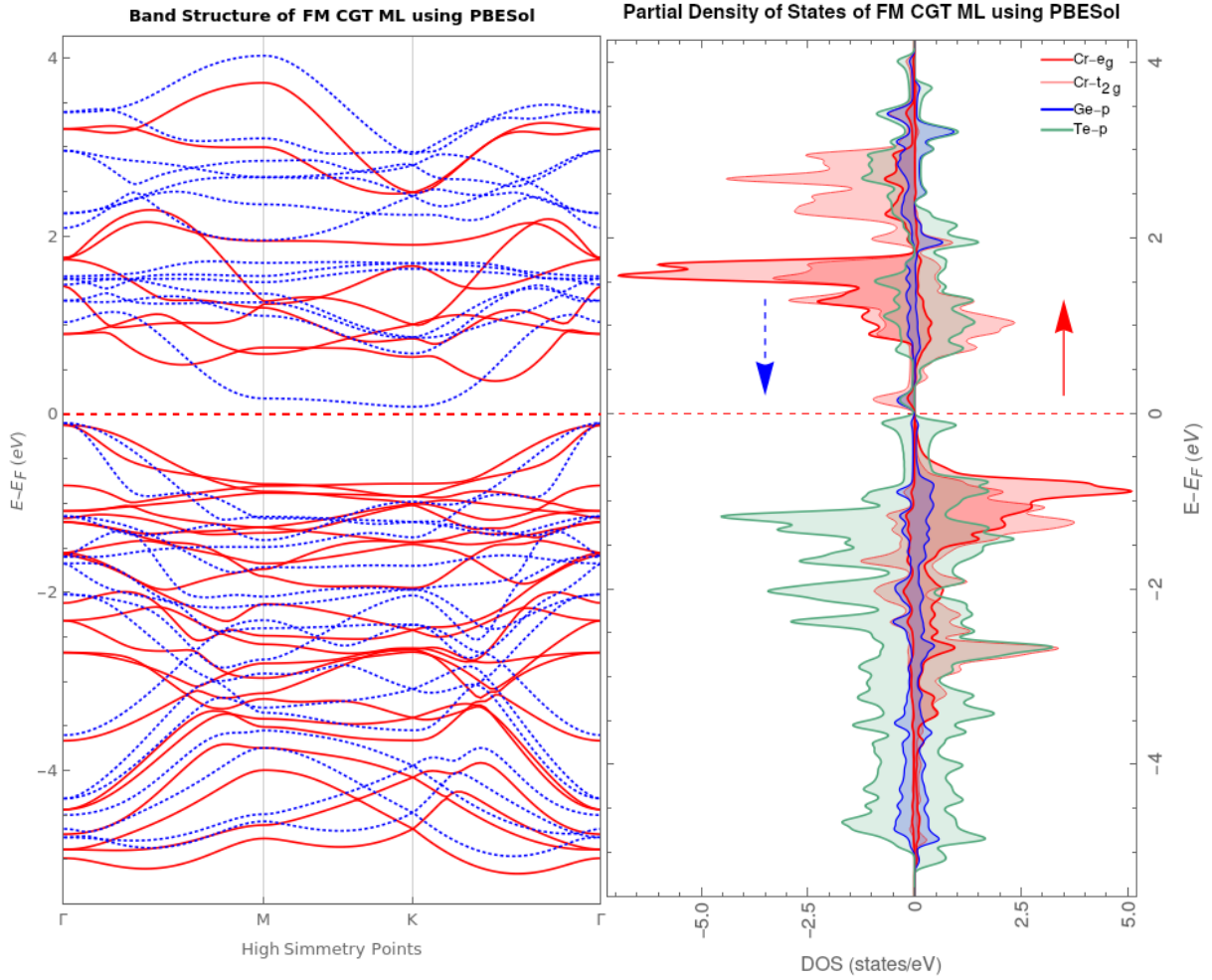
Figure 4.6: Band structure (left) and density of states (DOS) plot (right) for the ferromagnetic CrGeTe$_3$ monolayer calculated using the PBESol functional. The red and blue curves correspond to the spin-up and spin-down channels, respectively. The Fermi level is indicated by a red line in both plots. The underestimation of the band gap compared to the PBE functional is evident.

4.1.3   Magnetic and electronic properties using PBE and PBESol functionals with Hubbard U corrections

To enhance the accuracy of our computational studies on this monolayer, we incorporated Hubbard U corrections using the Dudarev approach[39]. This correction is essential for adjusting the magnetic moment and band gap of CrGeTe$_3$ in its ferromagnetic stable phase. Given the experimental lattice parameters for this two-dimensional system are $a = b = 6.82\,\text{Å}$[13], and the theoretical band gap value is $0.91\,\text{eV}$[72] obtained using the hybrid functional HSE06[73], we employed two functionals: PBE and PBESol, in conjunction with the DFT+U formalism.

To determine an appropriate value for $U_{\text{eff}} = U - J$, we set the exchange interaction J to zero and explored a range of on-site Coulomb repulsion potentials $U = U_{\text{eff}}$ from 0.0 to 3.0 eV using the PBE functional. For the PBESol functional, the range for U extended from 0.0 to 4.0 eV. These ranges were chosen to ensure the preservation of the structure with Hubbard U corrections.

Notably, the space group corresponds to number 147, and this preservation of crystal symmetry is observed for both the ferromagnetic (FM) and antiferromagnetic (AFM) phases.

Magnetic phase		Ferromagnetic						
Properties	$a = b(\text{Å})$	Total E(eV)	μ_B			Band gap (eV)		
			Cr(1)	Cr(2)	Tot	↑	↓	Tot
U=0.0	6.91	-48.442	3.13	3.13	5.79	0.58	0.38	0.36
U=0.5	6.91	-47.804	3.21	3.21	5.87	0.54	0.46	0.43
U=1.0	6.92	-47.190	3.29	3.29	5.95	0.51	0.54	0.50
U=1.5	6.93	-46.598	3.37	3.37	6.03	0.47	0.62	0.47
U=2.0	6.94	-46.029	3.45	3.45	6.11	0.43	0.70	0.43
U=2.5	6.95	-45.482	3.53	3.53	6.18	0.39	0.77	0.39
U=3.0	6.95	-44.957	3.61	3.61	6.26	0.35	0.84	0.35
U=3.5	6.96	-44.455	3.68	3.68	6.33	0.31	0.90	0.31
U=4.0	6.97	-43.973	3.75	3.75	6.40	0.27	0.96	0.27
Magnetic phase		Anti-ferromagnetic						
Properties	$a = b(\text{Å})$	Total E(eV)	μ_B			Band gap (eV)		
			Cr(1)	Cr(2)	Tot	↑	↓	Tot
U=0.0	6.86	-48.368	3.04	-3.04	0.00	0.50	0.50	0.50
U=0.5	6.87	-47.724	3.13	-3.13	0.00	0.54	0.54	0.54
U=1.0	6.88	-47.104	3.22	-3.22	0.00	0.57	0.57	0.57
U=1.5	6.89	-46.509	3.31	-3.31	0.00	0.59	0.59	0.59
U=2.0	6.90	-45.937	3.40	-3.40	0.00	0.59	0.59	0.59
U=2.5	6.91	-45.389	3.48	-3.48	0.00	0.56	0.56	0.56
U=3.0	6.92	-44.863	3.57	-3.57	0.00	0.52	0.52	0.52
U=3.5	6.93	-44.360	3.65	-3.65	0.00	0.49	0.49	0.49
U=4.0	6.94	-43.878	3.72	-3.72	0.00	0.46	0.46	0.46

Table 4.1: Calculated electronic and magnetic properties for FM and AFM phases of $CrGeTe_3$ monolayer using the PBE functional. Both magnetic phases exhibit semiconductor behavior and maintain symmetry conservation (space group 147), similar to the CGT monolayer.

Magnetic phase			Ferromagnetic					
Properties	$a = b(\text{Å})$	Total E(eV)	μ_B			Band gap (eV)		
			Cr(1)	Cr(2)	Tot	↑	↓	Tot
U=0.0	6.79	-52.230	3.06	3.06	5.74	0.55	0.18	0.18
U=0.5	6.80	-51.568	3.14	3.14	5.82	0.51	0.26	0.26
U=1.0	6.80	-50.928	3.22	3.22	5.89	0.48	0.34	0.34
U=1.5	6.81	-50.312	3.30	3.30	5.97	0.44	0.42	0.40
U=2.0	6.82	-49.717	3.38	3.38	6.05	0.40	0.50	0.40
U=2.5	6.82	-49.146	3.46	3.46	6.13	0.36	0.57	0.36
U=3.0	6.83	-48.597	3.54	3.54	6.20	0.32	0.65	0.32
U=3.5	6.84	-48.070	3.62	3.62	6.28	0.28	0.71	0.28
U=4.0	6.84	-47.565	3.69	3.69	6.35	0.24	0.78	0.24

Magnetic phase			Anti-ferromagnetic					
Properties	$a = b(\text{Å})$	Total E(eV)	μ_B			Band gap (eV)		
			Cr(1)	Cr(2)	Tot	↑	↓	Tot
U=0.0	6.74	-52.166	2.97	-2.97	0.00	0.35	0.35	0.35
U=0.5	6.75	-51.495	3.06	-3.06	0.00	0.40	0.40	0.40
U=1.0	6.76	-50.849	3.15	-3.15	0.00	0.44	0.44	0.44
U=1.5	6.76	-50.228	3.24	-3.24	0.00	0.48	0.48	0.48
U=2.0	6.77	-49.631	3.33	-3.33	0.00	0.50	0.50	0.50
U=2.5	6.78	-49.058	3.42	-3.42	0.00	0.49	0.49	0.49
U=3.0	6.79	-48.509	3.50	-3.50	0.00	0.46	0.46	0.46
U=3.5	6.80	-47.982	3.58	-3.58	0.00	0.42	0.42	0.42
U=4.0	6.80	-47.478	3.66	-3.66	0.00	0.39	0.39	0.39

Table 4.2: Calculated electronic and magnetic properties for FM and AFM phases of $CrGeTe_3$ monolayer using the PBESol functional. Both magnetic phases exhibit semiconductor behavior and maintain symmetry conservation (space group 147), similar to the CGT monolayer.

After performing extensive density functional theory (DFT) calculations to determine the electronic and magnetic properties of the ferromagnetic and antiferromagnetic phases, using two different functionals, we summarize the results as follows:
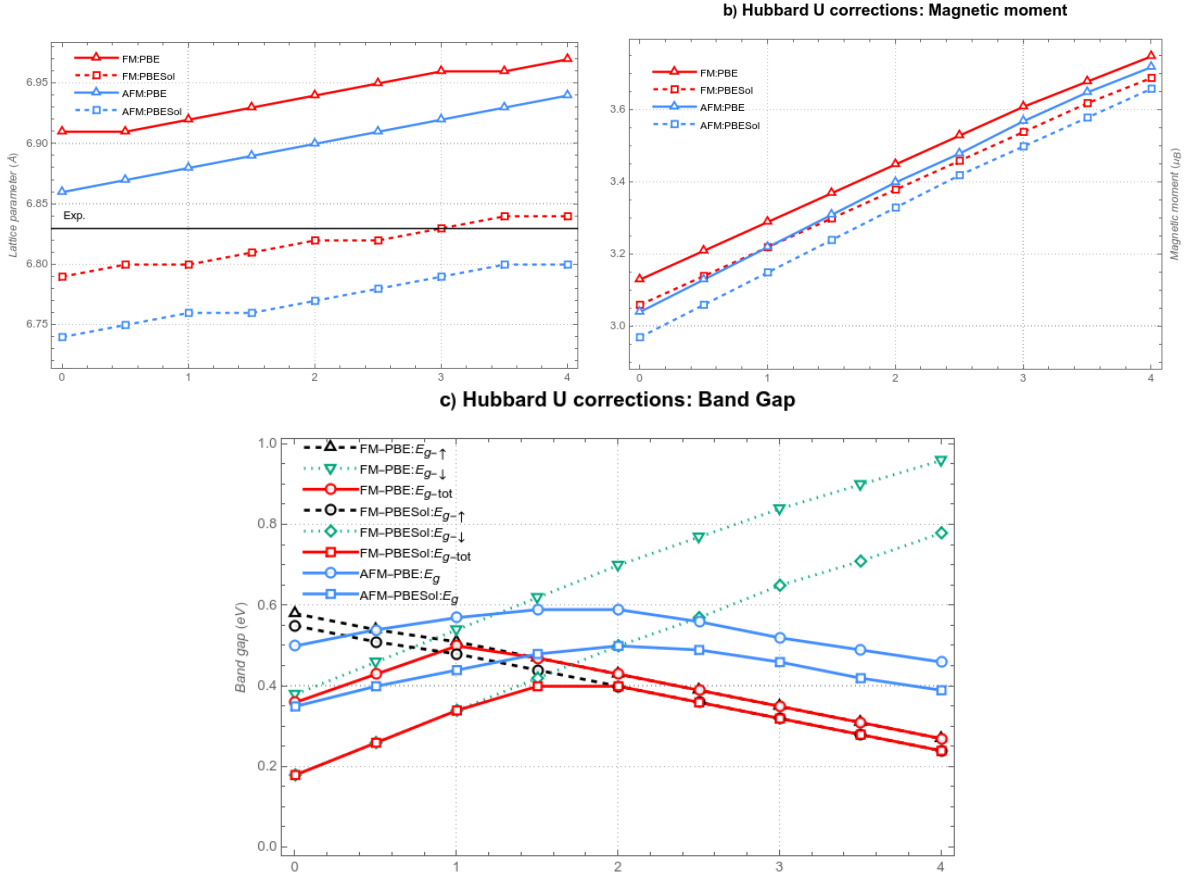
Figure 4.7: Main lattice and magnetic parameters as a function of the Hubbard U correction. In all plots, the x axis represents the Hubbard U values. (**a**) Error analysis of lattice parameters compared to experimental values, using PBE and PBESol functionals. The PBESol functional with a Hubbard U value of 3.0 eV provides the highest accuracy, showing a relative error of 0%. (**b**) Magnetic moment dependence on the Hubbard U parameter using both functionals. (**c**) Comparison of band gap corrections with PBE and PBESol functionals using Hubbard U corrections. The addition of U significantly enhances the band gap compared to the uncorrected cases. Although PBE yields a better improvement in the band gap, PBESol+$U = 3.0$ is selected for further studies due to its superior accuracy in reproducing electronic properties.

The results confirm that the PBESol functional with a Hubbard U correction of $U_{\text{eff}} = 3.0$ reproduces the lattice parameters more accurately compared to the PBE functional. This is because the PBE functional, which includes a stronger density-gradient dependence, tends to overestimate the lattice constants. While PBE is more appropriate for determining ground state energies, the choice of Hubbard $U_{\text{eff}} = 3.0$ is further validated by the improvement in the calculated band gap. Despite the absence of experimental band gap values for direct comparison, several theoretical studies using advanced functionals provide reference values. For example, using the HSE06 hybrid functional, we obtain a band gap of 0.68 eV. Incorporating spin-orbit coupling (SOC) with HSE06 yields an even lower value of 0.33 eV[74]. With $U = 3.0$, our calculated band gap shows a relative error of only 3.13%, which is significantly smaller than the 15.63% and 43.75% errors observed for the PBE and PBESol functionals, respectively, without Hubbard U. See Fig. 4.8 for further details.
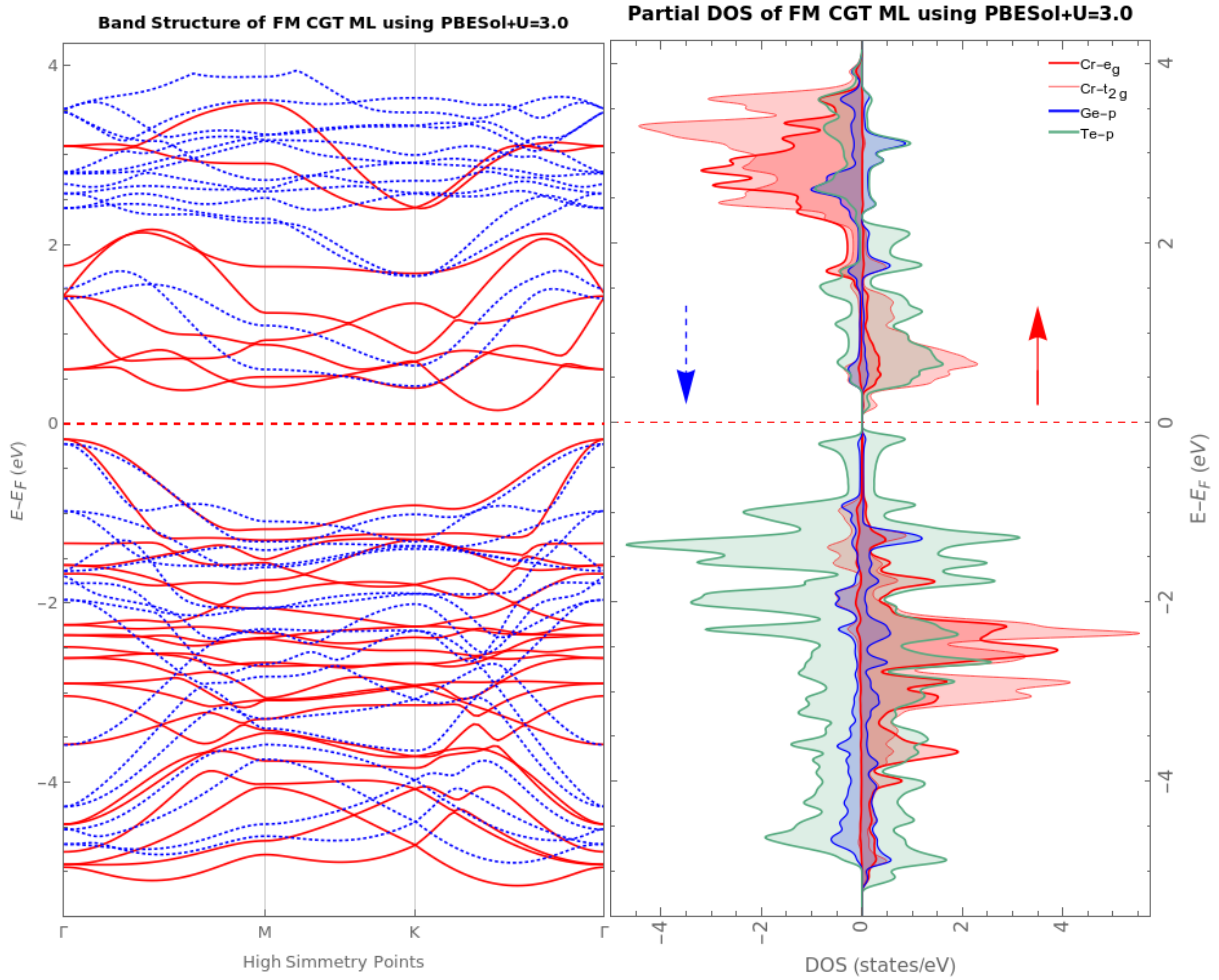
Figure 4.8: Band structure (left) and Density of States (DOS) plot (right) for the ferromagnetic CGT monolayer using the PBESol+$U(3.0)$ functional. The DOS plot shows well-localized t_{2g} and e_g orbitals.

4.1.4 Phonon Band Structure

To accurately assess the stability of the CrGeTe$_3$ monolayer, phonon calculations are essential. Phonons, which represent quantized lattice vibrations, play a key role in understanding the vibrational properties of crystal structures. These calculations provide detailed information about the vibrational modes of the lattice, offering insights into the stability, potential instabilities, or phase transitions of the material. Using a 3x3x1 ferromagnetic supercell and the PBESol+$U(3.0)$ functional, the resulting phonon band structure is presented in Fig. 4.9.
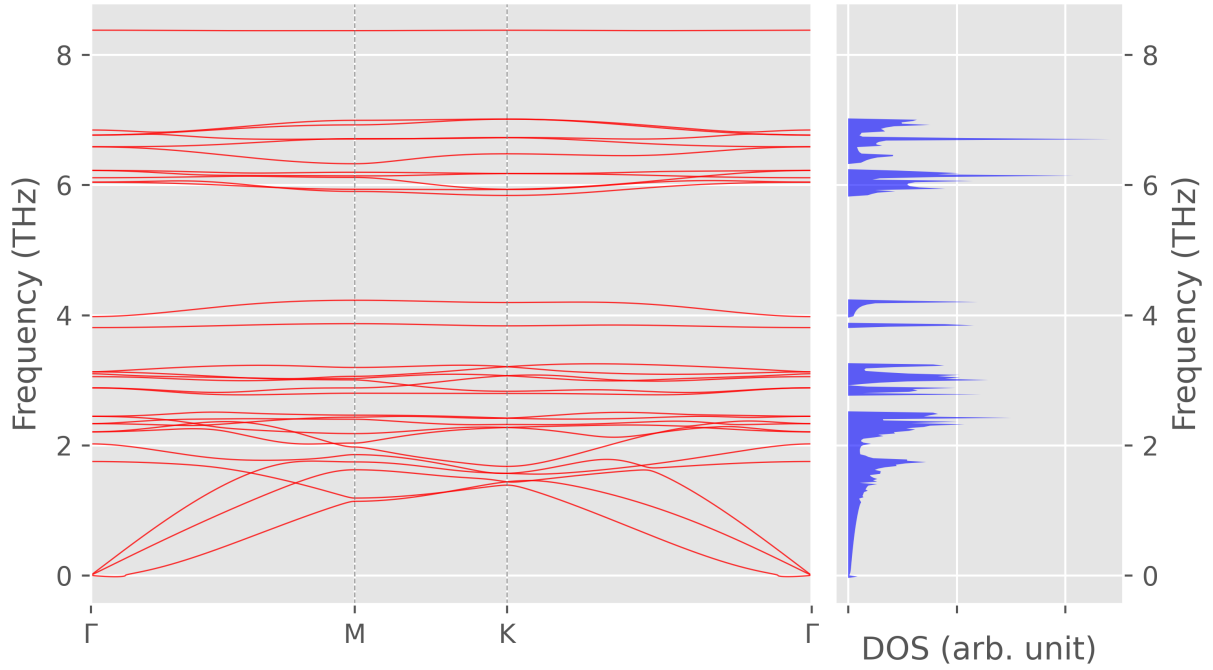
Figure 4.9: Phonon band structure (left) for the ferromagnetic CGT monolayer (3x3x1 supercell) and Density of States (DOS) plot (right). The absence of negative frequencies, along with the presence of acoustic phonons originating from the high-symmetry point Γ, confirms the stability of the CGT monolayer in its ferromagnetic phase.

4.2 MnGeTe$_3$ Monolayer

In this section, we present our findings on the MnGeTe$_3$ monolayer. This system shares the same symmetry (space group 147) as the CrGeTe$_3$ monolayer, but with manganese as the transition metal. Experimental studies on this material are yet to be reported, and to date, only theoretical studies have been carried out[18,19,20].

4.2.1 Electronic Properties Using the PBE Functional

To investigate the MnGeTe$_3$ monolayer, we employed the PBE functional. After structural relaxation of the unit cell in both ferromagnetic (FM) and antiferromagnetic (AFM) configurations, we calculated key electronic properties such as lattice parameters, magnetic moments, and total energy. These results are summarized in Figure 4.10.
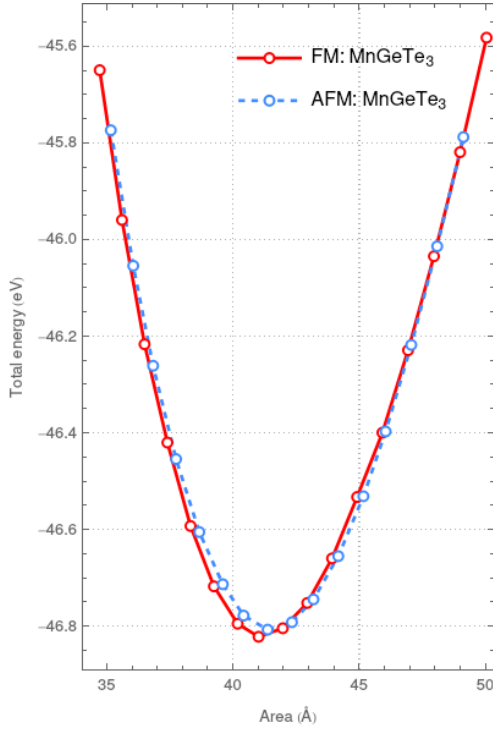
Properties	FM phase			AFM phase		
Space group	P-3 (147)			P-3 (147)		
$a = b$ (Å)	6.89			6.92		
c (Å)	21.82			21.82		
γ (°)	120			120		
Area (Å^2)	41.17			41.45		
Total Energy (eV)	-46.821			-46.807		
	Mn(1)	Mn(2)	Tot	Mn(1)	Mn(2)	Tot
μ_B	3.44	3.44	6.49	3.47	-3.47	0.00
	↑	↓	Tot	↑	↓	Tot
Band gap (eV)	0.00	0.00	0.00	0.00	0.00	0.00
sites	u	v	w	u	v	w
Mn(1)	0.6666	0.3333	0.5000	0.6666	0.3333	0.5000
Mn(2)	0.3333	0.6666	0.5000	0.3333	0.6666	0.5000
Ge(1)	0.0000	0.0000	0.5568	0.0000	0.0000	0.5565
Ge(2)	0.0000	0.0000	0.4432	0.0000	0.3333	0.4435
Te(1)	0.0001	0.3780	0.4208	0.0001	0.3774	0.4211
Te(2)	0.9999	0.6220	0.5792	0.9999	0.6226	0.5789
Te(3)	0.6220	0.6221	0.4208	0.6226	0.6228	0.4211
Te(4)	0.3780	0.3779	0.5792	0.3774	0.3772	0.5789
Te(5)	0.3779	0.9999	0.4208	0.3772	0.9999	0.4211
Te(6)	0.6221	0.0001	0.5792	0.6228	0.0001	0.5789

Figure 4.10: The left panel displays the two-dimensional equation of state for the MnGeTe$_3$ monolayer in both FM and AFM phases. The FM phase is more stable with $\Delta E = E_{AFM} - E_{FM} = 0.0014$ eV/atom. The right panel shows the calculated electronic and magnetic properties for the FM and AFM phases of MnGeTe$_3$ ML using the PBE functional. Both phases exhibit metallic behavior, maintaining the symmetry of space group 147, similar to the CrGeTe$_3$ monolayer.

As seen in Figure 4.10, the energy difference between the FM and AFM phases is $\Delta E = 0.0014$ eV/atom. Although this value exceeds 1 meV/atom, it is still insufficient to conclusively establish the FM phase as definitively more stable. Given that the system is close to the stability threshold of 1 meV/atom, it raises the question of why the PBE functional, known for accurately predicting ground state energies, does not show a larger energy distinction between the magnetic phases. Therefore, further analysis of the MnGeTe$_3$ monolayer is needed. Nevertheless, we focused on the FM phase, which appears to be the more promising magnetic configuration.

We then computed the density of states (DOS) and band structure, as shown in Figure 4.11. Despite the metallic nature revealed by the band structure in this FM phase, we hypothesize that MnGeTe$_3$ may exhibit half-metallic behavior. This inference is based on the few occupied states near the Fermi level in the spin-down channel, while the spin-up channel exhibits populated states near the Fermi level.
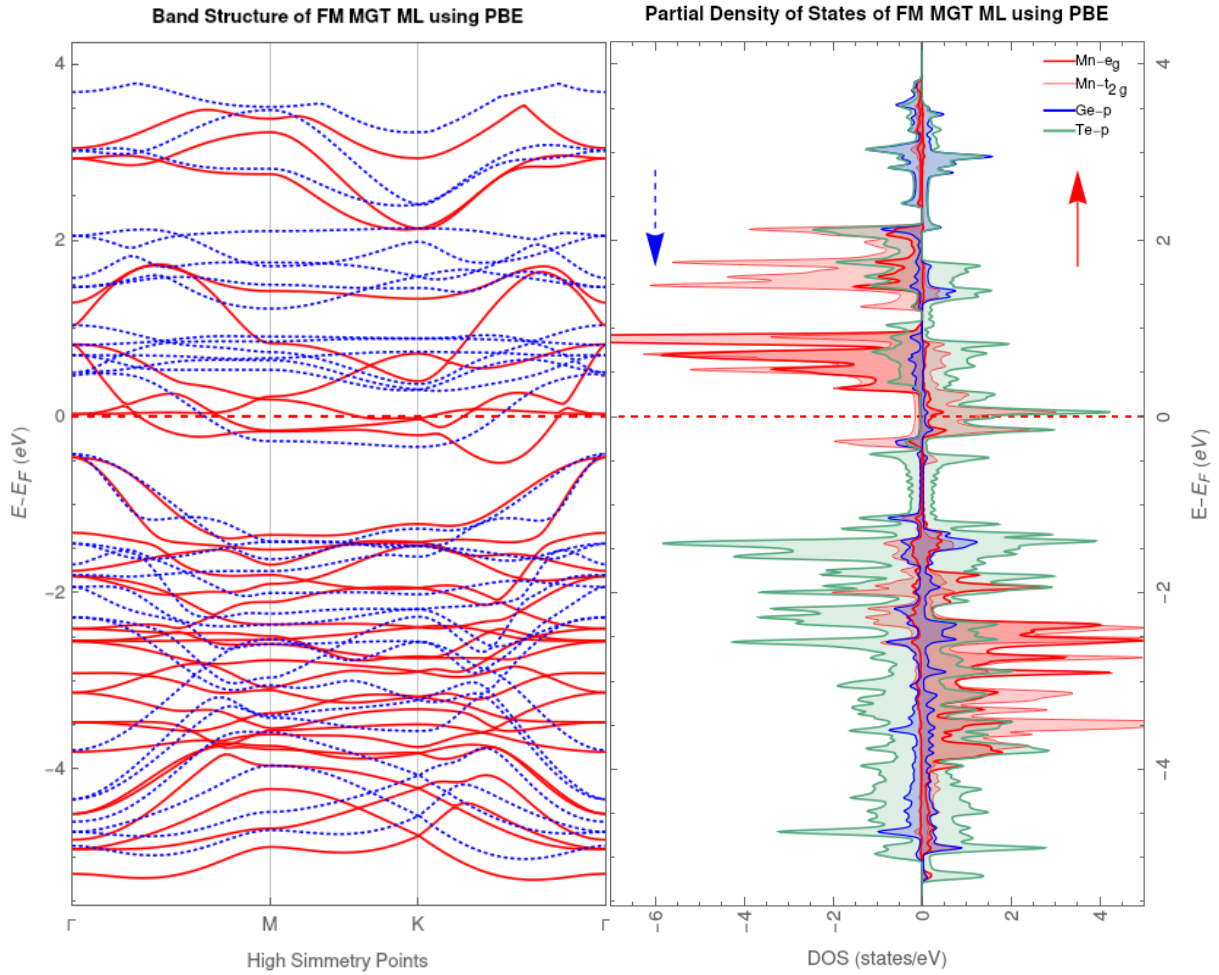
Figure 4.11: Band structure (left) and Density of States (DOS) plot (right) for the MnGeTe₃ ML using the PBE functional. Significant localized e_g states of Mn atoms are observed in the spin-down channel, while there is hybridization between t_{2g} and e_g states of Mn and p states of Te in the spin-up channel.

4.2.2 Electronic Properties Using the PBESol Functional

We employed the PBESol functional, which provides a more accurate lattice parameter approximation compared to the standard PBE functional. Although no experimental data is available for this specific monolayer, the calculated results are shown in Figure 4.12. The PBESol functional slightly underestimates the magnetic moment relative to PBE. Additionally, while the ferromagnetic (FM) phase is energetically more favorable, the energy difference between the FM and antiferromagnetic (AFM) phases is minimal ($\Delta E = 0.007$ eV/atom), similar to the results obtained with the PBE functional. Consequently, we focus our analysis on the FM phase.
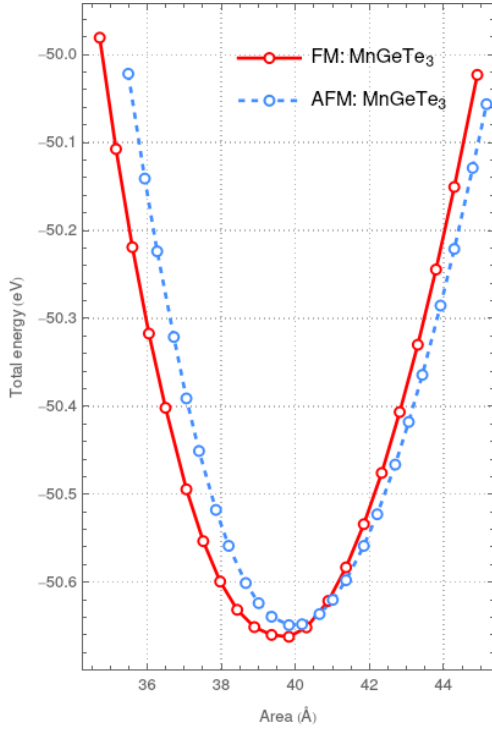
Properties	FM phase			AFM phase		
Space group	P-3 (147)			P-3 (147)		
$a = b$ (Å)	6.76			6.79		
c (Å)	21.82			21.82		
$\gamma(°)$	120			120		
Area (Å^2)	39.62			39.94		
Total Energy (eV)	-50.663			-50.649		
μ_B	Mn(1)	Mn(2)	Total	Mn(1)	Mn(2)	Total
	3.20	3.20	6.07	3.05	-3.05	0.00
Band gap (eV)	↑	↓	Total	↑	↓	Total
	0.00	0.00	0.00	0.00	0.00	0.00
Sites	u	v	w	u	v	w
Mn(1)	0.6666	0.3333	0.5000	0.6666	0.3333	0.5000
Mn(2)	0.3333	0.6666	0.5000	0.3333	0.6666	0.5000
Ge(1)	0.0000	0.0000	0.5563	0.0000	0.0000	0.5561
Ge(2)	0.0000	0.0000	0.4437	0.0000	0.0000	0.4439
Te(1)	0.0000	0.3824	0.4225	0.0000	0.3838	0.4242
Te(2)	0.9999	0.6176	0.5775	0.9999	0.6162	0.5758
Te(3)	0.6176	0.6176	0.4225	0.6162	0.6162	0.4242
Te(4)	0.3824	0.3824	0.5775	0.3838	0.3838	0.5758
Te(5)	0.3824	0.9999	0.4225	0.3838	0.9999	0.4242
Te(6)	0.6176	0.0000	0.5775	0.6162	0.0000	0.5758

Figure 4.12: The left panel displays the two-dimensional equation of state for the MnGeTe$_3$ monolayer in both FM and AFM phases. The FM phase is slightly more stable with $\Delta E = E_{\text{AFM}} - E_{\text{FM}} = 0.007$ eV/atom. The right panel shows the electronic and magnetic properties for both phases using the PBESol functional. Both phases exhibit metallic behavior and retain the symmetry of space group 147, similar to the CrGeTe$_3$ monolayer.

The density of states (DOS) and band structure plots for the FM phase, as shown in Figure 4.13, further confirm that the system does not exhibit half-metallic behavior. Instead, the results point towards a conventional metallic character.
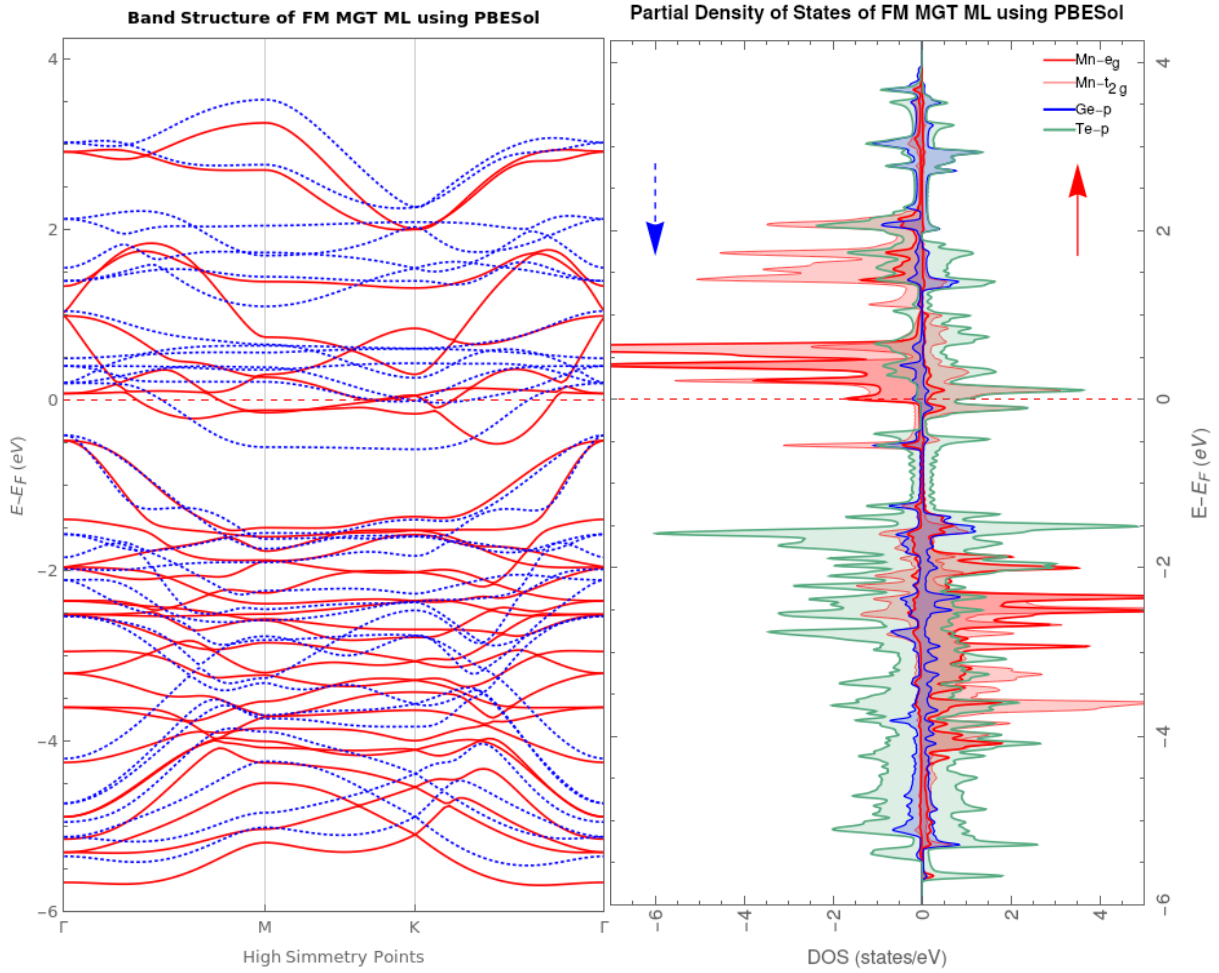
Figure 4.13: Band Structure (left) and Density of States (DOS) plot (right) for the ferromagnetic MnGeTe₃ monolayer using the PBESol functional. The DOS plot shows that the t_{2g} orbitals are more localized in the spin-down channel (above the Fermi level), while in the spin-up channel (below the Fermi level), these states are clearly hybridized with the p orbitals of Te.

4.2.3 Magnetic and electronic properties using PBE and PBESol functionals with Hubbard U corrections

The results obtained with the PBE and PBESol functionals provide a partial description of the half-metallic behavior. To better capture the strongly localized d orbitals of Mn, we employ Hubbard U corrections. This approach refines the total energies, clarifying the stability of the ferromagnetic (FM) phase. Notably, the energy difference between the antiferromagnetic (AFM) and FM phases, defined as $\Delta E = E_{AFM} - E_{FM}$, is marginal at 1.14 meV/atom for both functionals, indicating that the FM phase is nearly degenerate.

Utilizing Dudarev's approach for accounting for Hubbard U corrections, we aim to achieve a clearer FM ground state and a more accurate description of the half-metallic behavior. The results are summarized in Tables 4.3 and 4.4.

Magnetic phase			Ferromagnetic						
Properties	$a = b$(Å)	Total E(eV)	μ_B			Band gap (eV)			
			Mn(1)	Mn(2)	Tot	↑	↓	Tot	
U=0.0	6.89	-46.830	3.43	3.43	6.46	0.00	0.00	0.00	
U=0.5	6.93	-46.269	3.89	3.89	7.51	0.00	0.34	0.00	
U=1.0	6.94	-45.795	3.99	3.99	7.61	0.00	0.44	0.00	
U=1.5	6.94	-45.354	4.09	4.09	7.69	0.00	0.53	0.00	
U=2.0	6.95	-44.944	4.17	4.17	7.78	0.00	0.63	0.00	
U=2.5	6.96	-44.565	4.25	4.25	7.85	0.00	0.71	0.00	
U=3.0	6.96	-44.213	4.31	4.31	7.92	0.00	0.79	0.00	
U=3.5	6.97	-43.886	4.38	4.38	7.98	0.00	0.86	0.00	
U=4.0	6.97	-43.582	4.43	4.43	8.04	0.00	0.92	0.00	
U=4.5	6.98	-43.299	4.48	4.48	8.09	0.00	0.98	0.00	
Magnetic phase			Anti-ferromagnetic						
Properties	$a = b$(Å)	Total E(eV)	μ_B			Band gap (eV)			
			Mn(1)	Mn(2)	Tot	↑	↓	Tot	
U=0.0	6.92	-46.812	3.44	-3.44	0.00	0.00	0.00	0.00	
U=0.5	6.91	-46.231	3.76	-3.76	0.00	0.00	0.00	0.00	
U=1.0	6.91	-45.723	3.91	-3.91	0.00	0.00	0.00	0.00	
U=1.5	6.91	-45.266	4.04	-4.04	0.00	0.00	0.00	0.00	
U=2.0	6.91	-44.849	4.14	-4.14	0.00	0.00	0.00	0.00	
U=2.5	6.91	-44.465	4.23	-4.23	0.00	0.00	0.00	0.00	
U=3.0	6.92	-44.113	4.31	-4.31	0.00	0.00	0.00	0.00	
U=3.5	6.92	-43.787	4.37	-4.37	0.00	0.00	0.00	0.00	
U=4.0	6.92	-43.486	4.43	-4.43	0.00	0.00	0.00	0.00	
U=4.5	6.92	-43.209	4.48	-4.48	0.00	0.00	0.00	0.00	

Table 4.3: Calculated electronic and magnetic properties for FM and AFM phases of MnGeTe$_3$ monolayers using the PBE functional with Hubbard U corrections.

Magnetic phase			Ferromagnetic					
Properties	$a = b$(Å)	Total E(eV)	μ_B			Band gap (eV)		
			Mn(1)	Mn(2)	Tot	↑	↓	Tot
U=0.0	6.76	-50.684	3.11	3.11	5.86	0.00	0.00	0.00
U=0.5	6.77	-50.005	3.46	3.46	6.51	0.00	0.00	0.00
U=1.0	6.80	-49.444	3.91	3.91	7.52	0.00	0.19	0.00
U=1.5	6.81	-48.973	4.00	4.00	7.61	0.00	0.28	0.00
U=2.0	6.81	-48.535	4.09	4.09	7.69	0.00	0.37	0.00
U=2.5	6.81	-48.127	4.17	4.17	7.77	0.00	0.00	0.00
U=3.0	6.82	-47.748	4.25	4.25	7.86	0.00	0.00	0.00
U=3.5	6.81	-47.397	4.32	4.32	7.96	0.00	0.00	0.00
U=4.0	6.81	-47.072	4.38	4.38	8.05	0.00	0.00	0.00
U=4.5	6.81	-46.769	4.43	4.43	8.12	0.00	0.00	0.00
Magnetic phase			Anti-ferromagnetic					
Properties	$a = b$(Å)	Total E(eV)	μ_B			Band gap (eV)		
			Mn(1)	Mn(2)	Tot	↑	↓	Tot
U=0.0	6.79	-50.670	2.95	-2.95	0.00	0.00	0.00	0.00
U=0.5	6.80	-49.974	3.47	-3.47	0.00	0.00	0.00	0.00
U=1.0	6.79	-49.401	3.78	-3.78	0.00	0.00	0.00	0.00
U=1.5	6.77	-48.898	3.94	-3.94	0.00	0.00	0.00	0.00
U=2.0	6.77	-48.448	4.06	-4.06	0.00	0.00	0.00	0.00
U=2.5	6.77	-48.037	4.16	-4.16	0.00	0.00	0.00	0.00
U=3.0	6.76	-47.662	4.25	-4.25	0.00	0.00	0.00	0.00
U=3.5	6.76	-47.316	4.32	-4.32	0.00	0.00	0.00	0.00
U=4.0	6.75	-46.996	4.39	-4.39	0.00	0.00	0.00	0.00
U=4.5	6.74	-46.701	4.44	-4.44	0.00	0.00	0.00	0.00

Table 4.4: Calculated electronic and magnetic properties for FM and AFM phases of MnGeTe$_3$ monolayers using the PBESol functional with Hubbard U corrections.

Those results are summarized in the following figure:
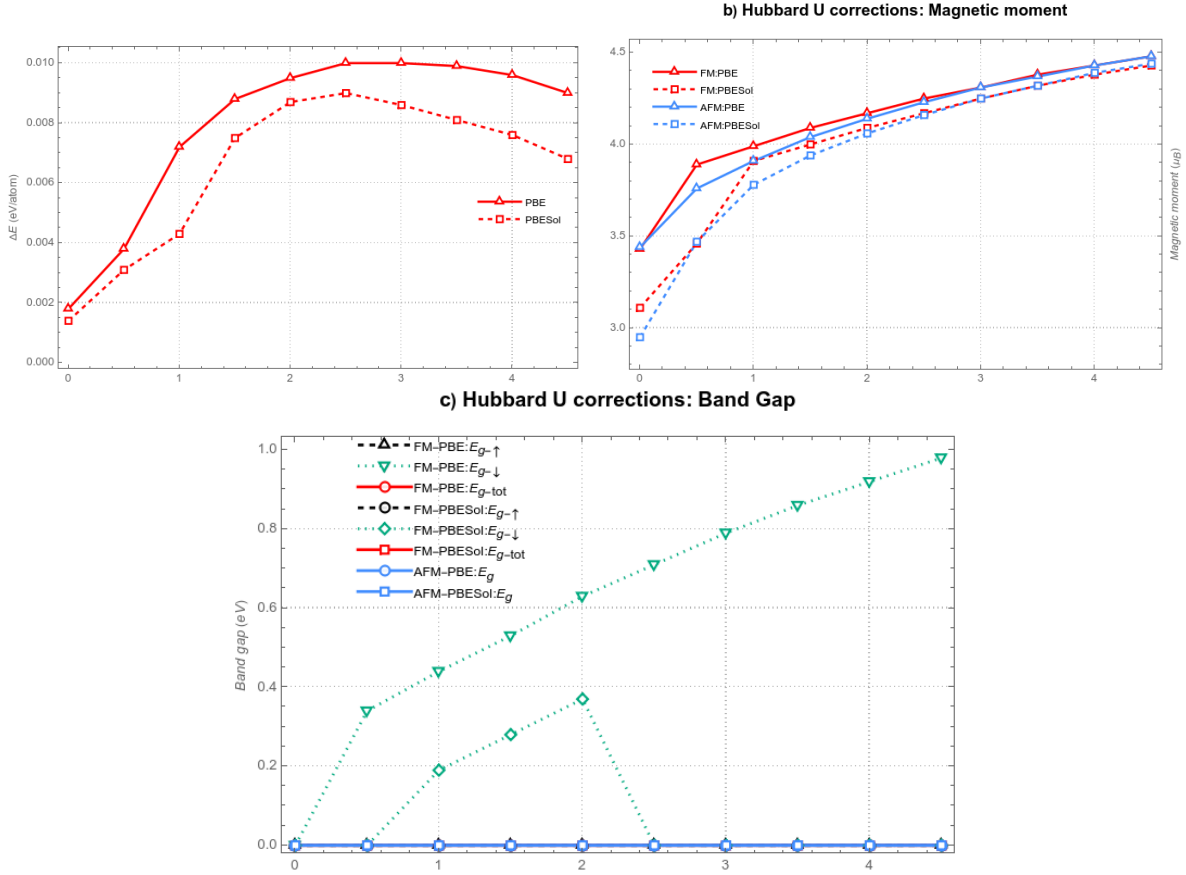
Figure 4.14: **(a)** Energy difference between FM and AFM phases for PBE and PBESol functionals with various Hubbard $U_{eff} = U - J$ corrections ranging from 0 to 4.5 eV. The PBE functional exhibits a stronger FM phase with $U = 2.5$ or $U = 3.0$ eV compared to PBESol with similar Hubbard corrections, indicating improved accuracy in ground state energies using PBE. **(b)** Magnetic moments as a function of Hubbard U parameters. **(c)** Band gap for both spin channels as a function of Hubbard U corrections, demonstrating clear half-metallic (HM) behavior in the FM phase with PBE and Hubbard U corrections. Notably, for PBEsol and Hubbard U corrections, the band gap for the spin-down channel increases up to $U = 2.0$ eV before decreasing, exhibiting metallic behavior at higher U values.

Figure 4.14 illustrates that the PBE functional with Hubbard U corrections effectively approximates the half-metallic behavior of the FM phase. However, it is essential to consider the magnetic moment, especially in the absence of experimental data. To address this, we employ the hybrid HSE06 functional, which predicts a magnetic moment of 4.23 μ_B and a spin-down band gap of 1.47 eV. Although Hubbard U corrections can approximate this band gap, as demonstrated in Figure 4.12 (a), they do not necessarily stabilize the FM phase. Notably, a Hubbard U value of 2.5 eV provides the closest match to the HSE06 magnetic moment, yielding a minimal relative error of 0.47%.

Figure 4.15: Band structure (left) and density of states (DOS) plot (right) for the ferromagnetic MGT monolayer using the PBE+U(2.5) functional. The red and blue colors represent spin-up and spin-down channels in the band structure plot. The DOS plot clearly indicates well-behaved localization for both t_{2g} and e_g orbitals, demonstrating clear half-metallic behavior. The spin-down channel exhibits semiconductor behavior, while the spin-up channel shows metallic characteristics.

4.2.4 Phonon Band Structure

Building on the previous analysis, we now investigate the phonon properties to assess the thermal stability of the ferromagnetic (FM) phase using the PBE+U(2.5) functional. Phonon calculations were performed using a 4x4x1 supercell to ensure accuracy and capture potential instabilities. The phonon density of states (DOS) and band structure, illustrated in Figure 4.16, indicate that the system exhibits no negative frequencies, signifying dynamic stability. The phonon band structure (left) confirms the presence of acoustic phonons originating from the high-symmetry point Γ, further supporting the stability of the ferromagnetic phase of the monolayer.

This stability analysis complements our previous findings, reinforcing that the PBE+U(2.5) functional not only provides an accurate description of the electronic properties but also predicts a stable FM phase under thermal conditions.
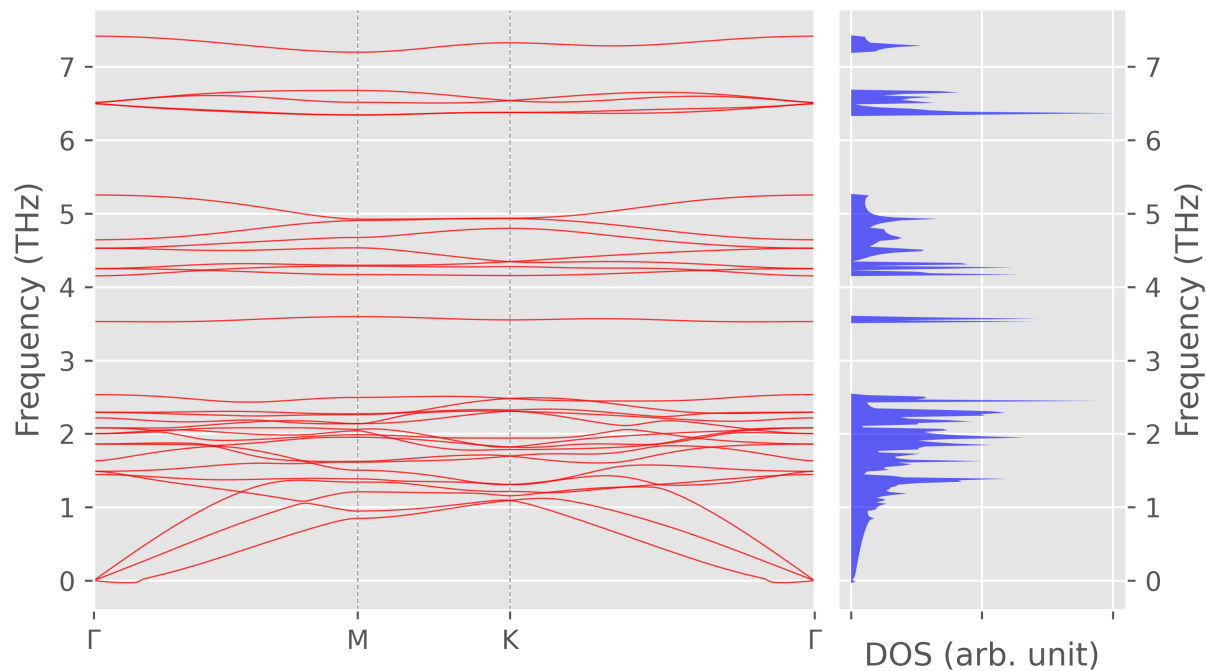
Figure 4.16: Phonon band structure (left) and phonon density of states (DOS) (right) for the ferromagnetic MGT monolayer with a 4x4x1 supercell.

4.3 FeGeTe$_3$ Monolayer

4.3.1 Electronic Properties Using PBE Functional

Finally, we present the analysis of the FeGeTe$_3$ monolayer, initially studied using the PBE functional. In our calculations, the lattice parameters were optimized, resulting in a change of symmetry from space group 147 to 162 for both magnetic phases (see Figure 4.17). This adjustment indicates unusual magnetic behavior in the monolayer, warranting further investigation.
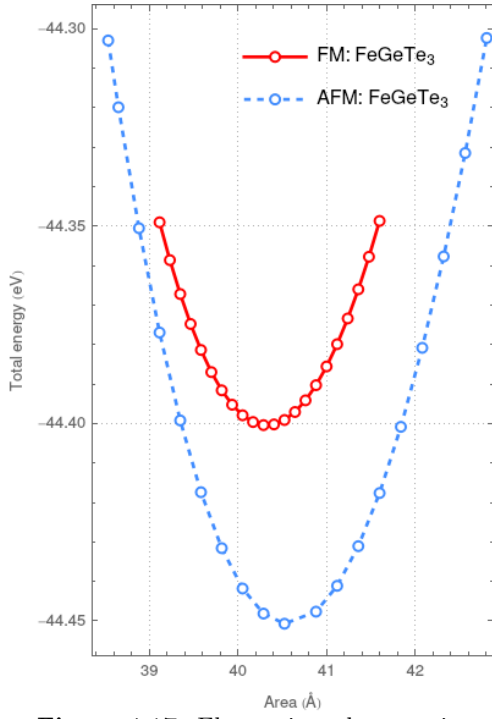
Properties	FM phase			AFM phase		
Space Group	P-3 (162)			P-3 (162)		
$a = b$ (Å)	6.82			6.85		
c (Å)	21.82			21.82		
$\gamma(°)$	120			120		
Area (Å)	40.33			40.57		
Total Energy (eV)	-44.400			-44.451		
	Fe(1)	Fe(2)	Tot	Fe(1)	Fe(2)	Tot
μ_B	1.21	1.21	2.12	1.38	-1.38	0.00
	↑	↓	Tot	↑	↓	Tot
Band Gap (eV)	0.39	0.00	0.00	0.23	0.23	0.00
Sites	u	v	w	u	v	w
Fe(1)	0.6666	0.3333	0.5000	0.6666	0.3333	0.5000
Fe(2)	0.3333	0.6666	0.5000	0.3333	0.6666	0.5000
Ge(1)	0.0000	0.0000	0.5562	0.0000	0.0000	0.5563
Ge(2)	0.0000	0.0000	0.4438	0.0000	0.0000	0.4437
Te(1)	0.0000	0.3866	0.4287	0.0000	0.3866	0.4291
Te(2)	0.9999	0.6134	0.5713	0.9999	0.6134	0.5709
Te(3)	0.6134	0.6134	0.4287	0.6134	0.6134	0.4291
Te(4)	0.3865	0.3865	0.5713	0.3866	0.3866	0.5709
Te(5)	0.3865	0.9999	0.4287	0.3866	0.9999	0.4291
Te(6)	0.6134	0.0000	0.5713	0.6134	0.0000	0.5709

Figure 4.17: Electronic and magnetic properties of FeGeTe$_3$ monolayer for ferromagnetic (FM) and antiferromagnetic (AFM) phases using the PBE functional. The energy difference $\Delta E = -0.026\,\text{eV/f.u.}$ suggests that the antiferromagnetic (AFM) phase may be more stable.

The energy difference $\Delta E = E_{FM} - E_{AFM} = -0.026\,\text{eV/f.u.}$ indicates a preference for the antiferromagnetic (AFM) phase over the ferromagnetic (FM) phase. This observation directs our focus toward the AFM phase for subsequent analysis.

In Figure 4.18, we present the band structure and density of states (DOS) for the FeGeTe$_3$ monolayer in the AFM phase. The DOS reveals a prominent delocalization of 'd' states and significant hybridization between Fe 'd' and Te 'p' orbitals. This hybridization is evident both below and above the Fermi level, influencing the electronic properties of the monolayer.
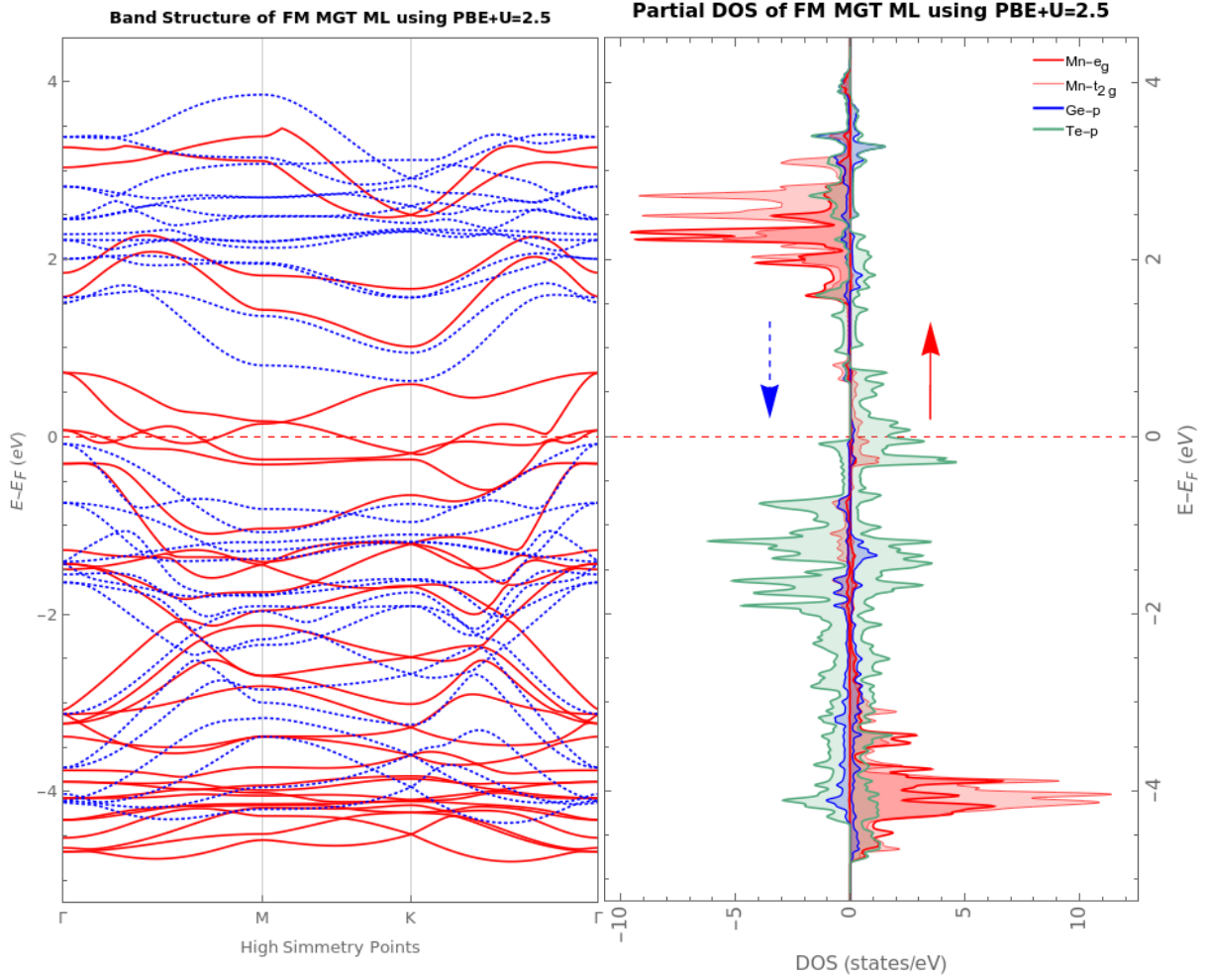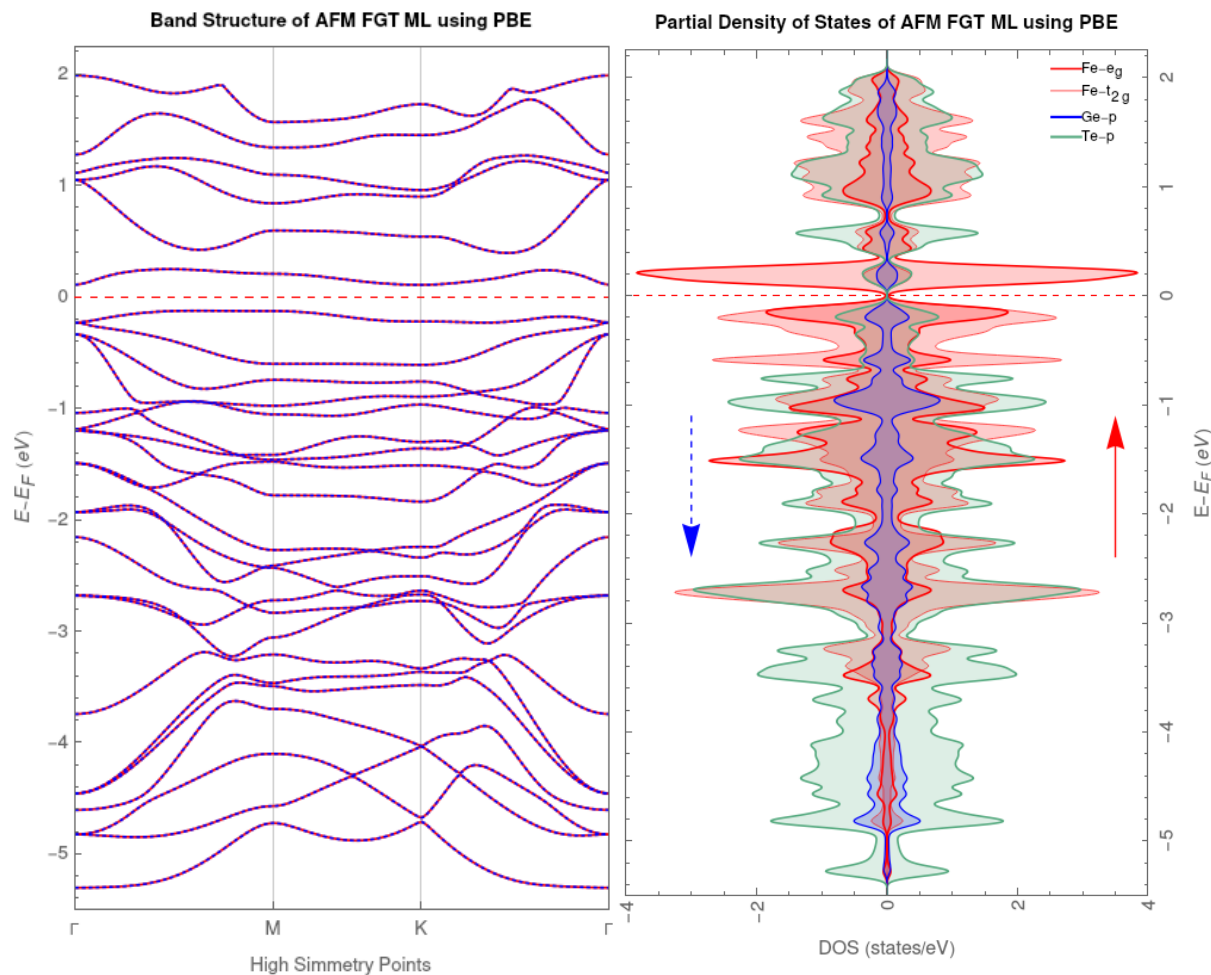
Figure 4.18: Band structure (left) and density of states (DOS) plot (right) for the AFM phase of FeGeTe₃ monolayer using the PBE functional. The AFM phase exhibits semiconductor behavior.

4.3.2 Electronic properties using PBESol functional

We next investigate the electronic properties of the FeGeTe₃ monolayer using the PBESol functional. The calculated energy difference, $\Delta E = 0.002\,\text{eV/f.u.}$, indicates a slight preference for ferromagnetic behavior (see Fig. **??**). However, this energy difference is notably smaller than that observed with the PBE functional, where an antiferromagnetic phase was determined to be more stable.
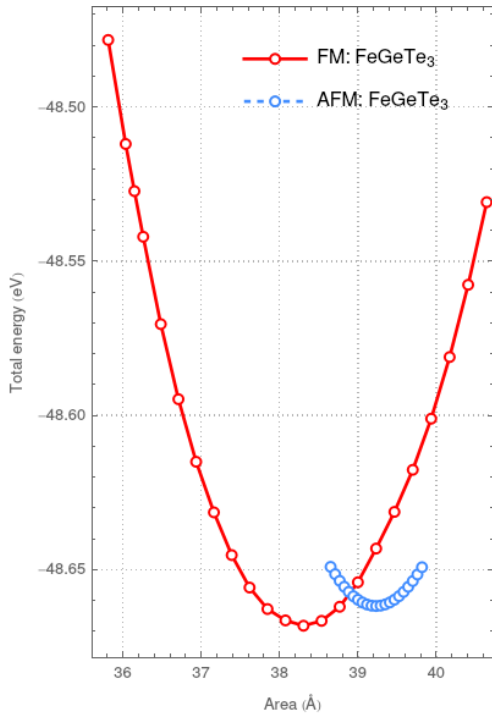
Properties	FM phase			AFM phase		
Space group	P-3 (162)			P-3 (162)		
$a = b$ (Å)	6.65			6.72		
c (Å)	21.82			21.82		
γ (°)	120			120		
Area (Å)	38.29			39.13		
Total Energy (eV)	-48.667			-48.664		
	Fe(1)	Fe(2)	Tot	Fe(1)	Fe(2)	Tot
μ_B	1.02	1.02	1.97	1.23	-1.23	0.00
	↑	↓	Tot	↑	↓	Tot
Band gap (eV)	0.00	0.00	0.00	0.00	0.00	0.00
Sites	u	v	w	u	v	w
Fe(1)	0.6666	0.3333	0.5000	0.6666	0.3333	0.5000
Fe(2)	0.3333	0.6666	0.5000	0.3333	0.6666	0.5000
Ge(1)	0.0000	0.0000	0.5559	0.0000	0.0000	0.5559
Ge(2)	0.0000	0.0000	0.4441	0.0000	0.0000	0.4440
Te(1)	0.0000	0.3941	0.4288	0.9999	0.3894	0.4301
Te(2)	0.9999	0.6059	0.5712	0.0000	0.6106	0.5699
Te(3)	0.6059	0.6059	0.4288	0.6106	0.6106	0.4301
Te(4)	0.3941	0.3941	0.5712	0.3894	0.3894	0.5699
Te(5)	0.3941	0.9999	0.4288	0.3894	0.0000	0.4301
Te(6)	0.6059	0.0000	0.5712	0.6106	0.9999	0.5699

Figure 4.19: Calculated electronic and magnetic properties for FM and AFM phases of FeGeTe₃ ML using the PBESol functional. Both magnetic phases exhibit metallic behavior.

4.3.3 Magnetic and electronic properties using PBE and PBESol functional with Hubbard U corrections

In this section, we analyze the magnetic and electronic properties of the FeGeTe₃ monolayer by applying Hubbard U corrections to the PBE and PBESol functionals. The initial results from the PBE functional suggested the stability of the antiferromagnetic (AFM) phase, prompting a detailed examination of this phase with Hubbard U corrections.

Magnetic Phase		Ferromagnetic						
Properties	$a = b$ (Å)	Total E (eV)	μ_B			Band Gap (eV)		
			Fe(1)	Fe(2)	Tot	↑	↓	Tot
U = 0.0	6.82	-44.483	1.19	1.19	2.10	0.39	0.13	0.13
U = 0.5	6.83	-43.629	1.26	1.26	2.15	0.36	0.46	0.31
U = 1.0	6.83	-42.806	1.33	1.33	2.22	0.33	0.76	0.33
U = 1.5	6.83	-42.013	1.44	1.44	2.31	0.27	0.83	0.27
U = 2.0	6.84	-41.256	1.57	1.57	2.42	0.20	0.84	0.20
U = 2.5	6.85	-40.542	1.73	1.73	2.55	0.11	0.85	0.11
U = 3.0	6.86	-39.878	1.90	1.90	2.70	0.00	0.86	0.00
U = 3.5	6.96	-39.826	3.71	3.71	8.52	0.00	0.00	0.00
U = 4.0	6.97	-39.441	3.73	3.73	8.60	0.00	0.00	0.00

Magnetic Phase		Antiferromagnetic						
Properties	$a = b$ (Å)	Total E (eV)	μ_B			Band Gap (eV)		
			Fe(1)	Fe(2)	Tot	↑	↓	Tot
U = 0.0	6.84	-44.526	1.34	-1.34	0.00	0.27	0.27	0.27
U = 0.5	6.84	-43.674	1.42	-1.42	0.00	0.42	0.42	0.42
U = 1.0	6.85	-42.853	1.52	-1.52	0.00	0.49	0.49	0.49
U = 1.5	6.91	-41.878	3.08	-3.08	0.00	0.00	0.00	0.00
U = 2.0	6.99	-41.263	3.54	-3.54	0.00	0.15	0.15	0.15
U = 2.5	6.99	-40.784	3.62	-3.62	0.00	0.31	0.31	0.31
U = 3.0	6.99	-40.347	3.67	-3.67	0.00	0.42	0.42	0.42
U = 3.5	6.99	-39.937	3.69	-3.69	0.00	0.49	0.49	0.49
U = 4.0	6.99	-39.545	3.71	-3.71	0.00	0.51	0.51	0.51

Table 4.5: Calculated electronic and magnetic properties for ferromagnetic (FM) and antiferromagnetic (AFM) phases of FeGeTe$_3$ ML using the PBE functional.

Magnetic Phase		Ferromagnetic						
Properties	$a = b$ (Å)	Total E (eV)	μ_B			Band Gap (eV)		
			Fe(1)	Fe(2)	Tot	↑	↓	Tot
U = 0.0	6.65	-48.702	1.00	1.00	1.95	0.00	0.00	0.00
U = 0.5	6.71	-47.783	1.18	1.18	2.09	0.33	0.14	0.14
U = 1.0	6.72	-46.929	1.24	1.24	2.14	0.31	0.42	0.31
U = 1.5	6.72	-46.102	1.32	1.32	2.21	0.27	0.69	0.27
U = 2.0	6.72	-45.302	1.40	1.40	2.28	0.23	0.78	0.23
U = 2.5	6.73	-44.533	1.52	1.52	2.36	0.17	0.81	0.17
U = 3.0	6.74	-43.779	1.63	1.63	2.45	0.12	0.84	0.12
U = 3.5	6.74	-43.031	1.78	1.78	2.58	0.07	0.88	0.07
U = 4.0	6.74	-42.276	1.84	1.84	2.64	0.03	0.93	0.03

Magnetic Phase		Antiferromagnetic						
Properties	$a = b$ (Å)	Total E (eV)	μ_B			Band Gap (eV)		
			Fe(1)	Fe(2)	Tot	↑	↓	Tot
U = 0.0	6.67	-48.303	1.00	-1.00	0.00	0.00	0.00	0.00
U = 0.5	6.67	-47.386	1.00	-1.00	0.00	0.13	0.13	0.13
U = 1.0	6.67	-46.542	1.00	-1.00	0.00	0.28	0.28	0.28
U = 1.5	6.67	-45.733	1.00	-1.00	0.00	0.37	0.37	0.37
U = 2.0	6.68	-44.938	3.21	-3.21	0.00	0.47	0.47	0.47
U = 2.5	6.68	-44.294	3.20	-3.20	0.00	0.59	0.59	0.59
U = 3.0	6.68	-43.543	3.19	-3.19	0.00	0.61	0.61	0.61
U = 3.5	6.68	-42.943	3.23	-3.23	0.00	0.65	0.65	0.65
U = 4.0	6.68	-42.557	3.25	-3.25	0.00	0.67	0.67	0.67

Table 4.6: Calculated electronic and magnetic properties for ferromagnetic (FM) and antiferromagnetic (AFM) phases of $FeGeTe_3$ ML using the PBESol functional.

The results are summarized in the following figures:
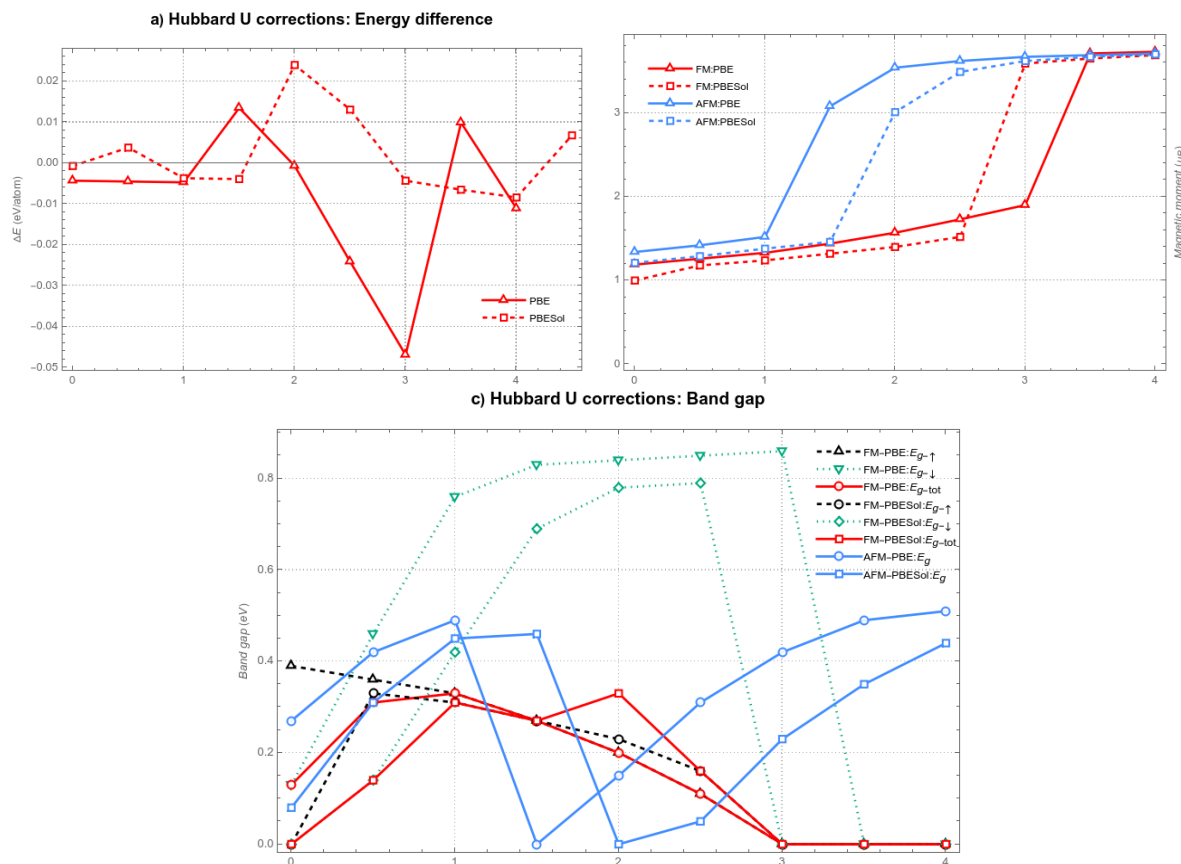
Figure 4.20: **(a)** Difference in total energy as a function of Hubbard U for both ferromagnetic and antiferromagnetic phases. The antiferromagnetic phase exhibits enhanced stability at specific U values, with $U = 3.0$ identified as the most favorable. **(b)** Dependence of magnetic moment on Hubbard U. **(c)** Variation of the band gap with Hubbard U. The PBE+U(1.0) functional yields a suitable band gap for the antiferromagnetic phase, aligning with the desired semiconductor behavior, although it does not fully replicate the HSE06 results.

To achieve semiconductor behavior in the antiferromagnetic phase, we recommend the PBE+U(1.0) functional (see Fig. 4.21). This functional maintains the stability of the antiferromagnetic phase and provides a magnetic moment of approximately 1.46 μ_B, which closely resembles the results obtained with the HSE06 functional. However, attaining a band gap comparable to that from HSE06 remains challenging with Hubbard U corrections, primarily due to the relationship between the magnetic moment and Hubbard U, as illustrated in the final figure.
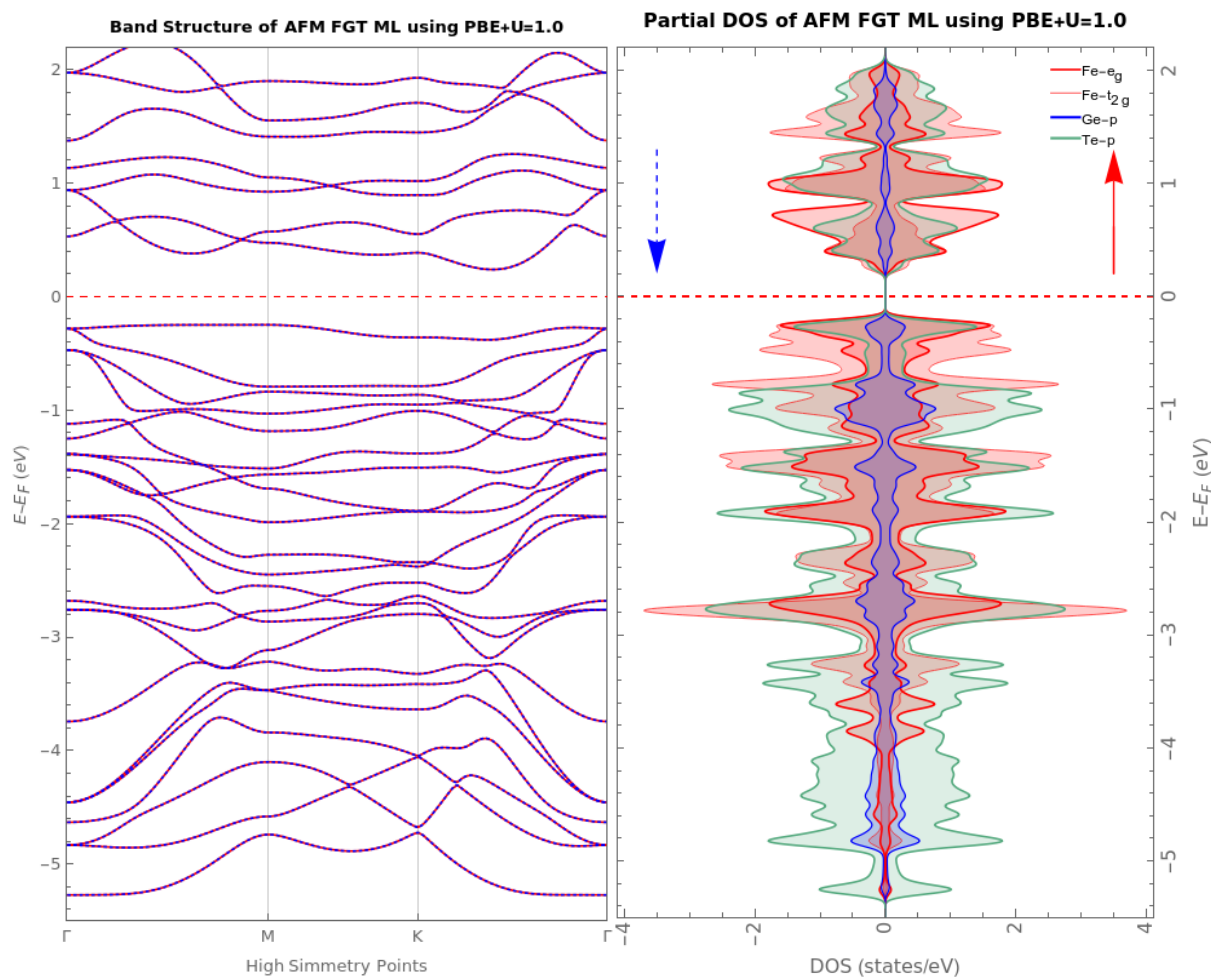
Figure 4.21: Band structure (left) and density of states (DOS) plot (right) for the antiferromagnetic FeGeTe$_3$ monolayer using the PBE functional. Notably, hybridization occurs between the 'd' orbitals of Fe and the 'p' orbitals of Te, with stronger interactions observed for the e_g states compared to the t_{2g} states.

4.3.4 Phonon Band Structure

To evaluate the thermodynamic stability of the antiferromagnetic (AFM) phase using the PBE+U(1.0) functional, we performed phonon calculations on a 4x4x1 supercell. Despite the application of Hubbard U corrections, the phonon band structure analysis reveals the presence of negative frequencies, indicating potential instability in the AFM phase.
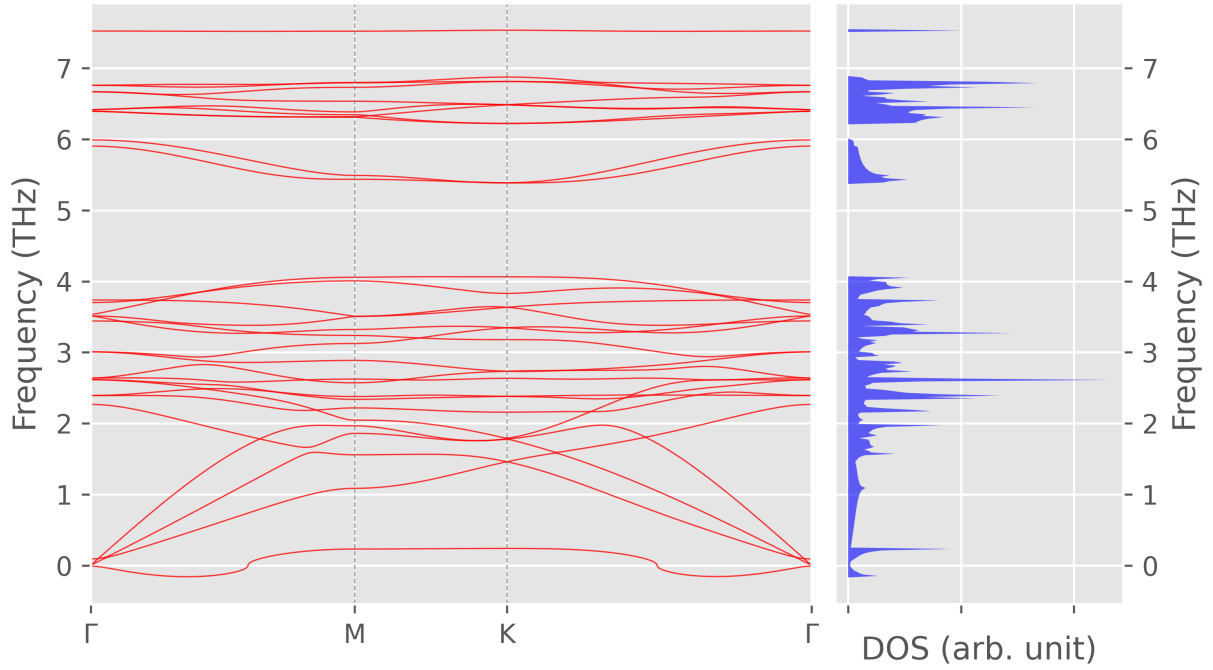
Figure 4.22: Phonon band structure (left) and phonon density of states (DOS) plot (right) for the AFM phase of the FGT 4x4x1 supercell.

4.4 Random Alloys

In this section, we present our results for random alloys obtained using the Special Quasirandom Structure (SQS) method for the sublattice systems X = Cr-Mn, Cr-Fe, and Fe-Mn within a 4x3x1 supercell of $X\text{GeTe}_3$, which consists of 24 formula units (f.u.) and a total of 120 atoms. This composition includes 24 atoms of the sublattice X, which varies based on the partial occupations ($x = 0.25$, 0.50, and 0.75), 24 atoms of Ge, and 72 atoms of Te. It is important to note that the SQS obtained represents random configurations fitting the lattice sites of $\text{Cr}_x\text{Mn}_{1-x}\text{GeTe}_3$.

We employed several relaxation loops—rather than performing a full relaxation—to achieve optimized random alloys. The relaxation process was structured as follows: (1) relax the cell size (area), (2) relax the cell size again, (3) relax ionic positions, (4) relax the cell size once more, and (5) relax ionic positions again.

4.4.1 $\text{Cr}_{1-x}\text{GeMn}_x\text{Te}_3$ Random Alloys

We begin with the random alloys $\text{Cr}_{1-x}\text{GeMn}_x\text{Te}_3$ at concentrations $x = 0.25$, 0.50, and 0.75. Some important properties, such as the magnetic moment and total energy, are presented in Table 4.7. Notably, at the concentration $x = 0.50$, throughout the entire relaxation loop (except in the third step), we observed an unusual error (standard deviation) in the mean magnetic

moment of the Mn atoms. Specifically, one of the 12 Mn atoms (Mn atom number 10) exhibited a negative magnetic moment throughout the relaxation process (except in the third step), with values ranging from -3.707 to -3.610 μ_B. Conversely, if we disregard this Mn atom with a negative magnetic moment, the average magnetic moment across the entire relaxation process ranges from 3.552 to 3.568 μ_B, with a small standard deviation ranging from $\pm$ 0.008 to $\pm$ 0.017 μ_B.

This behavior can be attributed to the local atomic environment of the Te atoms surrounding each Mn atom. For the 11 Mn atoms, the average distance to the surrounding Te atoms is approximately 2.78 to 2.79 Å, while the distance for Mn atom number 10 is 2.81 Å. This discrepancy may lead to magnetic frustration—competing magnetic interactions between the Cr and Mn atoms—in the random alloy at the concentration of $x = 0.50$. Consequently, it is energetically favorable for the Mn atom to align antiferromagnetically with its neighbors.

Concentration x%	Property	Atom	Relaxation				
			Step 1	Step 2	Step 3	Step 4	Step 5
25	Magnetic Moment (μ_B/atom)	Cr	3.122 ± 0.009	3.122 ± 0.009	3.101 ± 0.012	3.091 ± 0.012	3.095 ± 0.012
		Ge	0.022 ± 0.007	0.022 ± 0.007	0.023 ± 0.007	0.022 ± 0.007	0.023 ± 0.007
		Mn	3.539 ± 0.004	3.539 ± 0.004	3.586 ± 0.010	3.570 ± 0.017	3.571 ± 0.016
		Te	-0.073 ± 0.011	-0.073 ± 0.011	-0.072 ± 0.011	-0.071 ± 0.011	-0.072 ± 0.011
		Total	77.677	77.677	77.637	77.618	77.688
	Total Energy (eV)		-566.222	-566.222	-566.187	-566.226	-566.234
50	Magnetic Moment (μ_B/atom)	Cr	3.131 ± 0.012	3.131 ± 0.012	3.113 ± 0.017	3.105 ± 0.016	3.107 ± 0.016
		Ge	0.028 ± 0.009	0.028 ± 0.009	0.030 ± 0.008	0.027 ± 0.008	0.026 ± 0.008
		Mn	2.940 ± 2.060	2.940 ± 2.060	3.568 ± 0.017	2.954 ± 2.079	2.947 ± 2.096
		Te	-0.078 ± 0.024	-0.078 ± 0.024	-0.082 ± 0.011	-0.077 ± 0.023	-0.077 ± 0.023
		Total	67.947	67.947	74.961	67.824	67.672
	Total Energy (eV)		-570.772	-570.773	-570.691	-570.741	-570.756
75	Magnetic Moment (μ_B/atom)	Cr	3.141 ± 0.012	3.141 ± 0.012	3.130 ± 0.014	3.122 ± 0.014	3.126 ± 0.014
		Ge	0.037 ± 0.008	0.037 ± 0.008	0.034 ± 0.008	0.034 ± 0.008	0.034 ± 0.008
		Mn	3.529 ± 0.007	3.529 ± 0.007	3.525 ± 0.007	3.511 ± 0.007	3.510 ± 0.007
		Te	-0.081 ± 0.008	-0.081 ± 0.008	-0.078 ± 0.009	-0.078 ± 0.009	-0.078 ± 0.009
		Total	64.209	64.209	64.208	64.196	64.200
	Total Energy (eV)		-570.771	-570.771	-570.771	-570.770	-570.770

Table 4.7: Magnetic moments and total energies at different stages of the relaxation cycle for each concentration $x = 0.25$, 0.50, and 0.75. An issue with the average magnetic moment of Mn atoms at the concentration of $x = 0.50$ is noted, as its standard deviation is considerable.

Using the values obtained from the final relaxation loop, corresponding to the most stable configuration, we computed key thermodynamic properties such as the formation and mixing energies. For the formation energy, we considered the 24 formula units (f.u.) that make up the random alloy $Cr_{1-x}GeMn_xTe_3$:

$$\Delta_f(\text{Cr}_{1-x}\text{GeMn}_x\text{Te}_3) = E(\text{Cr}_{24(1-x)}\text{Ge}_{24}\text{Mn}_{24x}\text{Te}_{72})$$
$$- [24(1-x)E(\text{Cr}) + 24E(\text{Ge}) + 24xE(\text{Mn}) + 72E(\text{Te})]$$

Here, $E(\text{Cr}_{24(1-x)}\text{Ge}_{24}\text{Mn}_{24x}\text{Te}_{72})$ represents the total energy of the alloy obtained from the final relaxation loop, as summarized in Table 4.7. The terms $E(\text{Cr})$, $E(\text{Ge})$, $E(\text{Mn})$, and $E(\text{Te})$ correspond to the chemical potentials of the individual elements. These chemical potentials are calculated by performing full structural relaxations on the pure elemental unit cells and dividing the total energy of each unit cell by the number of atoms it contains. These values serve as reference energies for the elements in their most stable crystalline forms, which are critical for calculating the formation energy of the alloy.

For the mixing energy, which also considers the 24 formula units, accounting for the energetic cost or benefit of forming the alloy from its individual components, we use the following expression:

$$\Delta E_{\text{mix}}(\text{Cr}_{1-x}\text{GeMn}_x\text{Te}_3) = E(\text{Cr}_{24(1-x)}\text{Ge}_{24}\text{Mn}_{24x}\text{Te}_{72})$$
$$- [24(1-x)E(\text{CrGeTe}_3) + 24xE(\text{MnGeTe}_3)]$$

Here, $E(\text{CrGeTe}_3)$ and $E(\text{MnGeTe}_3)$ denote the total energies of the unmixed monolayers containing chromium and manganese, respectively. These total energies are precomputed using the Perdew–Burke–Ernzerhof (PBE) functional, as illustrated in Figures 4.3 and 4.10. Both the formation and mixing energies are derived from the total energies obtained after the final relaxation step, ensuring that the most stable configuration of the alloy is used for all subsequent calculations.
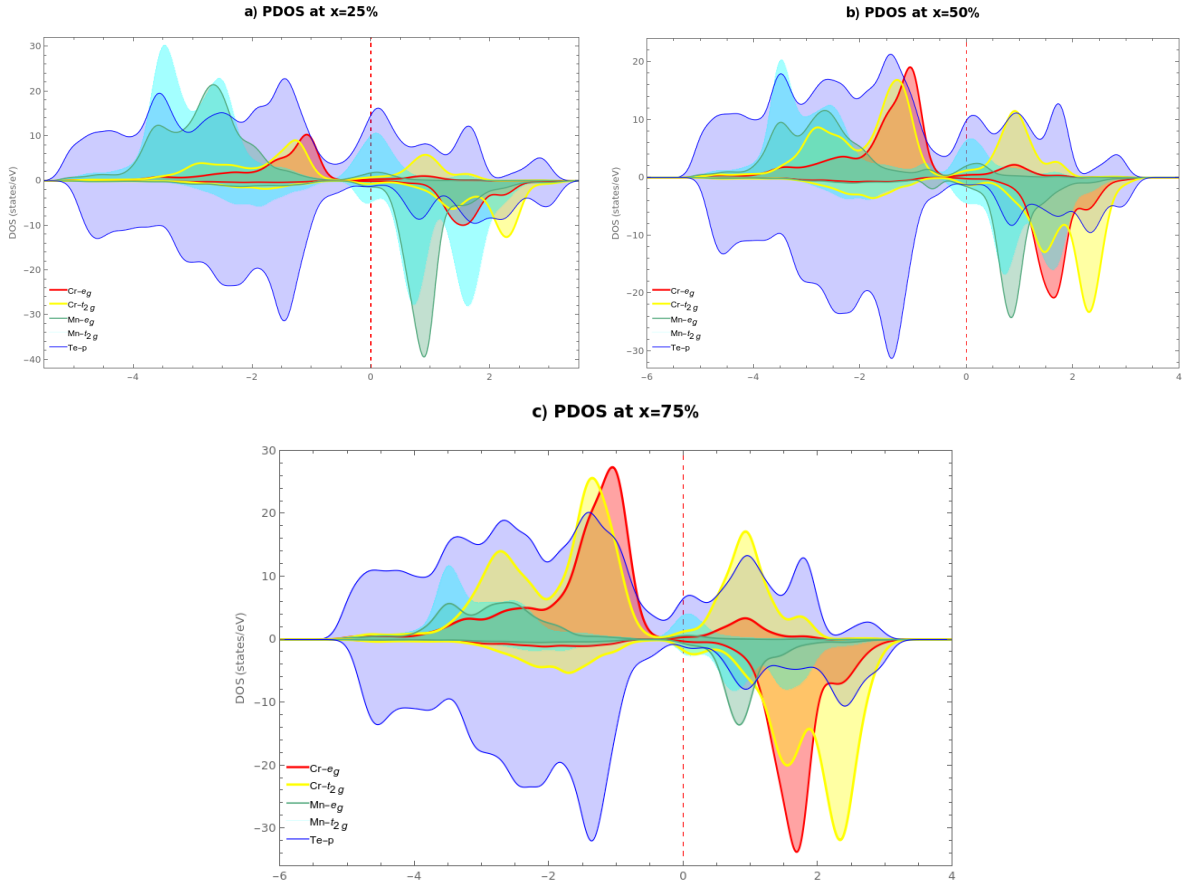
Figure 4.23: Projected density of states of the random alloys, where the x-axis represents the energy (eV) range concerning the Fermi level (displayed as a red dashed line) for $Cr_xGeMn_{1-x}Te_3$ at (**a**) $x = 0.25$, (**b**) $x = 0.50$, and (**c**) $x = 0.75$. In (**a**) and (**b**), a strong hybridization of the d orbitals of the magnetic atoms with the p orbitals of Te is observed. In (**c**), a weak localization of the e_g states of Cr atoms is noted for the spin-down channel above the Fermi level.

The formation energies obtained for concentrations of $x = 0.25$, $x = 0.50$, and $x = 0.75$ are -0.503, -0.540, and -0.597 eV/f.u., respectively. A similar approach was employed to calculate the mixing energies, resulting in values of 0.037, 0.014, and 0.015 eV/f.u., respectively. These values indicate a global stability for the random alloys $Cr_xGeMn_{1-x}Te_3$ at the studied concentrations. However, the positive values of the mixing energies suggest a complex internal structure, implying that there may exist a different ground magnetic phase than the ferromagnetic one that we considered.

Finally, we present in Fig. 4.23 the projected density of states for these concentrations. Notably, for $x = 0.25$, the random alloy exhibits well-defined d states for Mn atoms; however, the d states for Cr atoms are significantly hybridized with the p orbitals of Te atoms. For the concentration $x = 0.50$, the d states are not well-localized for both Cr and Mn atoms, as they are hybridized with the p orbitals of Te. In contrast, for the concentration $x = 0.75$, the d orbitals of Cr atoms are well-localized, while the d states of Mn atoms remain localized but hybridized with the p states of Te atoms.

4.4.2 Cr$_{1-x}$GeFe$_x$Te$_3$ random alloys

In this section, we examine the random alloy of the form Cr$_{1-x}$GeFe$_x$Te$_3$. The magnetic moments and total energies for the different concentrations $x = 0.25, 0.50$, and 0.75 are presented in Tab. 4.8. The calculations show negligible errors, indicated by small standard deviations, across the five relaxation loops. Using the total energies from the final loop (the fifth loop), we can calculate the formation energies and mixing energies similarly to our previous analysis for the Cr$_{1-x}$GeMn$_x$Te$_3$ alloy.

Concentration $x\%$	Property	Atom	Relaxation				
			Step 1	Step 2	Step 3	Step 4	Step 5
		Cr	3.054 ± 0.01	3.054 ± 0.01	3.063 ± 0.011	3.061 ± 0.012	3.058 ± 0.01
	Magnetic	Ge	0.002 ± 0.007	0.002 ± 0.007	0.005 ± 0.006	0.005 ± 0.006	0.005 ± 0.006
25	moment ($\mu_B/atom$)	Fe	2.237 ± 0.029	2.239 ± 0.029	2.218 ± 0.051	1.238 ± 0.057	1.237 ± 0.06
		Te	-0.068 ± 0.011	-0.068 ± 0.011	-0.059 ± 0.013	-0.057 ± 0.013	-0.057 ± 0.013
		Total	53.741	53.743	36.971	36.966	36.675
	Total Energy (eV)		-538.728	-538.727	-543.151	-543.378	-543.396
		Cr	3.084 ± 0.018	3.084 ± 0.023	3.087 ± 0.02	3.084 ± 0.02	3.082 ± 0.02
	Magnetic	Ge	0.011 ± 0.009	0.011 ± 0.009	0.013 ± 0.008	0.012 ± 0.009	0.012 ± 0.009
50	moment ($\mu_B/atom$)	Fe	2.23 ± 0.061	2.231 ± 0.061	1.307 ± 0.071	1.328 ± 0.079	1.33 ± 0.08
		Te	-0.076 ± 0.016	-0.076 ± 0.016	-0.074 ± 0.015	-0.074 ± 0.015	-0.074 ± 0.015
		Total	58.194	58.209	47.577	47.902	47.906
	Total Energy (eV)		-552.521	-552.524	-555.368	-555.549	-555.554
		Cr	2.06 ± 1.491	2.06 ± 1.491	3.114 ± 0.019	3.111 ± 0.019	3.11 ± 0.019
	Magnetic	Ge	0.564 ± 0.98	0.564 ± 0.98	0.025 ± 0.011	0.025 ± 0.012	0.025 ± 0.012
75	moment ($\mu_B/atom$)	Fe	2.238 ± 0.077	2.237 ± 0.078	1.426 ± 0.063	1.455 ± 0.067	1.458 ± 0.068
		Te	-0.081 ± 0.011	-0.081 ± 0.011	-0.091 ± 0.008	-0.089 ± 0.011	-0.089 ± 0.011
		Total	58.209	58.209	58.711	58.922	58.926
	Total Energy (eV)		-566.454	-566.454	-567.718	-567.846	-567.847

Table 4.8: Average magnetic moments per atom and total energies of the random alloys Cr$_{1-x}$GeFe$_x$Te$_3$ at the concentrations $x = 0.25, 0.50$, and 0.75 for each stage of the implemented relaxation cycle. Note that the standard deviation values are minimal, ensuring realistic calculations.

For the concentrations $x = 0.25, 0.50$, and 0.75, we obtain formation energies of -0.163, -0.314, and -0.471 eV/f.u., respectively, along with mixing energies of 0.054, 0.042, and 0.025 eV/f.u. These negative formation energies indicate that the random alloy exhibits stable behavior at the studied concentrations. The positive mixing energies suggest that the $4 \times 3 \times 1$ supercell contains heterogeneous interaction domains among the constituent atoms, consistent with the characteristics of a truly random alloy.

We present the projected density of states for this random alloy in Fig. 4.24.
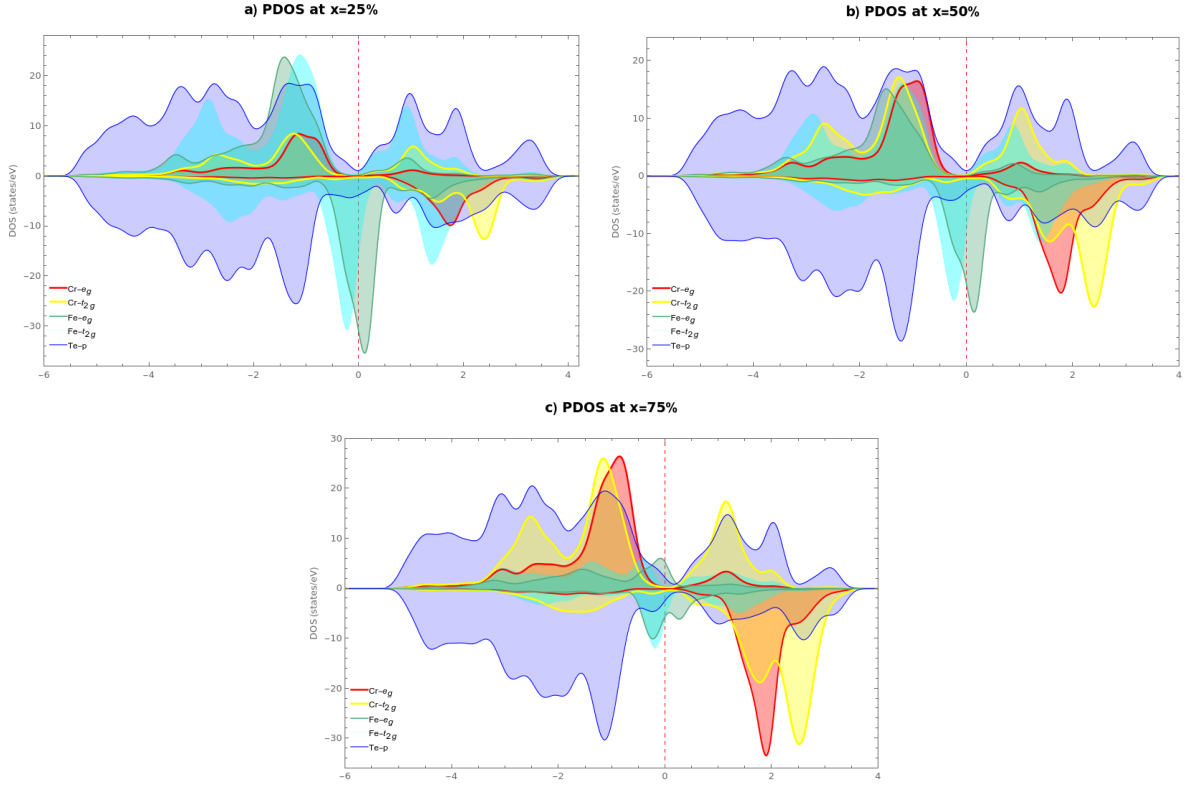
Figure 4.24: Projected density of states for the $Cr_{1-x}GeFe_xTe_3$ random alloys at concentrations (a) $x = 0.25$, (b) $x = 0.50$, and (c) $x = 0.75$.

As illustrated in Fig. 4.24 **(a)**, at a concentration of $x = 0.25$, well-behaved localized d states are observed around the Fermi level for Fe atoms in the spin-down channel, while conduction and valence bands in the spin-up channel are less localized. Additionally, the d states of Cr atoms are hybridized with the p states of Te in both spin channels.

For the concentration of $x = 0.50$ shown in Fig. 4.24 **(b)**, we again observe localized d states for Fe atoms around the Fermi level. However, the d states of Cr are not localized within the valence or conduction bands, as both are hybridized with the p states of Te.

Conversely, for the concentration of $x = 0.75$ presented in Fig. 4.24 **(c)**, the d states of Fe atoms contribute minimally to the density of states of the alloy. In contrast, the d states of Cr are better defined, particularly with respect to the e_g orbitals, which exhibit more localization compared to the t_{2g} orbitals. It is also noteworthy that there exists a strong hybridization, similar to the other concentrations, between the d states of Cr and Fe and the p states of Te.

4.4.3 $Fe_{1-x}GeMn_xTe_3$ random alloys

Finally, we present the results for the random alloy incorporating Fe and Mn atoms. Table 4.9 displays the mean magnetic moments of the atoms involved in the random alloy $Fe_{1-x}GeMn_xTe_3$ and their corresponding total energy for each concentration. Generally, no significant errors are associated with these results. We found formation energies of -0.384, -0.304, and -0.169 eV/f.u. for concentrations of x = 0.25, 0.50, and 0.75, respectively. The mixing energies for the same concentrations are -0.011, -0.030, and 0.006 eV/f.u., indicating that these alloys are thermodynamically stable. However, at x = 0.75, we observe an inhomogeneous alloy, as its positive mixing energy leads to structural tensions within the alloy.

Concentration $x\%$	Property	Atom	Relaxation				
			Step 1	Step 2	Step 3	Step 4	Step 5
25	Magnetic moment ($\mu_B/atom$)	Fe	-0.038 ± 2.875	-0.415 ± 1.074	-0.938 ± 0.077	-0.795 ± 0.472	-0.625 ± 0.884
		Ge	0.017 ± 0.004	0.016 ± 0.003	0.015 ± 0.004	0.015 ± 0.004	0.015 ± 0.004
		Mn	3.539 ± 0.016	3.496 ± 0.013	3.443 ± 0.066	3.444 ± 0.067	3.458 ± 0.066
		Te	-0.050 ± 0.017	-0.050 ± 0.017	-0.045 ± 0.025	-0.046 ± 0.024	-0.046 ± 0.024
		Total	60.266	57.230	53.479	54.257	55.494
	Total Energy (eV)		-553.072	-552.183	-554.872	-554.850	-554.864
50	Magnetic moment ($\mu_B/atom$)	Fe	2.427 ± 0.018	2.427 ± 0.018	0.828 ± 0.864	0.797 ± 0.583	0.879 ± 0.883
		Ge	0.008 ± 0.004	0.008 ± 0.004	0.012 ± 0.003	0.011 ± 0.003	0.011 ± 0.003
		Mn	3.509 ± 0.019	3.510 ± 0.019	3.457 ± 0.090	3.438 ± 0.091	3.430 ± 0.088
		Te	-0.056 ± 0.006	-0.056 ± 0.006	-0.052 ± 0.013	-0.052 ± 0.013	-0.052 ± 0.013
		Total	67.366	67.375	47.952	47.361	48.173
	Total Energy (eV)		-544.153	-544.156	-547.343	-547.373	-548.038
75	Magnetic moment ($\mu_B/atom$)	Fe	2.306 ± 0.011	2.308 ± 0.011	1.042 ± 0.180	1.033 ± 0.180	1.035 ± 0.179
		Ge	0.008 ± 0.003	0.008 ± 0.003	0.018 ± 0.003	0.025 ± 0.012	0.025 ± 0.012
		Mn	3.447 ± 0.015	3.448 ± 0.015	3.297 ± 0.031	3.288 ± 0.031	3.288 ± 0.031
		Te	-0.057 ± 0.005	-0.057 ± 0.005	-0.049 ± 0.013	-0.049 ± 0.013	-0.049 ± 0.013
		Total	58.096	58.095	35.116	34.924	34.965
	Total Energy (eV)		-535.253	-535.254	-539.912	-539.914	-539.909

Table 4.9: Average magnetic moments per atom and total energies of the random alloys $Fe_{1-x}GeMn_xTe_3$ at the concentrations $x = 0.25$, 0.50, and 0.75 during each stage of the implemented relaxation cycle. Note that the standard deviation values are minimal, ensuring realistic calculations.

As with the other random alloys, we present the projected density of states (PDOS) for the different concentrations considered, as shown in Fig. 4.25.
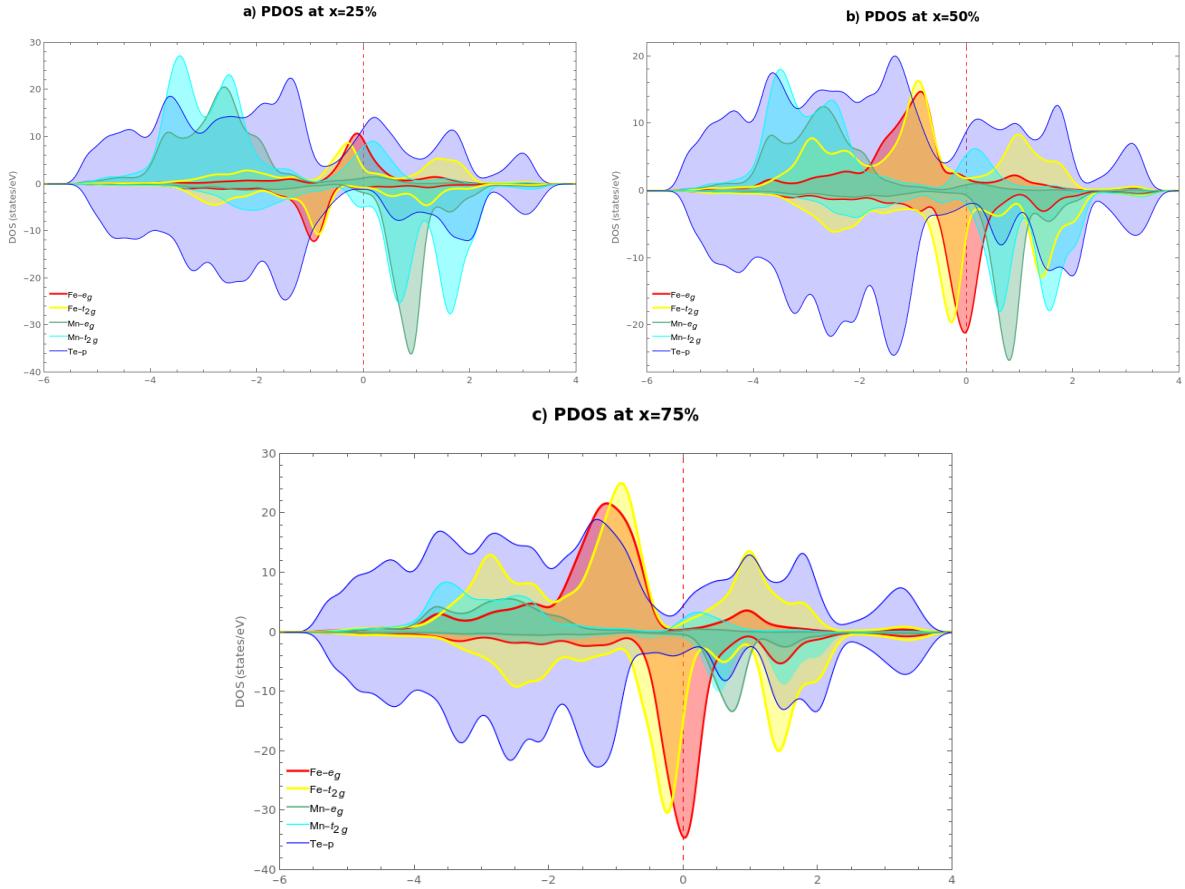
Figure 4.25: Projected density of states of the random alloys $Fe_{1-x}GeMn_xTe_3$ for **(a)** at $x = 0.25$, for **(b)** at $x = 0.50$, and for **(c)** at $x = 0.75$. In all cases, a strong hybridization of the d orbitals of magnetic atoms with the p orbitals of Te is observed.

As shown in Fig. 4.25, the concentration of Fe atoms increases the presence of d orbitals in the projected density of states.

In Fig. 4.25**(a)**, we observe bound states for the t_{2g} orbitals in the range of -4 to -2 eV for the spin-up channel, while bound states for the same orbitals are present in the range of 0 to 2 eV for the spin-down channel. The e_g orbitals appear to be more accurately described, as they are slightly more localized, particularly for the conduction band located around 0.95 eV above the Fermi level. In contrast, the contribution of Fe to the PDOS is weaker, and the e_g orbitals are better localized compared to their t_{2g} counterparts. The d states of both Fe and Mn atoms exhibit strong hybridization with the p states of Te.

In Fig. 4.25**(b)**, the t_{2g} orbitals of Fe appear delocalized, while the localized e_g orbitals of the same species are better described. Additionally, bound states for the d states of Mn in the spin-up channel are observed in the valence bands around -4 to -2 eV, with similar states present in the conduction bands from 0 to 2 eV.

Finally, in Fig. 4.25**(c)**, the delocalized t_{2g} orbitals are more pronounced compared to the concentration $x = 0.50$. Similarly, the e_g orbitals for Fe are better localized than in the previous two concentrations. Furthermore, it is evident that the d orbitals of Mn are completely hybridized with the p states of Te.

Chapter 5

Conclusions & Outlook

This work provides a comprehensive analysis of the magnetic and electronic properties of XGeTe$_3$ (X = Cr, Mn, Fe) monolayers and their random alloys, including Cr$_{1-x}$GeMn$_x$Te$_3$, Cr$_{1-x}$GeFe$_x$Te$_3$, and Fe$_{1-x}$GeMn$_x$Te$_3$, using density functional theory (DFT) with PBE and PBESol functionals, alongside Hubbard U corrections.

For the CrGeTe$_3$ monolayer, we confirmed robust ferromagnetic (FM) ordering, driven by strong exchange interactions. The PBE+U functional, with $U = 3.0$ eV, offered a balanced trade-off between computational efficiency and accuracy. The calculated band gap aligned well with experimental data. Phonon stability analysis confirmed the dynamical stability of the system, supporting its potential for practical applications. Future studies may benefit from using more advanced functionals for deeper exploration of its electronic and magnetic properties.

The MnGeTe$_3$ monolayer exhibited half-metallic (HM) behavior, making it suitable for spintronic applications. The PBE+U functional, with $U = 2.5$ eV, effectively captured both the magnetic moments and ground state energies. Phonon analysis confirmed its dynamical stability, positioning MnGeTe$_3$ as a promising material for further refinement of the Hubbard U parameter or exploration of alternative functionals.

The FeGeTe$_3$ monolayer displayed distinct deviations from the symmetrical behavior observed in CrGeTe$_3$ and MnGeTe$_3$. These deviations were attributed to its antiferromagnetic (AFM) ground state and the hybridization between Fe d states and Te p states. Phonon analysis revealed negative frequencies, suggesting potential dynamical instabilities that need to be addressed to fully understand and optimize the electronic properties of FeGeTe$_3$.

For the random alloys, substitution of Cr, Mn, and Fe atoms in XGeTe$_3$ supercells led to notable changes in magnetic moments, electronic structures, and alloy stability. In Cr$_{1-x}$GeMn$_x$Te$_3$ at $x = 0.50$, magnetic moment disorder was observed, where one Mn atom exhibited a negative magnetic moment due to local atomic environments and magnetic frustration linked to variations

in Mn-Te bond lengths. This suggests the presence of complex magnetic ground states, which could be beneficial for spintronic applications. Negative formation energies across different concentrations confirmed the alloy's global thermodynamic stability, while positive mixing energies indicated structural complexity that could give rise to non-ferromagnetic phases.

In $Cr_{1-x}GeFe_xTe_3$, at $x = 0.75$, strong hybridization between Fe and Cr d states and Te p states was observed, indicating the tunability of electronic transport properties through Fe doping. This positions the alloy as a promising candidate for applications in magnetic sensors and thermoelectric devices. The consistent magnetic moments and stable formation energies across concentrations further affirm its technological viability.

In the $Fe_{1-x}GeMn_xTe_3$ system, increasing Mn concentrations (up to $x = 0.75$) led to structural tension and strong hybridization between Mn and Fe d states with Te. This suggests the alloy's potential for applications in magnetic tunneling junctions and other devices requiring tailored electronic and magnetic properties. However, despite the negative formation energies confirming thermodynamic stability, the structural tensions at high Mn concentrations must be addressed to fully harness the alloy's technological potential.

In conclusion, this investigation underscores the significant technological potential of $XGeTe_3$ monolayers and their random alloys for applications in spintronics, magnetic memory, and thermoelectric devices. Precise control over magnetic frustration, hybridization, and alloy stability is essential for the successful deployment of these materials, paving the way for future research in this rapidly advancing field.

Appendix A
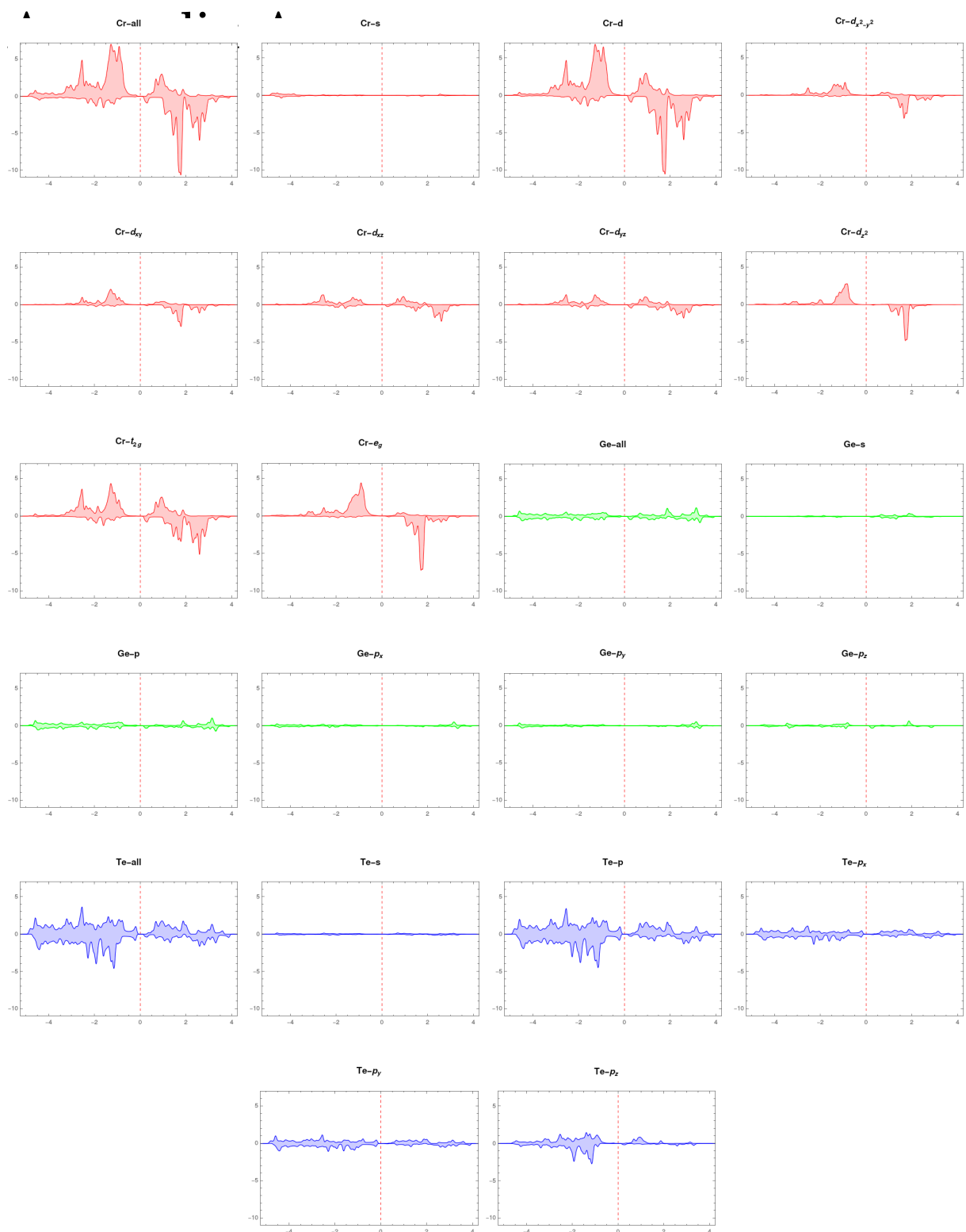
Figure A.1: Detailed density of states for the ferromagnetic CrGeTe monolayer calculated using the

Figure A.2: Detailed density of states for the ferromagnetic CrGeTe$_3$ monolayer, calculated using the PBESol functional for each atomic orbital, is shown. The horizontal axis represents the energy difference $E - E_F$, while the vertical axis indicates the normalized density of states (states/eV)

Figure A.3: Detailed density of states for the ferromagnetic CrGeTe$_3$ monolayer, calculated using the hybrid functional HSE06 for each atomic orbital, is shown. The horizontal axis represents the energy difference $E - E_F$, while the vertical axis indicates the normalized density of states (states/eV)

Figure A.4: Detailed density of states for the ferromagnetic MnGeTe$_3$ monolayer, calculated using the PBE functional for each atomic orbital, is shown. The horizontal axis represents the energy difference $E - E_F$, while the vertical axis indicates the normalized density of states (states/eV)
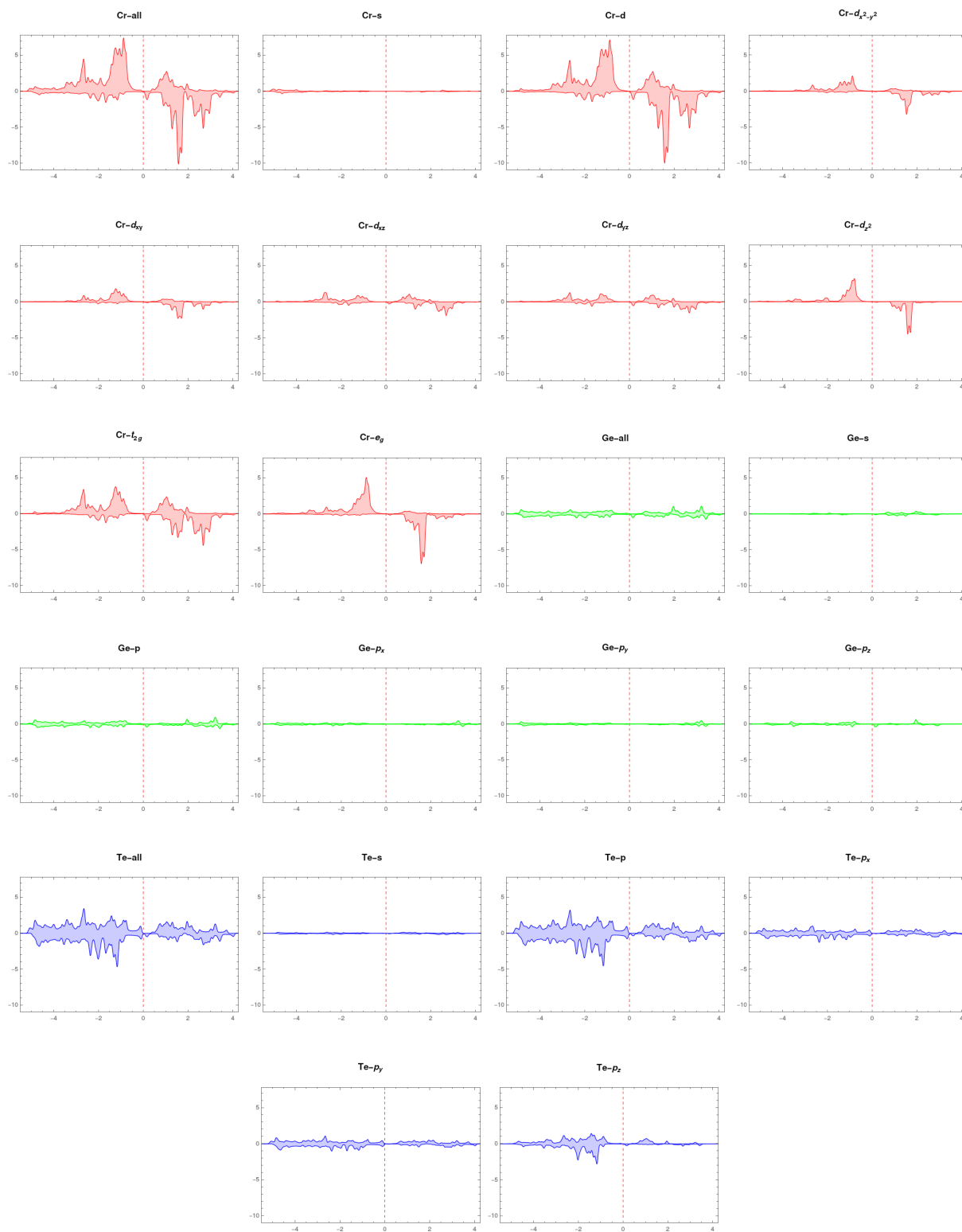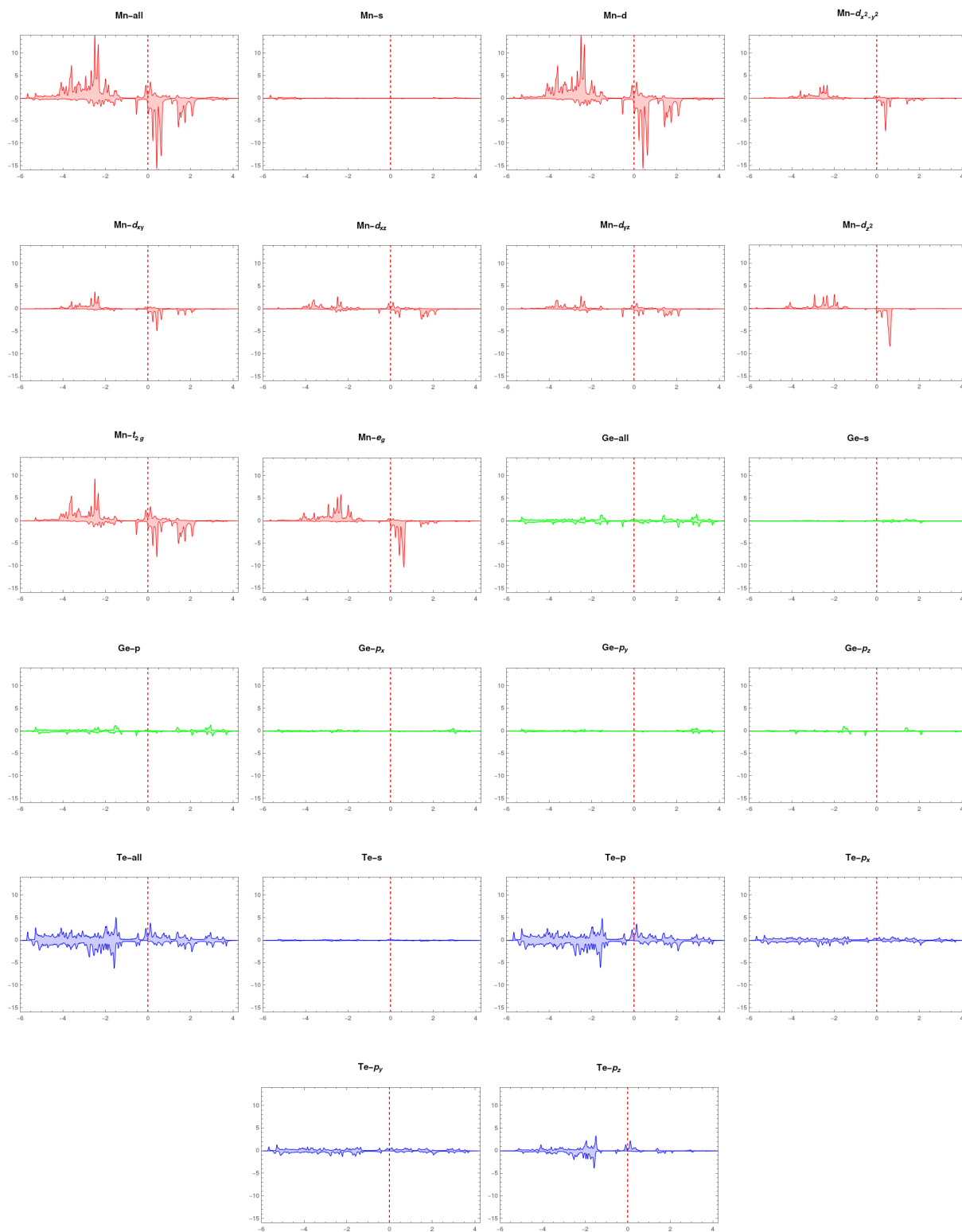
Figure A.5: Detailed density of states for the ferromagnetic MnGeTe₃ monolayer, calculated using the PBESol functional for each atomic orbital, is shown. The horizontal axis represents the energy difference $E - E_F$, while the vertical axis indicates the normalized density of states (states/eV)
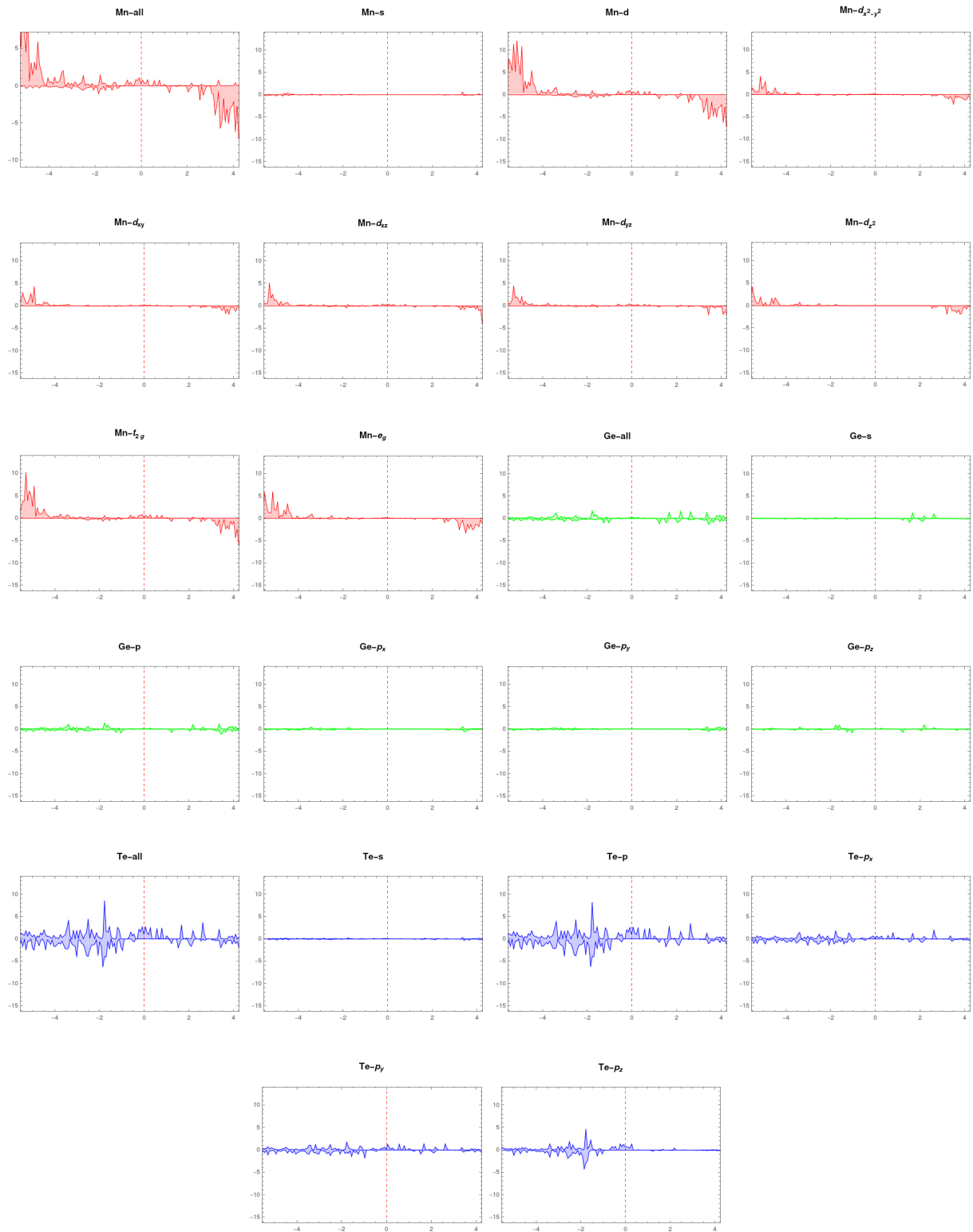
Figure A.6: Detailed density of states for the ferromagnetic MnGeTe$_3$ monolayer, calculated using the hybrid functional HSE06 for each atomic orbital, is shown. The horizontal axis represents the energy difference $E - E_F$, while the vertical axis indicates the normalized density of states (states/eV)
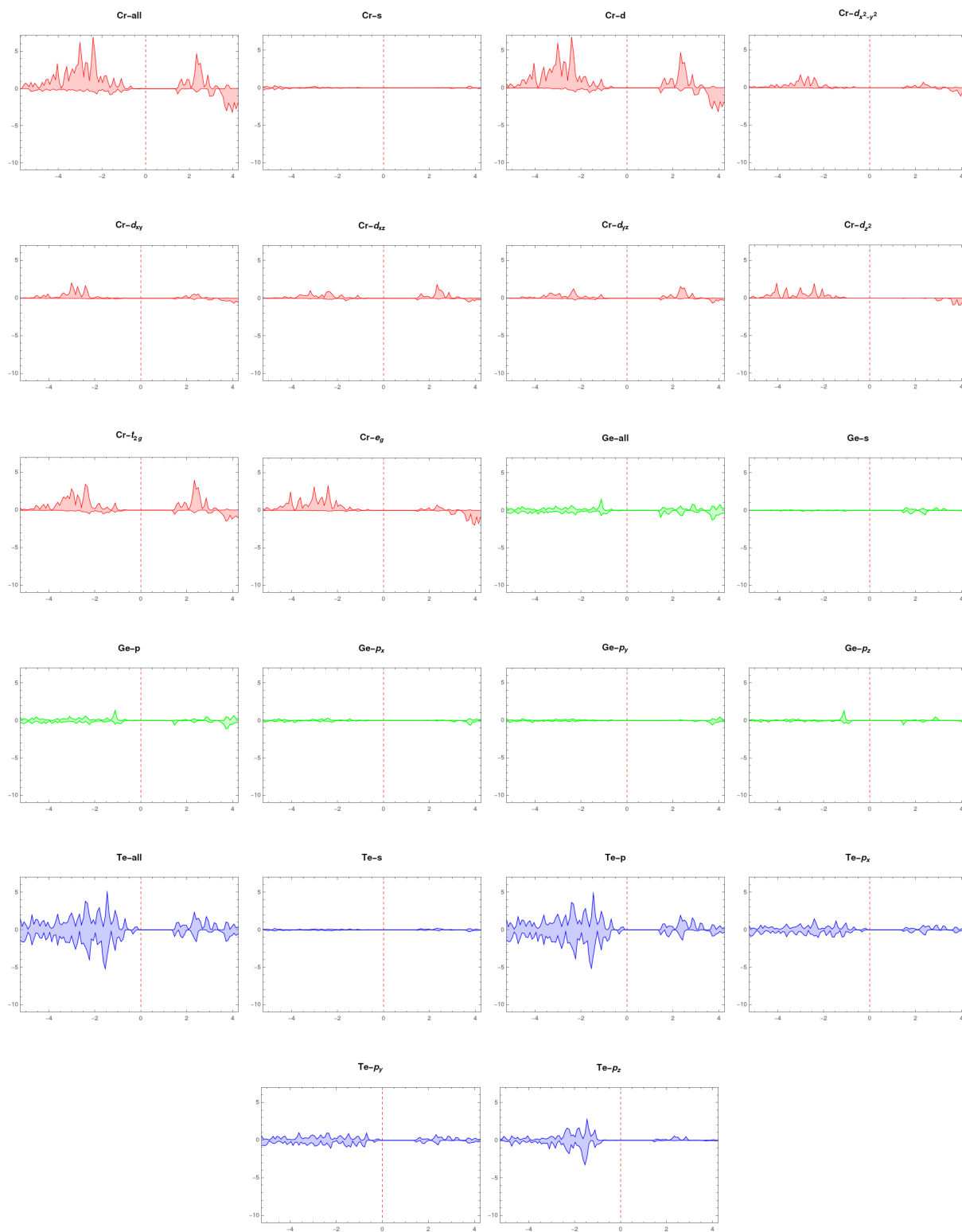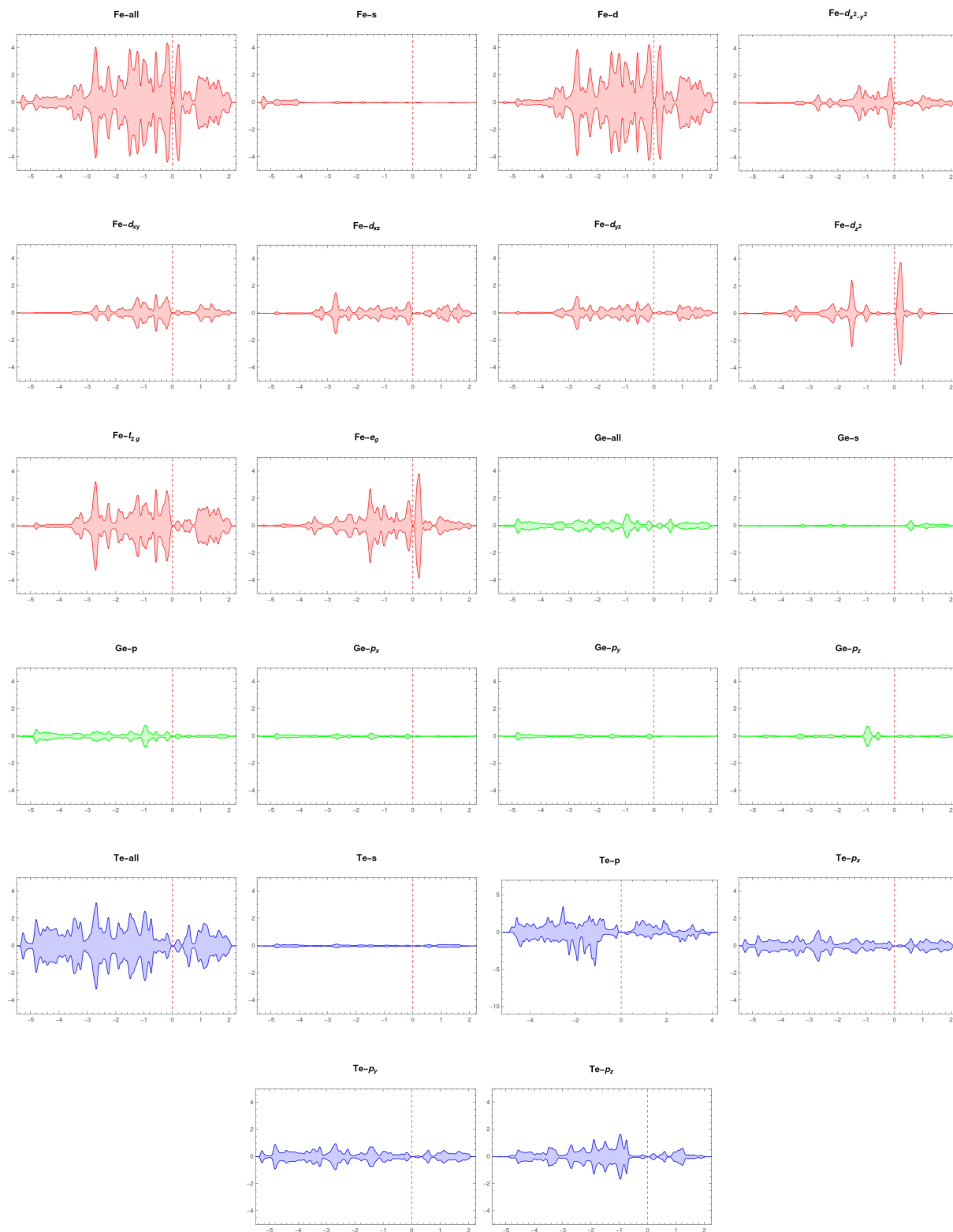
Figure A.7: Detailed density of states for the anti-ferromagnetic FeGeTe$_3$ monolayer, calculated using the PBE functional for each atomic orbital, is shown. The horizontal axis represents the energy difference $E - E_F$, while the vertical axis indicates the normalized density of states (states/eV)
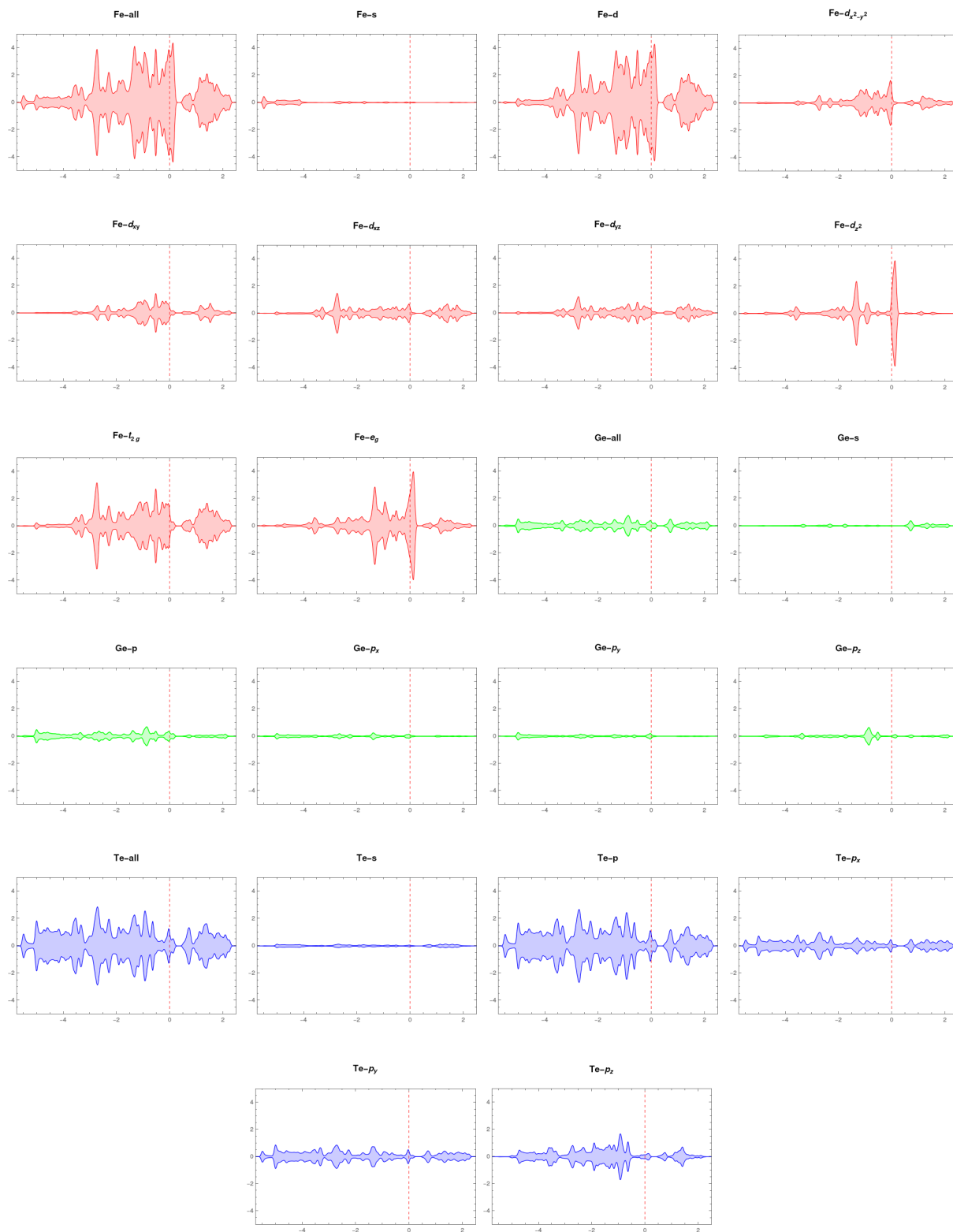
Figure A.8: Detailed density of states for the anti-ferromagnetic FeGeTe$_3$ monolayer, calculated using the PBESol functional for each atomic orbital, is shown. The horizontal axis represents the energy difference $E - E_F$, while the vertical axis indicates the normalized density of states (states/eV)
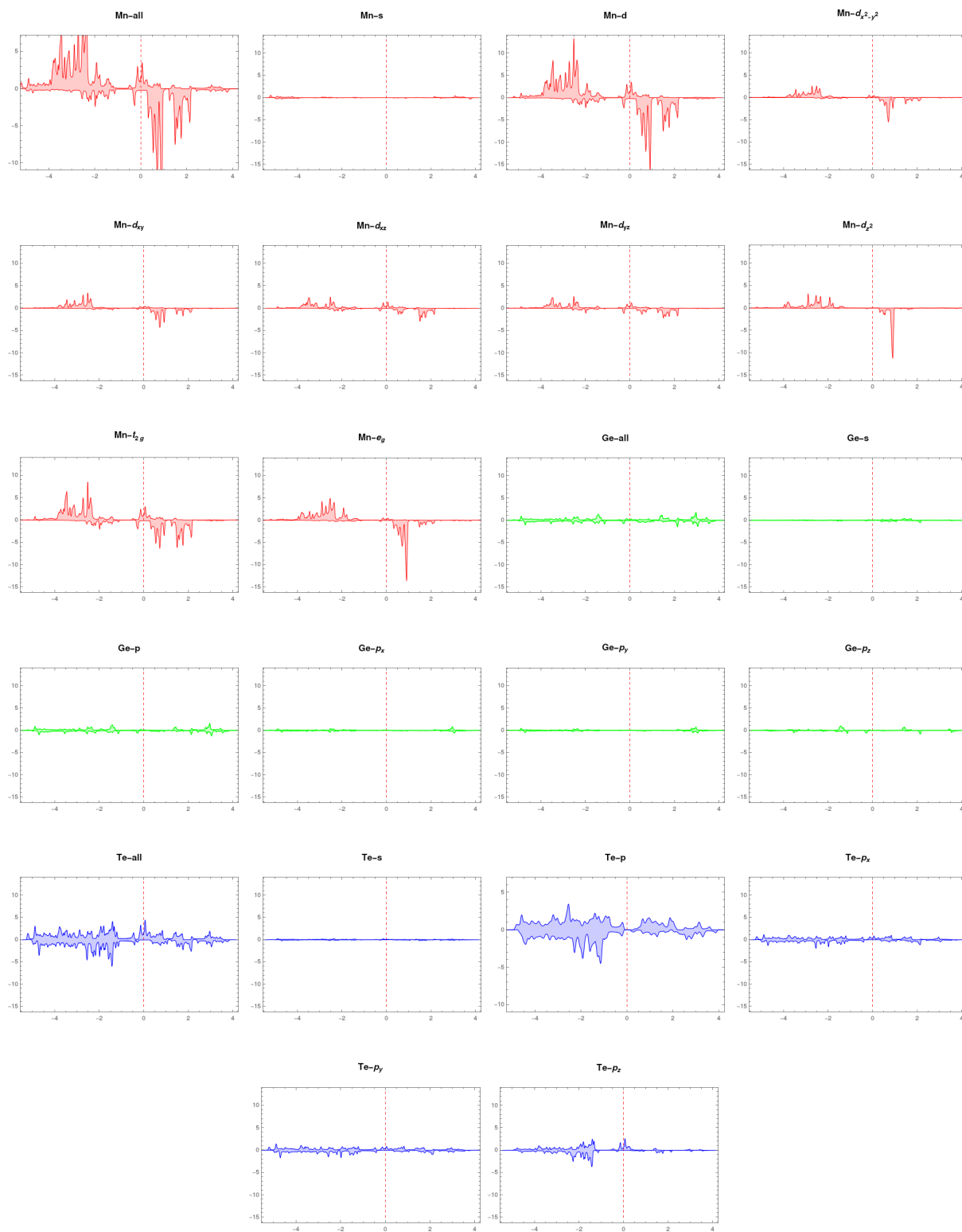
Figure A.9: Detailed density of states for the anti-ferromagnetic FeGeTe$_3$ monolayer, calculated using the hybrid functional HSE06 for each atomic orbital, is shown. The horizontal axis represents the energy difference $E - E_F$, while the vertical axis indicates the normalized density of states (states/eV)
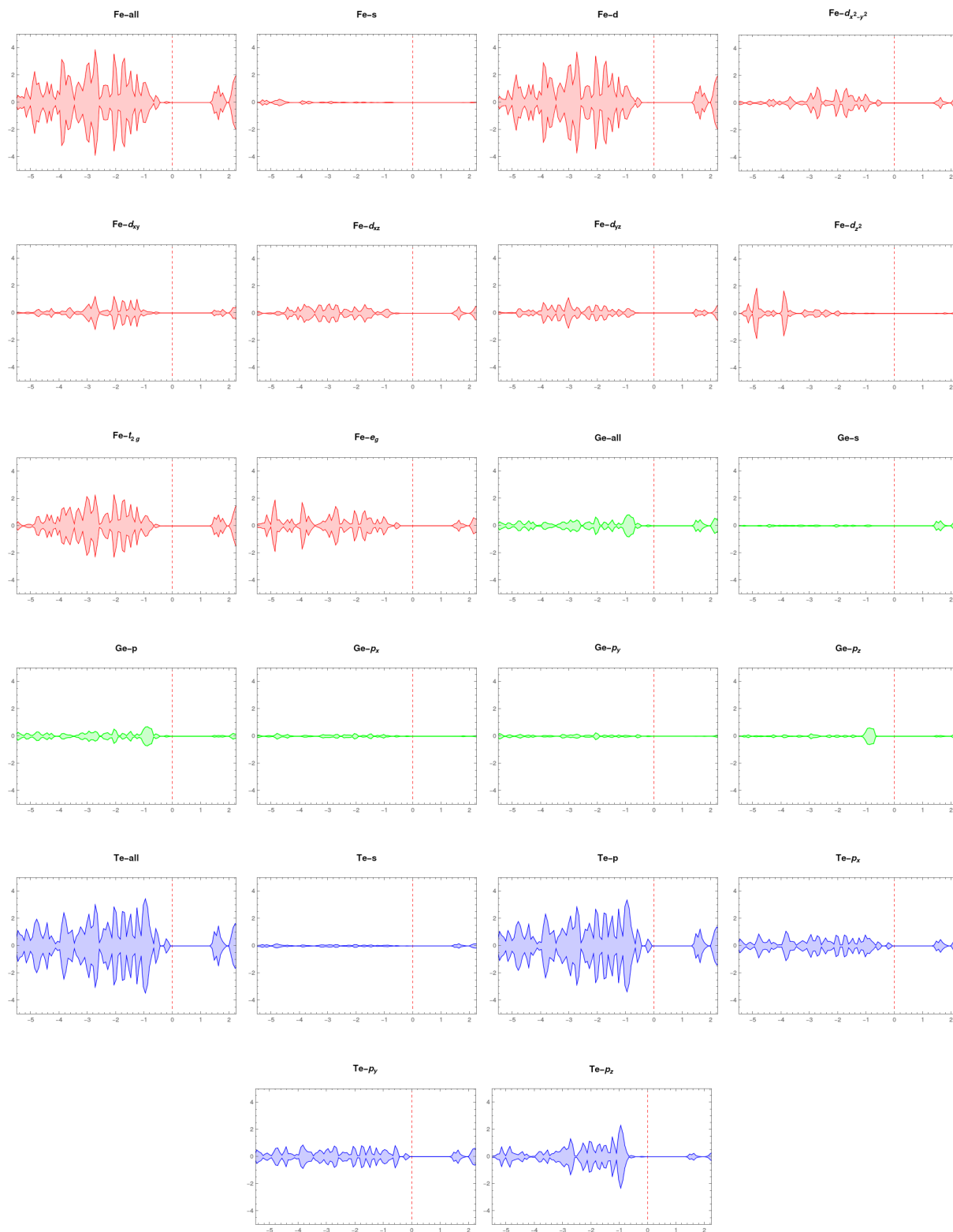
Bibliography

[1]   Zheng Xiao Guo. *Multiscale Materials Modelling: Fundamentals and Applications*. Elsevier, 2007. ISBN: 978-1-84569-071-7.

[2]   June Gunn Lee. *Computational Materials Science : An Introduction*. 2nd ed. CRC Press, 2011. ISBN: 978-1-4987-4973-2.

[3]   Anurag Gaur, AL Sharma, and Anil Arya. *Energy Storage and Conversion Devices: Supercapacitors, Batteries, and Hydroelectric Cells (Emerging Materials and Technologies)*. 1st ed. CRC Press, 2021. ISBN: 978-0-3676-9425-8.

[4]   Feliciano Giustino. *Materials Modelling using Density Functional Theory: Properties and Predictions*. 1st ed. Oxford University Press, 2014. ISBN: 978-0-1996-6243-2.

[5]   Kostya S Novoselov et al. "Electric field effect in atomically thin carbon films". In: *science* 306.5696 (2004), pp. 666–669.

[6]   JT Paul et al. "Computational methods for 2D materials: discovery, property characterization, and application design". In: *Journal of Physics: Condensed Matter* 29.47 (2017), p. 473001.

[7]   Soo Ho Choi et al. "Large-scale synthesis of graphene and other 2D materials towards industrialization". In: *Nature Communications* 13.1 (2022), p. 1484.

[8]   Guillaume Cassabois, Pierre Valvin, and Bernard Gil. "Hexagonal boron nitride is an indirect bandgap semiconductor". In: *Nature photonics* 10.4 (2016), pp. 262–266.

[9]   Andrea Splendiani et al. "Emerging photoluminescence in monolayer MoS2". In: *Nano letters* 10.4 (2010), pp. 1271–1275.

[10] Ashwin Ramasubramaniam, Doron Naveh, and Elias Towe. "Tunable band gaps in bilayer transition-metal dichalcogenides". In: *Physical Review B* 84.20 (2011), p. 205325.

[11] Xianguang Ding et al. "Defect engineered bioactive transition metals dichalcogenides quantum dots". In: *Nature Communications* 10.1 (2019), p. 41.

[12] Nikhil Sivadas et al. "Magnetic ground state of semiconducting transition-metal trichalcogenide monolayers". In: *Physical Review B* 91.23 (2015), p. 235425.

[13]   Cheng Gong et al. "Discovery of intrinsic ferromagnetism in two-dimensional van der Waals crystals". In: *Nature* 546.7657 (2017), pp. 265–269.

[14]   Bevin Huang et al. "Layer-dependent ferromagnetism in a van der Waals crystal down to the monolayer limit". In: *Nature* 546.7657 (2017), pp. 270–273.

[15]   Magnetic Gibertini et al. "Magnetic 2D materials and heterostructures". In: *Nature nanotechnology* 14.5 (2019), pp. 408–419.

[16]   Vladimir I Anisimov, Jan Zaanen, and Ole K Andersen. "Band theory and Mott insulators: Hubbard U instead of Stoner I". In: *Physical Review B* 44.3 (1991), p. 943.

[17]   John P Perdew et al. "Restoring the density-gradient expansion for exchange in solids and surfaces". In: *Physical review letters* 100.13 (2008), p. 136406.

[18]   Bheema Lingam Chittari et al. "Carrier-and strain-tunable intrinsic magnetism in two-dimensional M A X 3 transition metal chalcogenides". In: *Physical Review B* 101.8 (2020), p. 085415.

[19]   Yanxing Song et al. "Tunable magnetic anisotropy, half-metallicity and tunneling magnetoresistance effect of 2D CrI3 in CrI3/MnGeX3 (X= Se, Te) heterostructures under normal compressive strain". In: *Physics Letters A* (2023), p. 128944.

[20]   Kuan-Rong Hao et al. "The atlas of ferroicity in two-dimensional MGeX 3 family: Room-temperature ferromagnetic half metals and unexpected ferroelectricity and ferroelasticity". In: *Nano Research* 14 (2021), pp. 4732–4739.

[21]   Janice A Steckel David Sholl. *Density functional theory: A practical introduction*. Wiley-Interscience, 2009. ISBN: 0470373172.

[22]   Pierre Hohenberg and Walter Kohn. "Inhomogeneous electron gas". In: *Physical review* 136.3B (1964), B864.

[23]   Mildred Dresselhaus et al. *Solid State Properties: From Bulk to Nano*. 1st ed. Graduate Texts in Physics. Springer-Verlag Berlin Heidelberg, 2018. ISBN: 978-3-662-55920-8.

[24]   Scheffler M and Carbogno C. *Theoretical Materials Science*. Fritz Haber Institute of the Max Planck Society, 2017.

[25]   Walter Kohn and Lu Jeu Sham. "Self-consistent equations including exchange and correlation effects". In: *Physical review* 140.4A (1965), A1133.

[26]   David M Ceperley and Berni J Alder. "Ground state of the electron gas by a stochastic method". In: *Physical review letters* 45.7 (1980), p. 566.

[27]   John P Perdew and Alex Zunger. "Self-interaction correction to density-functional approximations for many-electron systems". In: *Physical review B* 23.10 (1981), p. 5048.

[28]   Joseph Morin and Jean Marie Pelletier. *Density functional theory Principles, applications and analysis*. Nova Science Publishers, Incorporated, 2013.

[29] Ulf Von Barth and Lars Hedin. "A local exchange correlation potential for the spin polarized case I". In: *Journal of Physics C: Solid State Physics* 5.13 (1972), p. 1629.

[30] Seymour H Vosko, Leslie Wilk, and Marwan Nusair. "Accurate spin dependent electron liquid correlation energies for local spin density calculations a critical analysis". In: *Canadian Journal of physics* 58.8 (1980), pp. 1200–1211.

[31] Hans Hellmann. "A new approximation method in the problem of many electrons". In: *The Journal of Chemical Physics* 3.1 (1935), pp. 61–61.

[32] Richard M Martin. *Electronic structure: basic theory and practical methods*. Cambridge university press, 2020.

[33] Axel Gross. *Theoretical surface science*. Vol. 132. Springer, 2003.

[34] D Jetal Chadi and Marvin L Cohen. "Special points in the Brillouin zone". In: *Physical Review B* 8.12 (1973), p. 5747.

[35] Lev Kantorovich (auth.) *Quantum Theory of the Solid State: An Introduction*. 1st ed. Fundamental Theories of Physics 136. Springer Netherlands, 2004. ISBN: 9781402021534.

[36] Richard Charles Andrew et al. "Mechanical properties of graphene and boronitrene". In: *Physical Review B—Condensed Matter and Materials Physics* 85.12 (2012), p. 125428.

[37] Georg Kresse and Daniel Joubert. "From ultrasoft pseudopotentials to the projector augmented wave method". In: *Physical review b* 59.3 (1999), p. 1758.

[38] O Bengone et al. "Implementation of the projector augmented-wave LDA+ U method: Application to the electronic structure of NiO". In: *Physical Review B* 62.24 (2000), p. 16392.

[39] Dudarev Sergei L Botton et al. "Electron energy loss spectra and the structural stability of nickel oxide: An LSDA+ U study". In: *Physical Review B* 57.3 (1998), p. 1505.

[40] S-H Wei et al. "Electronic properties of random alloys-Special quasirandom structures". In: *Physical Review B* 42.15 (1990), p. 9622.

[41] Alex Zunger and Wei. "Special quasirandom structures". In: *Physical review letters* 65.3 (1990), p. 353.

[42] A. van de Walle et al. "Efficient stochastic generation of Special Quasirandom Structures". In: *Calphad* 42 (2013), pp. 13–18. DOI: `10.1016/j.calphad.2013.06.006`.

[43] Harold T Stokes and Dorian M Hatch. "FINDSYM: program for identifying the space-group symmetry of a crystal". In: *Journal of Applied Crystallography* 38.1 (2005), pp. 237–238.

[44] Atsushi Togo et al. "Implementation strategies in phonopy and phono3py". In: *J. Phys. Condens. Matter* 35.35 (2023), p. 353001. DOI: `10.1088/1361-648X/acd831`.

[45] Atsushi Togo. "First-principles Phonon Calculations with Phonopy and Phono3py". In: *J. Phys. Soc. Jpn.* 92.1 (2023), p. 012001. DOI: `10.7566/JPSJ.92.012001`.

[46]   A. van de Walle. "Multicomponent multisublattice alloys, nonconfigurational entropy and other additions to the Alloy Theoretic Automated Toolkit". In: *Calphad* 33 (2009), pp. 266–278. DOI: `10.1016/j.calphad.2008.12.005`.

[47]   A. van de Walle, M. D. Asta, and G. Ceder. "The Alloy Theoretic Automated Toolkit: A User Guide". In: *Calphad* 26 (2002), pp. 539–553. DOI: `10.1016/S0364-5916(02)80006-2`.

[48]   A. van de Walle and G. Ceder. "Automating First-Principles Phase Diagram Calculations". In: *J. Phase Equilib.* 23 (2002), pp. 348–359. DOI: `10.1361/105497102770331596`.

[49]   A. van de Walle and M. D. Asta. "Self-driven lattice-model Monte Carlo simulations of alloy thermodynamic properties and phase diagrams". In: *Model. Simul. Mater. Sc.* 10 (2002), p. 521. DOI: `10.1088/0965-0393/10/5/304`.

[50]   A. van de Walle. "Methods for First-Principles Alloy Thermodynamics". In: *JOM - J. Min. Met. Mat. S.* 65 (2013), pp. 1523–1532. DOI: `10.1007/s11837-013-0764-3`.

[51]   A. van de Walle. "A complete representation of structure-property relationships in crystals". In: *Nat. Mater.* 7 (2008), pp. 455–458. DOI: `10.1038/nmat2190`.

[52]   A. van de Walle and D. Ellis. "First-principles thermodynamics of coherent interfaces in samarium-doped ceria nanoscale superlattices". In: *Phys. Rev. Lett.* 98 (2007), p. 266101. DOI: `10.1103/PhysRevLett.98.266101`.

[53]   E. Cockayne and A. van de Walle. "Building effective models from scarce but accurate data: Application to an alloy cluster expansion model". In: *Phys. Rev. B* 81 (2010), p. 012104. DOI: `10.1103/PhysRevB.81.012104`.

[54]   A. van de Walle et al. "Ab initio calculation of anisotropic interfacial excess free energies". In: *Phys. Rev. B* 89 (2014), p. 184101. DOI: `10.1103/PhysRevB.89.184101`.

[55]   A. van de Walle et al. "The free energy of mechanically unstable phases". In: *Nature Commun.* 6 (2015), p. 7559. DOI: `10.1038/ncomms8559`.

[56]   A. van de Walle et al. "Epicycle method for elasticity limit calculations". In: *Phys. Rev. B* 95 (2017), p. 144113. DOI: `10.1103/PhysRevB.95.144113`.

[57]   R. Sun and A. van de Walle. "Automating impurity-enhanced antiphase boundary energy calculations from ab initio Monte Carlo". In: *Calphad* 53 (2016), p. 20. DOI: `10.1016/j.calphad.2016.02.005`.

[58]   A. van de Walle et al. "Software tools for high-throughput CALPHAD from first-principles data". In: *Calphad* 58 (2017), p. 70. DOI: `10.1016/j.calphad.2017.05.005`.

[59]   A. van de Walle. "Reconciling SGTE and ab initio enthalpies of the elements". In: *Calphad* 60 (2018), p. 1. DOI: `10.1016/j.calphad.2017.10.008`.

[60]   H. Liu and A. van de Walle. "Rapid Geometric Screening of Low-Energy Surfaces in Crystals". In: *Symmetry* 14 (2022), p. 2067. DOI: `10.3390/sym14102067`.

[61]   *EDIFF*. URL: https://www.vasp.at/wiki/index.php/EDIFF.

[62]   Mohamed Barhoumi. "The density functional theory and beyond-Example and applications". In: *Density Functional Theory-Recent Advances, New Perspectives and Applications* (2021).

[63]   Peter E Blöchl. "Projector augmented-wave method". In: *Physical review B* 50.24 (1994), p. 17953.

[64]   *POSCAR*. URL: https://www.vasp.at/wiki/index.php/POSCAR.

[65]   *KPOINTS*. URL: https://www.vasp.at/wiki/index.php/KPOINTS.

[66]   Charles Kittel. *Introduction to Solid State Physics*. 7th ed. Wiley, 1995. ISBN: 9780471111818.

[67]   N. David Mermin Neil W. Ashcroft. *Solid state physics*. 1st ed. Solid State Physics. Holt, Rinehart and Winston, 1976. ISBN: 9780030839931.

[68]   Yoyo Hinuma et al. "Band structure diagram paths based on crystallography". In: *Computational Materials Science* 128 (2017), pp. 140–184.

[69]   Togo Atsushi and Tanaka Isao. "Spglib a software library for crystal symmetry search". In: *arXiv preprint arXiv:1808.01590* (2018).

[70]   Junjie He et al. "Remarkably enhanced ferromagnetism in a super-exchange governed Cr 2 Ge 2 Te 6 monolayer via molecular adsorption". In: *Journal of Materials Chemistry C* 7.17 (2019), pp. 5084–5093.

[71]   Jiayong Zhang et al. "Robust quantum anomalous Hall effect in graphene-based van der Waals heterostructures". In: *Physical Review B* 92.16 (2015), p. 165418.

[72]   Kangying Wang et al. "Magnetic and electronic properties of Cr2Ge2Te6 monolayer by strain and electric-field engineering". In: *Applied Physics Letters* 114.9 (2019).

[73]   Aliaksandr V Krukau et al. "Influence of the exchange screening parameter on the performance of screened hybrid functionals". In: *The Journal of chemical physics* 125.22 (2006).

[74]   Yimei Fang et al. "Large magneto optical effects and magnetic anisotropy energy in two-dimensional Cr 2 Ge 2 Te 6". In: *Physical Review B* 98.12 (2018), p. 125416.